

AD-A273 820

AFIT/GAE/ENY/93D-14



DTIC
S ELECTE D
DEC 16 1993
E

ANALYSIS AND CHARACTERIZATION OF
COMPRESSOR STALL PRECURSOR SIGNALS IN
FORWARD AND AFT SWEPT HIGH SPEED
COMPRESSORS

THESIS

Bernard J. Frank, Capt, USAF
AFIT/GAE/ENY/93D-14
Approved for public release
Distribution Unlimited

93-30494



93 12 15112

AFIT/GAE/ENY/93D-14

ANALYSIS AND CHARACTERIZATION OF COMPRESSOR STALL
PRECURSOR SIGNALS IN FORWARD AND AFT SWEPT
HIGH SPEED COMPRESSORS

THESIS

Presented to the Faculty of the Graduate School of
Engineering of the Air Force Institute of Technology
Air University
in Partial Fulfillment of the
Requirements for the Degree of
Master of Science in Aeronautical Engineering

Bernard J. Frank, B.S.

Captain, USAF

November 1993

Approved for public release, Distribution Unlimited

ACKNOWLEDGEMENTS

Many thanks are owed to many people for the success of this research. Much of the credit for its success belongs to Dr Paul King, my advisor. Through many long hours of discussion, we were able to add this research to the existing works in this area. I must also thank the insights and suggestions received from my thesis committee, Dr William Elrod and Dr Rodney Bowersox.

My thanks also go out to Dr Bill Copenhaver and the staff of the Compressor Aerodynamic Research Laboratory for sponsoring this research, providing the data and allowing me the freedom to perform this analysis. I look forward to working with them in the future.

This acknowledgement section would not be complete without thanking Charlotte Coleman of the Scientific and Engineering Application Section of the Communications-Computer Systems Group for her help in digitizing and re-digitizing the data used in this analysis. Many long hours were spent processing the analog tapes used to produce the results found in this thesis.

I also owe a very special thank you to my wife and best friend Wallene. Her tireless support and encouragement through these past months have made this job much easier. There were many times during these long months that she must have thought she was a single mom. It is to my dear wife Wallene that this thesis is dedicated.

Accession For	
NTIS	CRA&I <input checked="checked" type="checkbox"/>
DTIC	TAB <input checked="checked" type="checkbox"/>
Unannounced	<input type="checkbox"/>
Justification	
By	
Distribution /	
Availability Codes	
Dist	Avail and/or Special
A-1	

DTIC QUALITY INSPECTED 1

TABLE OF CONTENTS

	Page
ACKNOWLEDGEMENTS	ii
LIST OF FIGURES	v
LIST OF TABLES	ix
LIST OF SYMBOLS	x
ABSTRACT	xi
1.0 INTRODUCTION	1-1
1.1 Background	1-1
1.2 Rotating stall	1-2
1.3 Surge	1-4
1.4 Stall inception	1-5
1.5 Scope of the present work	1-8
2.0 FACILITY AND EQUIPMENT	2-1
2.1 Compressor Aerodynamic Research Laboratory (CARL)	2-1
2.2 Rotor descriptions	2-2
2.3 Signal processing	2-3
3.0 METHODOLOGY	3-1
3.1 Analysis process	3-1
3.2 Calibration	3-1
3.3 Power spectrum densities (PSD) analysis	3-2
3.4 Channel subtraction process	3-3
3.5 Digital filtering	3-6
3.6 Spatial Fourier Transform	3-7
3.7 Phase tracking analysis	3-9
3.8 System identification	3-11
3.9 Testing of the system identification method	3-15
4.0 RESULTS	4-1
4.1 Introduction	4-1
4.2 Rotor 4	4-4
4.2.1 70% Speed	4-5
4.2.2 80% Speed	4-7
4.2.3 90% Speed	4-8
4.2.4 100% Speed	4-8
4.3 Rotor 6	4-9
4.3.1 70% Speed	4-9
4.3.2 80% Speed	4-10
4.3.4 90% Speed	4-10
4.3.4 100% Speed	4-11
4.4 Rotor 8	4-11

4.4.1 80% Speed	4-12
4.4.2 90% Speed	4-12
4.4.3 100% Speed	4-13
4.5 Rotor 9	4-13
4.5.1 80% Speed	4-14
4.5.2 90% Speed	4-15
4.5.3 100% Speed	4-15
4.6 Summary of results	4-16
5.0 CONCLUSIONS AND RECOMMENDATIONS	5-1
5.1 Discussion	5-1
5.1.1 Analysis methods	5-1
5.1.2 Rotor characterization	5-2
5.2 Conclusions	5-3
5.3 Recommendations	5-5
6.0 REFERENCES	6-1
7.0 FIGURES	7-1
VITA	8-1

LIST OF FIGURES

	Page
Figure 1.1 Compressor Map with Pressure Rise and Efficiency Copenhaver [1]	7-1
Figure 1.2 Abrupt/Progressive Stall Pampreen [7]	7-1
Figure 1.3 Example of Progressive Stall	7-2
Figure 1.4 Example of Abrupt Stall	7-2
Figure 1.5 Compressor Surge/Rotating Stall Boundary Copenhaver [1]	7-3
Figure 2.1 Schematic of CARL Facility	7-4
Figure 2.2 Sketch of Rotor 4	7-5
Figure 2.2 Sketch of Rotor 6	7-5
Figure 2.4 Sketch of Rotor 8	7-6
Figure 2.5 Sketch of Rotor 9	7-6
Figure 2.6 Pressure Signal Processing Boyer et al. [14]	7-7
Figure 3.1 Example of Stall Point Location	7-8
Figure 4.1 Channel Subtraction/Addition Results	7-9
Figure 4.2 Frequency and Damping Factor - 1st And 2nd Mode -Rotor 4 70% Speed without lowpass Filtering	7-10
Figure 4.3 Frequency and Damping Factor - Mode 1 Rotor 4 70% Speed - Lowpass filtered at 0.9/rev	7-11
Figure 4.4 Frequency and Damping Factor - Mode 1 Rotor 4 70% Speed - Lowpass filtered at 0.7/rev	7-11
Figure 4.5 Frequency and Damping Factor - Mode 1 Rotor 4 70% Speed - Lowpass filtered at 0.6/rev	7-12
Figure 4.6 Spatial Fourier Magnitude versus Time plot Rotor 4 70% Speed	7-12
Figure 4.7 Spatial Fourier Phase versus Time plot Rotor 4 70% Speed	7-13
Figure 4.8 Phase Tracking Output - Rotor 4 70% Speed	7-13
Figure 4.9 Windowed Frequency Pressure Signal Data (180 Degree Subtracted) - Rotor 4 70% Speed	7-14
Figure 4.10 Windowed Frequency Pressure Signal (180 Degree Addition) - Rotor 4 70% Speed	7-15
Figure 4.11 Windowed Frequency Spectrum from SFCs Rotor 4 70% Speed	7-16
Figure 4.12 Spatial Fourier Magnitude versus Time plot Rotor 4 80% Speed	7-17
Figure 4.13 Spatial Fourier Phase versus Time plot Rotor 4 80% Speed	7-17
Figure 4.14 Frequency and Damping Factor Rotor 4 80% Speed	7-18
Figure 4.15 Windowed Frequency Pressure Signal Data Rotor 4 80% Speed	7-18
Figure 4.16 Windowed Frequency Spectrum from SFCs Rotor 4 80% Speed	7-19
Figure 4.17 Spatial Fourier Magnitude versus Time plot	

Rotor 4 90% Speed	7-19
Figure 4.18 Spatial Fourier Phase versus Time plot	
Rotor 4 90% Speed	7-20
Figure 4.19 Frequency and Damping Factor	
Rotor 4 90% Speed	7-20
Figure 4.20 Windowed Frequency Pressure Signal	
Rotor 4 90% Speed	7-21
Figure 4.21 Windowed Frequency Spectrum from SFCs	
Rotor 4 90% Speed	7-21
Figure 4.22 Spatial Fourier Magnitude versus Time plot	
Rotor 4 100% Speed	7-22
Figure 4.23 Spatial Fourier Phase versus Time plot	
Rotor 4 100% Speed	7-22
Figure 4.24 Frequency and Damping Factor	
Rotor 4 100% Speed	7-23
Figure 4.25 Windowed Frequency Pressure Signal Data	
Rotor 4 100% Speed	7-23
Figure 4.26 Windowed Frequency Spectrum from SFCs	
Rotor 4 100% Speed	7-24
Figure 4.27 Spatial Fourier Magnitude versus Time plot	
Rotor 6 70% Speed	7-24
Figure 4.28 Spatial Fourier Phase versus Time plot	
Rotor 6 70% Speed	7-25
Figure 4.29 Frequency and Damping Factor	
Rotor 6 70% Speed	7-25
Figure 4.30 Windowed Frequency Pressure Signal Data	
Rotor 6 70% Speed	7-26
Figure 4.31 Windowed Frequency Spectrum from SFCs	
Rotor 6 70% Speed	7-26
Figure 4.32 Spatial Fourier Magnitude versus Time plot	
Rotor 6 80% Speed	7-27
Figure 4.33 Spatial Fourier Phase versus Time plot	
Rotor 6 80% Speed	7-27
Figure 4.34 Frequency and Damping Factor	
Rotor 6 80% Speed	7-28
Figure 4.35 Windowed Frequency Pressure Signal Data	
Rotor 6 80% Speed	7-28
Figure 4.36 Windowed Frequency Spectrum from SFCs	
Rotor 6 80% Speed	7-29
Figure 4.37 Spatial Fourier Magnitude versus Time plot	
Rotor 6 90% Speed	7-29
Figure 4.38 Spatial Fourier Phase versus Time plot	
Rotor 6 90% Speed	7-30
Figure 4.39 Frequency and Damping Factor	
Rotor 6 90% Speed	7-30
Figure 4.40 Windowed Frequency Pressure Signal Data	
Rotor 6 90% Speed	7-31
Figure 4.41 Windowed Frequency Spectrum from SFCs	
Rotor 6 90% Speed	7-31
Figure 4.42 Spatial Fourier Magnitude versus Time plot	

Rotor 6 100% Speed	7-32
Figure 4.43 Spatial Fourier Phase versus Time plot	
Rotor 6 100% Speed	7-32
Figure 4.44 Frequency versus Damping Factor	
Rotor 6 100% Speed	7-33
Figure 4.45 Windowed Frequency Pressure Signal Data	
Rotor 6 100% Speed	7-33
Figure 4.46 Windowed Frequency Spectrum from SFCs	
Rotor 6 100% Speed	7-34
Figure 4.47 Spatial Fourier Magnitude versus Time plot	
Rotor 8 80% Speed	7-34
Figure 4.48 Spatial Fourier Phase versus Time plot	
Rotor 8 80% Speed	7-35
Figure 4.49 Frequency and Damping Factor	
Rotor 8 80% Speed	7-35
Figure 4.50 Windowed Frequency Pressure Signal Data	
Rotor 8 80% Speed	7-36
Figure 4.51 Windowed Frequency Spectrum from SFCs	
Rotor 8 80% Speed	7-36
Figure 4.52 Spatial Fourier Magnitude versus Time plot	
Rotor 8 90% Speed	7-37
Figure 4.53 Spatial Fourier Phase versus Time plot	
Rotor 8 90% Speed	7-37
Figure 4.54 Frequency and Damping Factor	
Rotor 8 90% Speed	7-38
Figure 4.55 Windowed Frequency Pressure Signal Data	
Rotor 8 90% Speed	7-38
Figure 4.56 Windowed Frequency Spectrum from SFCs	
Rotor 8 90% Speed	7-39
Figure 4.57 Spatial Fourier Magnitude versus Time plot	
Rotor 8 100% Speed	7-39
Figure 4.58 Spatial Fourier Phase versus Time plot	
Rotor 8 100% Speed	7-40
Figure 4.59 Frequency and Damping Factor	
Rotor 8 100% Speed	7-40
Figure 4.60 Windowed Frequency Pressure Signal Data	
Rotor 8 100% Speed	7-41
Figure 4.61 Windowed Frequency Spectrum from SFCs	
Rotor 8 100% Speed	7-41
Figure 4.62 Spatial Fourier Magnitude versus Time plot	
Rotor 9 80% Speed	7-42
Figure 4.63 Spatial Fourier Phase versus Time plot	
Rotor 9 80% Speed	7-42
Figure 4.64 Frequency and Damping Factor	
Rotor 9 80% Speed	7-43
Figure 4.65 Windowed Frequency Pressure Signal Data	
Rotor 9 80% Speed	7-43
Figure 4.64 Windowed Frequency Spectrum from SFCs	
Rotor 9 80% Speed	7-44
Figure 4.65 Spatial Fourier Magnitude versus Time plot	

Rotor 9 90% Speed	7-44
Figure 4.66 Spatial Fourier Phase versus Time plot	
Rotor 9 90% Speed	7-45
Figure 4.67 Frequency and Damping Factor	
Rotor 9 90% Speed	7-45
Figure 4.68 Windowed Frequency Pressure Signal Data	
Rotor 9 90% Speed	7-46
Figure 4.69 Windowed Frequency Spectrum from SFCs	
Rotor 9 90% Speed	7-46
Figure 4.70 Spatial Fourier Magnitude versus Time plot	
Rotor 9 100% Speed	7-47
Figure 4.71 Spatial Fourier Phase versus Time plot	
Rotor 9 100% Speed	7-47
Figure 4.72 Frequency and Damping Factor	
Rotor 9 100% Speed	7-48
Figure 4.73 Windowed Frequency Pressure Signal Data	
Rotor 9 100% Speed	7-48
Figure 4.74 Windowed Frequency Spectrum from SFCs	
Rotor 9 100% Speed	7-49
Figure 4.76 Pressure versus Samples for one Kulite Trace	
Rotor 9 100% Speed (Sample rate = 4000 samples/sec) . .	7-49
Figure 4.77 FFT of Rotor 9 100% After Stall	7-50
Figure 5.1 Compressor Map for Rotor 4	7-51
Figure 5.2 Compressor Map for Rotor 6	7-51
Figure 5.3 Compressor Map for Rotor 8	7-52
Figure 5.4 Compressor Map for Rotor 9	7-52

LIST OF TABLES

	Page
Table 2.1 Kulite Calibration Data	2-2
Table 2.2 Rotor Design Features	2-2
Table 3.1 Effects of Subtraction/Addition of Kulite Data	3-6
Table 4.1 Stall Frequency Comparison for Rotor 4 . . .	4-5
Table 4.2 Stall Frequency Comparison for Rotor 6 . . .	4-9
Table 4.3 Rotor Comparison Table	4-17

LIST OF SYMBOLS

SYMBOLS

Section 1.0

a	--- Speed of Sound
A_c	--- Flow through area of the Compressor
B	--- Dimensionless Surge/Rotating Stall parameter
k	--- Fourier mode number
L_c	--- Effective length of Compressor
t	--- time
U	--- Mean rotor velocity
V_p	--- Exit plenum volume
x	--- Axial location
Θ	--- Circumferential location
λ_k	--- Wave amplitude
σ_k	--- Wave damping
ϕ	--- Flow coefficient
$\bar{\phi}$	--- Circumferential averaged coefficient
ϕ	--- Non-axisymmetric term
ω_k	--- Wave frequency

Section 3.0

A_0	--- Amplitude of the zero mode - Planar wave
A_j	--- Unit amplitude of the rotating wave
a	--- Phase speed calculated with phase tracking method
a_i	--- Output coefficients
b	--- Y-intercept from phase tracking solution
b_i	--- Input coefficients
C_k	--- Spatial Fourier coefficient
j	--- Transducer location
k	--- Mode of spatial Fourier coefficient
L	--- Gain matrix
m	--- Mode of wave
n	--- Number of $\pi/4$ increments from transducer location
	--- Summation term for Equation 3-7
P	--- Covariance matrix
P_j	--- Pressure at the j th transducer location
P_{jW}	--- Pressure after subtraction
p_i	--- Spatial Fourier phase
t	--- Time (Rotor revs)
u	--- Input data
V_n	--- Pressure data at each angular position
y	--- Output data
z	--- Roots of n th order equation
Θ	--- Parameter vector of unknown coefficients
λ	--- Forgetting factor
v	--- Error
ϕ	--- Vector of observed data
DF	--- Damping Factor
Freq	--- Frequency of the system

ABSTRACT

The stall characteristics of four single-stage transonic compressor rotors were investigated as they were throttled to stall. Forward-swept, backward-swept and straight leading edge rotors were examined. Three methods of analysis (1) windowed Power Spectrum Densities of pressure and spatial Fourier coefficients, (2) phase tracking analysis, and (3) system identification were used to identify the first appearance of modal waves and their accompanying frequencies in order to identify a stall warning time. A direct correlation between the amount of stall warning time and the shape of the compressor characteristic was found. Specifically, if the compressor characteristic had a significant period of flat or positive slope more stall warning was noted. It was also found that the forward-swept rotor consistently provided more stall warning time than the backward-swept and straight leading edge rotors.

1.0 INTRODUCTION

1.1 Background

The three main energy exchanging components of the gas turbine engine are the compressor, combustor, and turbine. The compressor is responsible for providing high pressure, high density air to the combustor. The air enters the combustor where thermal energy is added to the flow through the combustion process. The high pressure combustion gases are then converted to work through an expansion process in the turbine. Since the combustion and expansion processes are very efficient operations, the compressor too must operate with a high degree of efficiency to maintain the efficiency of the entire thermodynamic cycle.

The compressor, however, does not normally operate at its design speed and flow rate. Instead, it operates over a range of flow coefficients and rotational speeds. For this reason, a compressor map (Figure 1.1) is used to relate the compressor pressure rise to the mass flow condition for varying rotational speeds. Also seen in Figure 1.1 the compressor efficiency is a function of the operating point of the compressor.

For each speed line, there exists a maximum pressure rise which occurs as the mass flow is continually decreased. If the mass flow is decreased beyond this point the compressor becomes aerodynamically unstable, resulting in either surge or rotating stall. Unfortunately, as seen

in Figure 1.1 this point usually occurs at maximum pressure rise and maximum compressor efficiency.

This instability is commonly referred to as compressor stall. However, this term is rather misleading because two distinctly different instabilities may arise, rotating stall or surge. As the compressor becomes unstable either surge, rotating stall, or a combination of both instabilities may appear. By using high speed dynamic measurements, Stenning [2] found that surge may be triggered very rapidly by rotating stall. Day et al. [3] also indicated a similar result, restricting his findings to axial compressors.

1.2 Rotating stall

One of the first theories for rotating stall propagation was published by Emmons et al. [4]. Rotating stall occurs when the flow from one or more blades separates, forming a blockage. This blockage causes the flow to be deflected to both sides of the blocked blade passages. The blades in the direction of the rotation see a reduced incidence and continue to produce a pressure rise. However, the blades opposite the direction of rotation see an increased incidence. Since these blades were near stall prior to the blocked cell forming, they now stall, causing a new stall cell to form and giving relief to the old blockage. Thus, the blockage appears to propagate about the rotor annulus. In the relative reference frame, the stall cell appears to propagate opposite the direction of rotation. However, from the absolute

reference frame, the stall cell rotates in the direction of rotation at a fraction of the rotation velocity (usually 40 to 60% of rotational velocity). This study, along with that of Boyer et al. [5] and Garnier [6] confirmed that the rotation of the stall cell was indeed in the direction of rotation and always at a fraction of the rotor speed. The blockage, once fully formed does not significantly reduce the averaged mass flow.

The geometry of a stall cell is dependent upon several different factors. These factors include hub/tip ratio, tip speed, and the presence or absence of inlet guide vanes. As seen in the compilation of research put together by Pampreen [7], in most cases rotating stall formed at the tip, with a part-span cell forming and progressed into full span stall.

Pampreen [7] characterized stall in two different ways, progressive and abrupt stall. Progressive stall occurred when the rotor gradually reduced its pressure rise as the stall began. Abrupt stall occurred when there was a sharp decrease in the pressure rise as stall began. Both characterizations can be seen in Figure 1.2.

However, for this study the definition of abrupt and progressive stall will be based on the magnitude of the spatial Fourier transform for the system. (The spatial Fourier transform will be explained in detail in Section 3.5) If the magnitude of the spatial Fourier coefficient gradually increased, this was identified as a progressive stall (Figure 1.3). Alternatively, abrupt stall was identified by a sudden increase in the magnitude of the spatial

Fourier coefficient (Figure 1.4).

1.3 Surge

Surge is characterized by the blockage or reversal of the entire axial flow, and results in the large amplitude oscillations of the mass flow. At high rotational speeds, as the compressor reaches the stall line, surge occurs usually triggered and accompanied by rotating stall. While at low rotational speeds only rotating stall is encountered. The boundary line between these two instabilities is presented graphically in Figure 1.5.

The theory describing the boundary between rotating stall and surge was presented by Greitzer [8], [9]. In part 1 of his study [8], he created a mathematical model based on a physical value that he called the B parameter. The B parameter was defined as follows:

$$B = \frac{U}{2a} \sqrt{\frac{V_p}{A_c L_c}} \quad (1-1)$$

His results indicated that for values of B greater than 1.0, decreasing the mass flow resulted in surge alone. However, for values of B less than 0.8, decreasing the mass flow lead to rotating stall without surge. From Equation 1.1, it can be seen that the value of B is related to the compressor geometry through the length and cross-sectional area. Also note that for large rotational speeds the value of B is increased and the system is more

likely to surge as was seen in Figure 1.5.

Another cause of surge that directly affects the experimental testing of compressor rigs is long ducted regions downstream in the flow. These long ducted regions act as storage reservoirs and result in an installation or system instability as is pointed out by Day et al. [3]. This can also be seen by examining the B parameter. The long ducted region can be thought to be a plenum volume, V_p . Equation 1.1 shows that B is proportional to the square root of the plenum volume, thus increasing the plenum volume will result in an increase in B. For this study, due to the high rotational velocities, a plenum volume of approximately 1.4 ft^3 is sufficient to result in a B parameter of 1.0 based on the speed of sound at sea level $a = 1116 \text{ ft/sec}$, $U = 1073.3 \text{ ft/sec}$, $A_c = 1.42 \text{ ft}^2$, and $L_c = 0.67 \text{ ft}$.

1.4 Stall inception

Stall inception describes the process by which the flow in the compressor becomes unstable. Two models for this process have been proposed. The first model described earlier, was first submitted by Emmons et al. [4]. The stall is produced when minor disturbances of the flow cause the flow around highly loaded blades to momentarily separate. According to Day [10] this is a description of a "disturbance of short length scale."

The second model of stall inception was proposed by Moore and Greitzer [11] which is based on small perturbations of the axial flow. These perturbations propagate circumferentially and if the compressor is throttled

toward stall the perturbations would grow into a stall cell. According to McDougall et al. [12], these perturbations represent the response of the upstream flow to disturbances in the blades, and are termed the modes of the system. A blade disturbance that produced a perturbation of a wavelength equal to that of the annular circumference would be called modal wave of order 1.

In order to prove the existence of these rotating wave, Garnier [6] began with the governing equation for the Moore and Greitzer model [11] (Equation 1.2).

$$\phi = \bar{\phi} + \tilde{\phi} \quad (1-2)$$

Then by utilizing the fact that the flow upstream was potential and that the non-axisymmetric part would vanish far upstream, Garnier was able to show that the non-axisymmetric part would have the solution of the form

$$\tilde{\phi}(t, \theta, x) = \sum_{|k| \neq 0}^{\infty} a_k(t) e^{ik|x} e^{ik\theta} \quad (1-3)$$

Assuming small perturbations and linearizing the total to static pressure rise equation, he found that the solution for $\tilde{\phi}$ was

$$\Phi = \sum_{|k| \neq 0} \lambda_k e^{(|k|x + \sigma_k t)} e^{i(k\theta - \omega_k t)} \quad (1-4)$$

Through this solution, Garnier [6] showed that each Fourier mode k is the product of two exponentials. The complex exponential represents the travelling wave, where θ represents the circumferential position and ω_k represents the wave frequency. The real exponential represents the wave amplitude's dependence on the axial position x , and the wave damping, σ_k . In both exponential terms t represents time. Garnier [6] notes that the model presented by Equation 1.4 is due only to a lag in the compressor response to local accelerations in the flow and does not represent a redistribution of the upstream flow field.

Garnier [6] went on to experimentally support this model, demonstrating the existence of modal waves in two low speed and one high speed compressor. McDougall et al. [13] also found similar results concluding that modal waves were always present prior to stall and the small amplitude perturbation model was the only valid model for stall inception.

In contrast, Day [10] concluded that both models were indeed causes for stall. He also concluded that modal waves were not always present prior to stall. In these cases, stall was induced by a stall cell of finite duration. He also concluded that the modal waves may or may not be coupled to the stall phenomenon.

1.5 Scope of the present work

The study of compressor stall and in particular stall inception has been given more attention in the recent years. This is due particularly to the success of active control experiments. Paduano [13] was able to demonstrate a significant extension in the range of the compressor operating region at low flow coefficients. Much of this research, though has been done in the area of low speed compressors (less than 3000 rpm), where the flow is essentially incompressible and subsonic.

The analysis for this study paralleled the one performed by Boyer et al. [5]. However, in addition to the straight and backward swept rotors used in the Boyer et al. [5] study, a forward-swept and a more radically backward swept rotor were also analyzed. One of the main focuses of this investigation was how modal waves are affected by blade sweep, as well as the affect on the stall warning time.

As seen in the Boyer et al. [5] study, there is a high degree of subjectivity in identifying a value of stall warning time. In an effort to better quantify that value, this study used three different analysis methods to correlate a value for stall warning found by any one method. The first method examined the power spectral density for one pressure transducer. The waves of interest to this study normally have a frequency in the range of 40 to 60% of the rotor frequency. The power spectral density method looked specifically at these frequencies as the data was windowed in

time. As this window moved toward the point of stall and the rotating wave frequencies appeared, a note was made of the time. This time value could later be compared to the value found using other methods. This method is explained further in Section 3.3.

The second method used was similar to the technique used by Boyer et al. [5] to identify stall warning time. This method examined the phase changes with time (phase speed) of the Spatial Fourier Coefficients (SFC). (A more detailed description of Spatial Fourier transform and the coefficients is found in Section 3.5). Both methods tried to track the phase speed of the SFC's, trying to identify when the value was approximately equal to 0.5/rev. However, the phase speed values were calculated in different ways. The Boyer et al. [5] study utilized a cubic spline to first smooth the data and then took a numerical derivative to find the phase speed. The method used for this study, utilized a moving average of 250 msec of data (1000 data points) to find the phase speed at that point in time. This window was then stepped 2.5 msec (10 data points) in time and recalculated. Both this method and the method used Boyer et al. [5] provided similar results. This method is explained further in Section 3.7.

The last method utilized a recursive least squares system identification technique. The system identification modeled the SFC's and could be used to identify the frequency and damping factor of the modeled system, namely the rotating waves. This method was used with a certain

degree of success and a more indepth description of the method and its intricacies can be found in Section 3.7.

Additionally, this investigation identified the stall type as either progressive or abrupt for each rotor and speed line, using the SFC magnitude. It also makes a comparison of this determination with the compressor characteristic for each rotor.

The remainder of this report is separated into four sections. Section 2.0 contains a description of the test facility, rotors, and digitizing process. Section 3.0 contains the methodology used to perform this analysis. Section 4.0 contains the results found, while Section 5.0 contains the conclusions and recommendations.

2.0 FACILITY AND EQUIPMENT

2.1 Compressor Aerodynamic Research Laboratory (CARL)

The Compressor Aerodynamic Research Laboratory (CARL) is located at Wright-Patterson AFB, Ohio and is part of the Aero Propulsion and Power Directorate of Wright Laboratory. The CARL is a closed loop compressor test facility capable of producing 2000 Horsepower (Figure 2.1). The CARL produced all the data used in this study.

For the study, the casing upstream of the rotor was fitted with eight Kulite Pressure transducers (model XCEW-1-187-5D) sensitive to 0 to 5 psi. The transducers were placed 0.3 rotor radii (2.5 inches) upstream of the rotor leading edge, for all the rotors with the exception of the forward-swept rotor. With the blade tip swept forward, the leading edge of the forward-swept rotor was only 0.2 rotor radii (1.69 inches) away from the transducer. A five point calibration was done on each transducer used for this study. The data from this calibration is recorded in Table 2.1. This calibration was done to ensure that the transducers were linear in the range of interest (approximately 2 psi). This calibration was used to set the amplifier gains for each transducer such that a 1 psi change in pressure produced a 1 volt signal output to the recorder. A more indepth description of the facility and the process used in gathering the data can be found in Boyer [14].

Table 2.1 Kulite Calibration Data

Serial Number	Angle Pos	Atmos	0.1 (psi)	0.5 (psi)	1.0 (psi)	5.0 (psi)
4554-2-	deg	mv	.. mv	mv	mv	mv
-18	10	0.20	1.42	6.30	12.35	60.65
-19	55	0.40	1.55	6.26	12.18	59.43
-20	100	0.21	1.45	6.23	12.37	61.41
-21	145	0.18	1.48	6.63	13.09	64.09
-23	190	-0.35	0.86	5.71	11.77	60.05
-24	235	-0.06	1.22	6.39	12.18	59.75
-25	280	0.23	1.17	6.23	12.18	59.75
-26	325	0.66	1.96	7.29	13.76	65.87

2.2 Rotor descriptions

There were four rotors used for this study. Each was a single stage transonic design. As was reported in Boyer et al. [5], Table 2.2 contains the design features for the rotors examined in this report.

Table 2.2 Rotor Design Features

Design Speed	20222 rpm
IGV's	None
L.E. tip radius	8.50 in.
L.E. hub radius	2.65 in.
L.E. mean radius	5.58 in.

The rotors were numerically numbered 4,6,8, and 9. Rotor 4 had a straight leading edge (Figure 2.2). It was the baseline rotor for this

investigation as well as the study done by Boyer et al [14]. Rotor 6 was the first backward swept design (Figure 2.3) examined and was also included in the Boyer et al. [14] study. The data from rotor 4 and rotor 6 for this test were not the same as the data used in the Boyer et al [14] study. The data for this report was obtained using 0-5 psi transducers. Like Rotor 6, Rotor 8 was backward swept (Figure 2.4). However, the sweep for this rotor occurred more at the hub than at mid-span. Rotor 9 was the forward swept design used in this study (Figure 2.5). It was the only rotor that caused the leading edge tip to move forward when compared to the other rotors.

For each of the swept rotors, the sweep in the rotor blades was achieved by varying the chord without leaning the blade. This was done by maintaining the trailing edge and varying the spanwise chord length to achieve the desired sweep. In this way, the distance from the transducer to the leading edge of the rotor remained constant for each rotor with the exception of Rotor 9. For Rotor 9, the forward sweep of the blade caused the tip leading edge to move closer to the pressure transducer.

2.3 Signal processing

The signal processing (Figure 2.6) began by recording the data samples at 120 inches per second (ips) on analog tape by the CARL personnel. The tapes were then played back at 120 ips on a 96B Honeywell wideband recorder matching the speed from the record deck by utilizing an internal tachometer. The tachometer helped maintain the integrity of the

frequency spectrum. During playback, the data channels were put through an in-line capacitor to eliminate DC bias, then passed through a Rockland Multi-Channel Analog filter configured for a 1 kHz Butterworth Low-Pass Filter. The rotor frequency for this study ranged from approximately 235 Hz to 350 Hz. Since the rotating wave frequency for mode 1 is approximately $1/2$ the rotor frequency and each of the higher modes close to a multiple of that frequency, the frequencies of interest ranged from approximately 117 Hz to 525 Hz. By lowpass filtering at 1 kHz, the digitized data contained all the frequencies of interest to this study, but the higher frequencies associated with the shock structure of the compressor were eliminated.

An Applied Dynamics AD100 A/D convertor was used to sample the analog tape data. The AD 100 was controlled by a VAX 3500 Computer which also stored the data during the sampling process. This data was sampled at 4000 Hz providing a Nyquist or fold over frequency of 2000 Hz. With the lowpass filter set at 1000 Hz, there was no frequency aliasing. The data was then transferred to an optical drive for storage. A separate data file was generated for each rotor and speed line. Each file contained approximately 10 seconds of data ending with stall.

A 2 volt peak-peak calibration signal was also digitized for each channel of the wideband tape. The calibration signal was recorded prior to the collection of the pressure data. During reproduction the signal is used

to account for differences between record and reproduce amplifiers. By digitizing the calibration signal, the signal was used to generate a calibration program that amplified or attenuated the digital pressure signals to ensure no increase or decrease in amplification took place during the recording to reproduction portion of the analysis.

Finally, the individual data files were electronically transferred to a Sun workstation for off-line analysis.

3.0 METHODOLOGY

3.1 Analysis process

The analysis process was completed in seven separate steps. These steps were (1) Calibration, (2) Frequency Evaluation, (3) Channel Subtraction, (4) Digital Filtering, (5) Spatial Fourier Transform, (6) Phase Tracking Analysis, and (7) System Identification. The specifics of each analysis step is explained in the following sections. All of the analysis was completed using MatLab™ [15], specifically, the Signal Analysis Toolbox [16], a feature built into the software package. Small programs called M-files were written to perform each step of the analysis.

3.2 Calibration

Each tape had a 2 volt peak to peak, 1 Khz sine wave recorded onto each track for calibration purposes. This signal was digitized and it's amplitude was examined to see if it was at 2 volts p-p. If not a multiplication factor was found which would amplify or attenuate the signal to the desired amplitude. This was done for each track. These multiplication factors were then used to calibrate each data channel so that they were all equally correlated.

During the recording process, each transducer was amplified and offset such that 1 volt was equivalent to 1 psi. Therefore, no external conversion was necessary to convert voltage data to pressures.

3.3 Power spectrum densities (PSD) analysis

Once the data was in pressure format, an individual channel was used to perform a PSD analysis. This analysis was done to examine the data in the frequency domain.

One of the main frequencies of interest was the rotor frequency. The rotor frequency was usually one of the most dominant frequencies within the spectrum. This frequency was used to compute the rotor rotational speed.

Each data set was noted to have a surge-like phenomenon at the point of instability. These lower surge frequencies (13-14 Hz and 26-28 Hz) were identified and recorded for each case studied.

The main focus of this analysis method was to locate the approximate time that the rotating wave frequency (approximately 50% rotor frequency) appeared. In order to do this, the channel subtraction technique (described in Section 3.4) was used to isolate the first mode and a FFT was applied to a window of pressure data (approximately 1/2 second of data, 2048 data points). The frequency spectrum was then examined, moving the window in small time steps until the rotating wave frequency (0.5/rev, 120 Hz to 175 Hz) appeared. The time was then recorded for comparison with the other analysis methods.

To take an FFT of the entire data channel, the PSD output would yield the combined effect of frequencies present from the beginning of the

sample to those that appear just before and during stall. In most cases, the PSD was dominated by the 1/rev frequency and the surge frequency. By examining the data in 0.5 second windows, the frequencies that appeared just before stall, were now more recognizable from the noise spectrum. This method in effect, created a digital spectrum analyzer that averaged the data in 2048 bit sections.

3.4 Channel subtraction process

For each rotor and speed studied, a surge-like phenomenon was encountered. This phenomenon was also seen by Boyer et al [5]. As expected with a surge cycle, the pressure wave formed was planar. Since the instability of interest to this study was not the planar disturbance, but in fact a rotating perturbation, a method was devised to eliminate or greatly reduce these planar waves. By subtracting the pressure data of one channel from that of another, any planar waves within the data are eliminated or greatly reduced if slightly out of phase. The effect on the rotating wave signal varied depending on the angle difference of the channels selected.

The technique was based on the premise that during the surge cycle the pressure transducers at each circumferential location saw equal amplitudes of the planar wave, while seeing differing amplitudes of the rotating waves dependent upon the mode of the wave. Based on this assumption, if the pressure from one transducer is subtracted from that of another transducer, the remaining pressure value can only be attributed to

the rotating waves.

To see the effect of this assumption on rotating waves, the modes of a rotating wave are expressed as sine waves where the mode of the wave describes the number of wavelengths in one circumference of the annulus. Since the transducers for this study were located 45 degrees apart, the unit magnitude of that wave at any transducer can be expressed as:

$$A_j = \sin\left(\frac{2\pi mj}{8}\right) \quad (3-1)$$

where m = mode of the wave and $j = 1, 2, \dots, 8$ represents the transducer.

The pressure at any transducer j , can then be expressed as:

$$P_j = A_0 + A_j \quad (3-2)$$

where A_0 represents the amplitude contribution from the planar wave.

Then the expression for the output from subtracting two data channels becomes

$$P_{j_n} = A_j - A_{j+n} = \sin\left(\frac{2\pi mj}{8}\right) - \sin\left(\frac{2\pi mj}{8} + \frac{mn\pi}{4}\right) \quad (3-3)$$

where n is the number of $\pi/4$ radian increments from j th transducer. By choosing the correct two channels, the various modes can be amplified or attenuated. For example, looking at the effect on mode 1 of subtracting

channels 180 degrees apart, Equation 3-3 becomes

$$P_{N_1} = \sin\left(\frac{2\pi j}{8}\right) - \sin\left(\frac{2\pi j}{8} + \pi\right) \quad (3-4)$$

Simplifying this expression, Equation 3-4 can be reduced to

$$P_{N_1} = 2\sin\left(\frac{2\pi j}{8}\right) \quad (3-5)$$

However, for mode 2, with $m=2$ and n still 4, Equation 3-3 becomes

$$P_{N_2} = \sin\left(\frac{j\pi}{2}\right) - \sin\left(\frac{j\pi}{2} + 2\pi\right) = 0 \quad (3-6)$$

Equation 3-6, when expanded equals zero for all values of j . Further examination of Equation 3-3 showed that for transducers spaced 180 degrees apart, the odd modes ($m = 1, 3, 5, \dots$) were doubled in amplitude, while all even modes ($m=0, 2, 4, \dots$) equal zero. Table 3-1 compiles the results of various angle combinations and their effect on the even and odd modes.

Table 3.1 Effects of Subtraction/Addition of Kulite Data

Method	Subtraction		Addition
	Amplitude Factor		
n, Angle Difference (deg)	2 (90)	4 (180)	4 (180)
Planar Waves	0X	0X	2X
Rotating Wave Odd Mode m = 1	1.4X	2X	0X
Rotating Wave Even Mode m = 2	2X	0X	2X
Rotor Frequency m = 1	1.4X	2X	0X

After testing this method for various angular positions (specifically 45, 90 and 180 degrees), it was determined that subtracting transducers 180 degrees apart produced the best results for analyzing the first mode. This subtraction process was applied to all data channels thus creating a new data file where the pressure for each channel can be expressed as follows:

$$\begin{aligned}
 P_{1N} &= P_1 - P_5 \\
 P_{2N} &= P_2 - P_6 \\
 P_{3N} &= P_3 - P_7 \\
 P_{4N} &= P_4 - P_8 \\
 P_{5N} &= P_5 - P_1 \\
 P_{6N} &= P_6 - P_2 \\
 P_{7N} &= P_7 - P_3 \\
 P_{8N} &= P_8 - P_4
 \end{aligned}$$

This new data set was then used to complete the analysis process.

3.5 Digital filtering

A digital filter was employed to eliminate the rotor frequency encountered during the analysis of each rotor and speed. This particular

frequency was believed to be the rotor frequency and not the 2nd harmonic of the first mode based on the subtraction method analysis described earlier.

The rotor frequency interfered greatly with any attempt to identify modal waves. To eliminate this frequency, while maintaining as much of the lower spectrum as possible, a digital low pass filter was used on the new subtracted channels.

This filter was a finite impulse response filter of order 96, employing a Hamming window. A FIR filter was employed to maintain the linear phase of the signal. The filter was created using the finite impulse response function within the Signal Analysis Toolbox from Matlab [17]. This functions calculates the coefficients of the filter. An M-file was designed to pass each data channel through the filter again employing the built-in filter command from the Signal Analysis Toolbox.

3.6 Spatial Fourier Transform

The spatial Fourier transform allows eight pressure channels to be characterized by a single set of parameters (amplitude, phase) at each point in time, The equation used for this analysis was developed by Garnier [6] and was used by Boyer et al. [5] and Hoying [17]. The equations is as follows:

$$C_k = \frac{1}{8} \sum_{n=0}^7 V_n e^{\frac{-2\pi i k n}{8}} \quad (3-7)$$

where C_k represents the complex spatial coefficient, V_n represents the pressure data at each angular position n , and k can vary from -3 to 4. As stated by Garnier [6], since the V_n is a real number, the C_{-k} and C_k are complex conjugates. Garnier [6] also indicated that the C_k possessed the phase and half the amplitude of the rotating modal wave, which is all the required information for this analysis. Therefore, as in the Garnier and Boyer study the C_k 's were used.

These complex spatial coefficients returned from Equation 3-7 are a mathematical representation of any rotating energy at a point in time. The magnitude of the coefficient represents the magnitude of that rotating energy and the phase angle of the coefficient represents the angular position of that magnitude.

Complex spatial coefficients (C_k) were calculated for each time step and plots of the spatial Fourier coefficient magnitude and the unwrapped phase were made versus time. The magnitude plot was used to determine when the rotor actually stalled. The stall point was always identified as the point of half the maximum SFC magnitude (Figure 3.1). Time was then re-scaled such that $t=0$ revs occurred at the point of stall. Thus any precursor

to stall was identified as negative time.

3.7 Phase tracking analysis

This portion of the analysis process was used to identify the presence of modal waves. As mentioned earlier, a form of this analysis technique was used by Boyer et al. [5] in an effort to quantify the precursor time. It relies on being able to track the phase speed which is the slope of the SFC phase plot. As this speed approaches 0.5/rev, the system is assumed to be near stall.

For this analysis, in this thesis, a moving average technique was used. A window of data 250 msec. in length from the phase and time data was selected. From this data the average slope was calculated as shown below and recorded against the final time value for the chosen window length. Then the window was stepped forward in time and the calculation was repeated.

To calculate the slope, the phase-time data were evaluated using a first order linear regression equation

$$\{p\} = a\{t\} + b \quad (3-8)$$

where p is a vector containing the phase data points and t is vector containing the time data points. Equation 3-8 can then be represented in matrix notation.

$$\begin{bmatrix} p_1 \\ \vdots \\ p_n \end{bmatrix} = a \begin{bmatrix} t_1 \\ \vdots \\ t_n \end{bmatrix} + b \quad (3-9)$$

Where n represents the window size used in the analysis. Equation 3-9 can be rearranged as follows:

$$\begin{bmatrix} p_1 \\ \vdots \\ p_n \end{bmatrix} = \begin{bmatrix} t_1 & 1 \\ \vdots & \vdots \\ t_n & 1 \end{bmatrix} \begin{bmatrix} a \\ b \end{bmatrix} \quad (3-10)$$

Transposing the 2 x n matrix and multiplying it by both sides returns 2 equations with two unknowns of which a represents the slope of interest and b is a y-intercept. The equation in matrix form is as follows:

$$\begin{bmatrix} \sum_{i=1}^n p_i \\ \sum_{i=1}^n p t_i \end{bmatrix} = \begin{bmatrix} n & \sum_{i=1}^n t_i \\ \sum_{i=1}^n t_i & \sum_{i=1}^n t_i^2 \end{bmatrix} \begin{bmatrix} a \\ b \end{bmatrix} \quad (3-11)$$

This equation was solved and the slope recorded for the highest value of time in the t vector. The window was then stepped in time 2.5 msec. (10 data points) and the process repeated. As stated earlier, the window size was 250. msec (1000 data points). The slope was then plotted against time.

3.8 System identification

System identification is a procedure normally used to construct a model for unpredictable or complex systems. These complex systems can take on many forms, to include the compressor fluid dynamics prior to stall. A system identification method was used by Garnier [12] in an effort to identify the modal waves as a precursor to stall. System identification was again used by Paduano [14] in his active control experiments. Hoying [17] also successfully used a system identification method to identify precursor time for a multistage high speed compressor analysis. Since the flow field of the transonic compressors used in this study is very complex, system identification was used in an effort to identify the point at which the modal waves first appeared.

The identification method used in this analysis was similar to that used by Hoying [17]. It was based on the recursive least squares method described in Ljung et al. [18]. The finite difference equation

$$y(t) + a_1 y(t-1) + \dots + a_n y(t-n) = b_1 u(t-1) + \dots + b_m u(t-m) + v(t) \quad (3-12)$$

where y represents the output spatial Fourier coefficient, $u(t)$ represents the input to the system (for this analysis $u=0$), and the a 's and b 's represent constants that minimize the error term $v(t)$. The number of terms used in this expression n , represents the order of the model. Using the notation

from Ljung et al [18], and allowing the parameter vector to be represented as

$$\Theta^T = (a_1 \dots a_n \ b_1 \dots b_m) \quad (3-13)$$

and introducing a vector of lagged input and output as

$$\phi^T = (-y(t-1) \dots -y(t-n) \ u(t-1) \dots u(t-m)) \quad (3-14)$$

Then Equation 3-14 can be rewritten as

$$y(t) = \Theta^T \phi(t) + v(t) \quad (3-15)$$

The least squares method is then used to minimize $v(t)$. Through a series of matrix manipulations, an equation of the form

$$\hat{\Theta} = \hat{\Theta}(t-1) + L(t)[y(t) - \hat{\Theta}^T(t-1)\phi(t)] \quad (3-16)$$

where the new $\hat{\Theta}$ represents approximate values which include some error.

Thus Equation 3-15 can be written

$$\hat{y}(t) = \hat{\Theta}^T \phi(t) \quad (3-17)$$

To solve for the new $\hat{\Theta}$, one must first solve for $L(t)$, the gain matrix and

$P(t)$, the covariance matrix. These equations are as follows:

$$L(t) = \frac{P(t-1)\Phi(t)}{\lambda + \Phi^T(t)P(t-1)\Phi(t)} \quad (3-18)$$

$$P(t) = \frac{1}{\lambda} \left[P(t-1) - \frac{P(t-1)\Phi(t)\Phi^T(t)P(t-1)}{\lambda + \Phi^T(t)P(t-1)\Phi(t)} \right] \quad (3-19)$$

The λ term in both equations 3-18 and 3-19 represents a "forgetting factor" that aides in the algorithm's ability to converge to the system of interest. This value of λ enables the algorithm to decrease the importance of older data. For example a λ value of 1.0 weights each data point equally, while decreasing λ , will decrease the influence of older time steps. However, $\lambda < 1.0$ also allows more error into the model calculation. This term usually ranges from $.95 < \lambda < 1.0$, and for this analysis it was set equal to 0.999.

The Equations 3-15, 3-17 and 3-18 were developed strictly for a real number analysis. To allow the use of this analysis technique with the spatial Fourier coefficients, the equations needed to be converted for use with complex numbers. This was accomplished using the least squares equation development from Marple [19]. By introducing the necessary conjugates, Equations 3-19 and Equation 3-18 were converted to

$$P(t) = \frac{1}{\lambda} \left[P(t-1) - \frac{P(t-1)\phi^*(t)\phi^T(t)P(t-1)}{\lambda + \phi^T(t)P(t-1)\phi^*(t)} \right] \quad (3-20)$$

$$L(t) = \frac{P(t-1)\phi^*(t)}{\lambda + \phi^T(t)P(t-1)\phi^*(t)} \quad (3-21)$$

where the * designates the conjugate of the vector and T the transpose without the conjugate.

This recursive operation returns values for $\hat{\Theta}$ for each time step. The number of $\hat{\Theta}$'s found is equal to the order of the model used. These values of $\hat{\Theta}$ can then be analyzed to identify the damping factor and frequency of the system model. This is accomplished by first constructing the equation

$$z^n + \hat{\Theta}_1 z^{n-1} + \dots + \hat{\Theta}_n = 0 \quad (3-22)$$

where n represents the order of the model. By solving for the poles of this equation a damping factor and frequency can be calculated using formulas taken from Marple [19].

$$DF(k) = \frac{\text{Ln}(|z(k)|)}{T} \quad (3-23)$$

$$Freq(k) = \arctan\left(\frac{\Im(z(k))}{\Re(z(k))}\right) * \frac{1}{2\pi T} \quad (3-24)$$

Where $k = 1$ to n , indicating that there are as many damping factors and frequencies as there are orders to the model. For this analysis the largest damping factor found at each time step is used and the first frequency corresponding to the first eigenvalue of Equation 3-22 was used. For this study a second order analysis was used.

3.9 Testing of the system identification method

In an effort to ensure the accuracy of the results of this analysis and in an effort to understand what the results would actually demonstrate, two simple tests were performed. The first was to construct a data stream that was generated by the Equation 3-25.

$$y(t) = a_1 y(t-1) + a_2 y(t-2) + \text{random noise} \quad (3-25)$$

The a_1 and a_2 were specified for this equation as complex values. The recursive least square algorithm was then applied to this data to identify the Θ 's (corresponding to a calculated a_1 and a_2) of the system. These Θ 's were within 0.5% error of the specified a_1 and a_2 for a 2000 data point sample.

The second test conducted for the algorithm was to generate a sine wave of known frequency (100 Hz) and again use the recursive least squares (RLS) algorithm to model the data. This test was done to see how well the output frequency calculated using Equation 3-23, matched the input

frequency. It was found that the system identification output was the exact frequency input for this data set.

This test was then re-run using a combination of two known frequencies of equal amplitude (100 Hz and 200 Hz). The results for this test was that the system tried to model both frequencies simultaneously and actually produced an output frequency that was the average of both frequencies.

The results of this simple test provided some valuable insight into the modeling ability of the recursive least squares algorithm. First, it demonstrated that the system would locate and track the most dominant frequency within the analysis data stream. Second, it demonstrated that the system identification method may not locate the exact frequency of the rotating wave, since it produced an average of all dominant frequencies present. Finally, it indicated that when evaluating real data a sharp or gradual change in frequency and the tendency for the frequency remain constant may be of more interest to the analysis process than the actual value of that frequency. This premise will be used later with the examination of output data.

One last point should be made about the damping factor produced by the system identification analysis. This value is a mathematical representation of the stability of the system. As long as the value produced is negative, the system is considered to be stable. If this value approaches

or crosses zero the system is becoming more unstable.

4.0 RESULTS

4.1 Introduction

The results for this report are presented by rotor, characterizing the stall process for each speed line. The resulting instability for each rotor and speed line was a surge-like phenomenon, which may or may not be related to a facility resonance. However, in each case the surge-like phenomenon was preceded by a brief period of rotating stall. This sequence, whereby rotating stall proceeded and appeared to trigger the surge agreed with the findings reported by Stenning [2] and Day et al. [3]. The period of rotating stall for Rotor 4 70% speed was longer than all other cases and was therefore used to perform all of the preliminary analysis.

The planar waves discussed in Boyer et al. [5] were found to be directly related to the surge-like phenomenon. The waves did not appear until the rotor began to become unstable and the system began to surge. These waves were noted to have a frequency of 13-14 Hz or 26-28 Hz. This indicated that the low frequency planar waves seen by Boyer [14] were not just a facility resonance, but result of the rotor instability most likely coupled with the facility which would account for the higher surge frequencies.

To eliminate the effect of these waves on the analysis process, the channel subtraction technique described in Section 3.4 was used. The results for this method for 90 degree and 180 degree subtraction as well as

180 degree addition are presented in Figure 4.1. The first figure (top left) represents the original data channel with no subtraction. The low frequency planar waves can be seen near zero. At approximately 120 Hz, one can see the rotating stall frequency, at approximately 240 Hz, the rotor frequency and possible second mode is visible, and finally at approximately 360 Hz there were indications of a possible third mode. For 90 degree subtraction (Figure 4.1, top right), the planar frequency was no longer present, while modes 1, 2 and 3 were amplified. For the 180 degree subtraction (Figure 4.1, bottom left), the planar wave was again eliminated, while for this case the second mode was also eliminated. Modes 1 and 3 were amplified. Finally, the 180 degree addition of channels (Figure 4.1, bottom right) was shown to amplify the planar wave as well as the second mode. The spike seen at 120 Hz is now no longer related to the first mode which was eliminated; it was 120 Hz power.

An effort was made to analyze both the first and second modes, without digital filtering. The data channels for Rotor 4 70% speed were subtracted using 90 degree channel subtraction, thus allowing all modes to remain while eliminating planar waves. After calculating the SFCs for both modes, the system identification procedure was used on the model the SFCs of both modes. The system identification results for this analysis are presented in Figure 4.2. Damping factor and frequency are plotted against time. As was discussed in Section 3.9, the damping factor is a

mathematical representation of the stability of the system being analyzed, while the frequency represents a weighted average of all frequencies present in the system. Prior to stall the rotor frequency normally dominated the frequency spectrum. This caused the frequency output from the system identification method to track higher frequencies and remain in that region until the 0.5/rev frequency became more dominant. The frequency then decreased at $t = -50$ revs and again just after stall when the rotating stall frequency dominated the frequency spectrum.

During this analysis, mode 2 did not appear to indicate any additional information that was not seen by examining mode 1. Therefore, to reduce computational time and eliminate the influence of the rotor frequency, the analysis focused on the first mode. Using 180 degree subtraction to eliminate planar effects, and double the amplitude of the first mode, and a digital lowpass filter (Described in Section 3.5) to eliminate the rotor frequency, the data channels were analyzed focusing on the first mode alone. Three different filter frequencies were used. They were 0.9/rev, 0.7/rev and 0.6/rev. The effects of filtering on the system identification output for mode 1 can be seen in Figures 4.3, 4.4 and 4.5.

By filtering at 0.9/rev, (Figure 4.3) the weighted average frequency was approximately 0.45/rev, which is very close to the frequency of interest, 0.5/rev. This made identifying any movement in frequency toward 0.5/rev very difficult. The damping factor showed its first zero crossing indicating

system instability at $t=50$ revs. This was the same indication seen prior to filtering the rotor frequency (Figure 4.2).

The results of filtering at 0.7/rev were shown in Figure 4.4. This reduced the averaged frequency to just above 0.4/rev which allowed better indications of a frequency change in the range of 0.5/rev. It also moved the damping factor closer to zero with the first zero crossing was now at approximately $t=130$. It will be shown later that this corresponds with the growth of the 0.5/rev frequency seen in pressure and SFC data.

Finally the lowpass filter was applied at 0.6/rev; the results of which are shown in Figure 4.5. The indications were again similar to those seen in Figure 4.4, however, the frequency indications were better using this lowpass frequency. However, the pre-stall modal frequency seen by Hoying [17] were in the range of 0.6/rev for first mode. Therefore, to prevent filtering off the frequencies of interest, 0.7/rev filter frequency was used.

4.2 Rotor 4

Rotor 4 was one of the two rotors included in the Boyer et al. [5] study. A comparison of rotating stall frequency between this study and the Boyer et al study [5] was done. The rotating stall frequency was within 1 Hz of the rotating stall frequency found by Boyer et al. [5] for each speed. This comparison was done to compare the results of the two studies since they were done with different data sets. However, as seen in Table 4-1. the

rotating stall frequencies compared well to those determined by Boyer et al. [5].

Table 4.1 Stall Frequency Comparison for Rotor 4

% Design Speed	Present Work	Boyer et al. [14]
70	.51/rev (123 Hz)	.52/rev (124 Hz)
80	.50/rev (139 Hz)	.53/rev (145 Hz)
90	.52/rev (163 Hz)	.53/rev (164 Hz)
100	.55/rev (193 Hz)	.56/rev (193 Hz)

This comparison indicated that the rotating stall frequencies identified during the analysis were characteristic of this rotor.

4.2.1 70% Speed

The magnitude of the spatial Fourier coefficient is plotted against time in Figure 4.6. This sharp increase in the magnitude at $t = 0.0$ revs was characterized as an abrupt stall. The unwrapped spatial Fourier coefficient phase is plotted against time in Figure 4.7. From this figure, it can be seen the linear growth that the phase maintained throughout the plot. However, at $t = -129$ revs, the slope appears to become equal to the slope seen after stall occurs.

Figure 4.8 is representative of the output of the phase tracking method described in Section 3.7. The phase speed (slope of Figure 4.7) is plotted against time. As can be seen in Figure 4.8, the phase speed approached 0.5/rev at approximately $t = -129$ revs as indicated in Figure

4.7, but it also approached 0.5/rev at $t = -300$, and $t=-200$ as well. This method was unreliable for determining a stall precursor value. For this reason, even though the analysis method was used the results were inconclusive for each case and only the plot for this case is presented.

One of the more valuable analytical tools used was the PSD analysis using windows of time. The results of windowed, unfiltered, pressure data utilizing 180 degree subtraction is presented in Figure 4.9. The rotor frequency can be seen at approximately 240 Hz, as well as the growth of the 0.5/rev frequency beginning to appear at $t=-160$ revs and growing in amplitude as stall was approached. The windowed results of 180 degree addition (second mode analysis) are also presented in Figure 4.10. The second mode did not appear until after the system has stalled. However, the low frequency planar affects appeared to grow as far back as -200 revs.

Finally the windowing method was applied to the SFCs. This in effect allowed for the examination of all the frequencies of the system and corresponded to the averaged frequency found using the system identification (Figure 4.4). (Note the system identification averages all the frequencies present at each time step) The spike seen at $t=-120$ revs agrees with the results found using the pressure data. However, the growth and decay of frequencies in this range as far back as -600 revs may indicate instabilities of the system much earlier.

From the overall analysis of rotor 4 70% speed, it was determined that the system identification method would be used to determine the precursor time, while the windowed frequency spectrum from the pressure and SFCs data would be used to as confirmation of those results. Therefore, using the system identification method a precursor time was determined to be approximately -133 revs. This value converts to 551.3 msec.

4.2.2 80% Speed

The stall for rotor 4 80% Speed was abrupt (Figure 4.12). There was little indication from the SFC magnitude growth that stall was approaching. The phase plot (Figure 4.13) showed an indication of phase change just before stall at $t = -48$ revs. The damping factor (Figure 4.14) was noted to increase several times just before stall. Though these increases were not much larger than the ones seen at $t = -105$, they were accompanied by a frequency change toward 0.5/rev. The PSD analysis of the pressure data (Figure 4.15) confirmed the existence of the frequency of interest (0.5/rev, 139 Hz) at approximately $t = -9$ revs while the PSD of the SFCs (Figure 4.16) indicated frequencies in the area of interest, however, determining a time of origination was not possible. Therefore, for rotor 4 80% speed, a value of $t = -48$ revs was used as the precursor. This corresponded to approximately 173 msec of stall warning time.

4.2.3 90% Speed

The stall for rotor 4 90% Speed was again an abrupt stall (Figure 4.17). There was no growth seen in the magnitude until stall occurred. The phase versus time plot (Figure 4.18) also gave no indication of stall. The system identification plot (Figure 4.19) showed an increase in damping factor at $t = -109$, however the increases in damping factor at $t = -27$ were closer to zero and appeared to be a more conservative estimate of the stall precursor time for this case. The PSD of pressure (Figure 4.20) showed no indication of stall approaching. The PSD of SFCs (Figure 4.21) did show slight frequency increases at $t = -25$ and growing up to stall.

Using the combined analysis from all methods yielded a stall precursor time of -27 revs which equated to approximately 86 msec.

4.2.4 100% Speed

Rotor 4 100% speed was characterized by an abrupt stall (Figure 4.22). As with the previous case, the magnitude and phase plot (Figure 4.23) showed no indication of stall approaching. However, unlike the other cases described above, the system identification plot (Figure 4.24), the windowed frequency of pressure signals (Figure 4.25) and the windowed frequency of SFCs (Figure 4.26) did not show stall indications either. Figure 4.24 showed no growth in damping factor or frequency change until stall. Figure 4.25 showed multiple frequencies in the area of 182 Hz. However, the 182 Hz stall frequency does not appear until after stall.

Figure 4.26 showed numerous frequencies from which a determination of stall precursor could not be made. Therefore for rotor 4 100% speed no stall precursor was determined.

4.3 Rotor 6

Rotor 6 was characterized by a mixture of stall types, progressive and abrupt. Again the rotating stall frequencies found in the Boyer et al. [14] study, were relatively the same as those found in this study. Table 4.2 compares the results for rotor 6, rotating stall frequencies for the two studies.

Table 4.2 Stall Frequency Comparison for Rotor 6

% Design Speed	Present Work	Boyer et al. [14]
70	.50/rev (121 Hz)	.50/rev (120 Hz)
80	.54/rev (150 Hz)	-----
90	.50/rev (158 Hz)	.50/rev (155 Hz)
100	.56/rev (197 Hz)	.50/rev (173 Hz)

4.3.1 70% Speed

The stall for rotor 6 70% speed was a progressive stall (Figure 4.27). Viewing the magnitude plot alone the system began to become unstable at $t = -450$ revs. Viewing the phase versus time plot (Figure 4.28), there appeared to be linear growth in phase throughout the data sample. The system identification output (Figure 4.29) showed the first zero crossing of the damping factor at $t = -446$, while the frequency appeared to remain at

0.45/rev to 0.5/rev from that point until stall. Both the PSD of the pressure signal (Figure 4.30) and the PSD of the SFCs (Figure 4.31) showed early indications of a frequency in the area of 0.5/rev (121 Hz). From Figure 4.31, it was more apparent that this growth began at or around $t = -450$ revs. Using the combined results from each method, a precursor time of $t = -450$ was determined for this case. This corresponded to 1853 msec of stall warning time.

4.3.2 80% Speed

This case was characterized by an abrupt stall (Figure 4.32). The magnitude plot gave no indication of stall warning, however, the phase plot (Figure 4.33) slope appears to become linear at $t = -95$ revs. The system identification output (Figure 4.34) showed zero crossings as early as $t = -600$ revs but did not have a corresponding frequency change toward 0.5/rev until $t = -80$. The PSD of the pressure (Figure 4.35) and the PSD of the SFCs (Figure 4.36) showed indications of stall at $t = -20$ revs but the amplitude of this frequency appeared to be about noise level at earlier times. For this case the value of $t = -80$ was used to identify stall precursor and corresponded to a stall warning time of 288 msec.

4.3.4 90% Speed

Rotor 9 at 90% speed was characterized by a mixed progressive and abrupt stall (Figure 4.37). At approximately $t = -1000$ revs, the magnitude plot began to show signs of growth or instability. This was then followed

by a sharp growth in magnitude at stall characteristic of an abrupt stall. The phase plot (Figure 4.38) showed linear growth up to stall. The system identification plot (Figure 4.39) showed the first zero crossing of the damping factor at $t = -1200$ revs and the frequency remained constant at 0.45/rev. The PSD of the pressure signals (Figure 4.40) and the PSD of the SFCs (Figure 4.41) each showed growth in the 0.5/rev as early as $t = -600$ revs. Using the output from the system identification a precursor time of $t = -1200$ revs was determined. This corresponded to a stall warning time of 3810 msec.

4.3.4 100% Speed

The stall for rotor 6 at 100% Speed was abrupt (Figure 4.42) as can be seen when viewing the sharp growth in SFC magnitude. This plot along with the phase plots (Figure 4.43) gave no indication of approaching stall. The damping factor and frequency (Figure 4.44) also gave no indication of stall approaching. There was no increase in damping factor or frequency as seen with the other case. The PSD of the pressure signal (Figure 4.45) and the PSD of the SFCs (Figure 4.46) also showed no stall precursor indications. Therefore as with rotor 4 at 100% speed no stall warning time was found.

4.4 Rotor 8

Rotor 8 like rotor 6 was backward swept. As seen with rotor 6, both progressive and abrupt stalls were seen with this rotor. The rotating stall

frequencies for this rotor ranged from 0.49 to 0.54/rev which was comparable with the results seen on rotor 6.

4.4.1 80% Speed

The stall at 80% speed was progressive as seen in the magnitude versus time plot (Figure 4.47). The phase plot (Figure 4.48) showed growth phase from approximately $t = -388$ revs, which agreed with the damping factor frequency indications from the system identification plot (Figure 4.49). The windowed PSD of pressure and SFCs (Figures 4.50 and 4.51) each confirmed these indications. Therefore, the precursor time for this case was $t = -388$ revs corresponding to 1426 msec.

4.4.2 90% Speed

The 90% case presented some problems for analysis. The data for this sample contained a very short period (approximately 2 seconds) of unstalled flow before the rotor stalled at which point the data sample was terminated. This limited the value of the system identification output since it requires a significant amount of data before it will converge to the system of interest.

The stall for this speed was again a progressive stall. This can be seen in the SFC magnitude versus time plot (Figure 4.52). The SFC phase plot (Figure 4.53) showed signs of linear growth at $t = -100$ revs. The magnitude plot (Figure 4.52) showed increases in the magnitude as early as $t = -400$ revs. The windowed PSD of pressure and SFCs (Figures 4.54 and

4.55) also indicated the presents of the frequencies in the area of 162 Hz (0.52/rev) as early as $t = -400$ revs. It would then appear that a stall precursor could be identified earlier than this data sampled would allow, however for this study a value of $t = -400$ revs will be used. This value corresponds to 1149 msec. in stall warning time.

4.4.3 100% Speed

This case like the two previous 100% speed cases was characterized by an abrupt stall (Figure 4.57). The phase plot (Figure 4.58) showed no phase change from approximately $t = -600$ revs until stall. The damping factor and frequency from the system identification also showed no precursor to stall (Figure 4.59). This was also confirmed using the windowed PSD of pressure and SFCs (Figures 4.60 and 4.61). On each of these plots only a small period of time near stall was examined. In both plots, no rotating wave frequencies were noted prior to stall. Therefore, like the two rotors examined above no stall warning time was determined for rotor 8 100% speed.

4.5 Rotor 9

Rotor 9 was the only forward-swept rotor examined for this study. It was characterized by a mixed progressive/abrupt stall at the 80% speed, and abrupt stalls for the 90% and 100% speeds. The rotating stall frequency for the 80% and 90% speeds were .52/rev and .50/rev, respectively. These values were within the range seen for the other rotors. Also, as seen with

the other rotors the 100% speed had a higher rotating stall frequency than the lower speed lines. However, with a rotating stall frequency of 0.7/rev it was significantly higher than the other rotors at this design speed.

During the analysis of rotor 9, an interesting phenomenon was observed. The output of the SFC phase plot for 80 and 90% speed (Figures 4.63 and 4.66) had significant regions of negative slope. This slope change at 90% speed corresponded with the initial detection of the 0.5/rev frequency found using the PSD analysis. These phase plots were unlike any of the plots found for the backward and straight leading edge rotors. For the 100% speed (Figure 4.71), there was no large negative slope, however, at $t = -89$ revs, the slope did appear to become negative up to the point of stall. Since this negative slope was consistent for each speed, it was used as the indicator of instability.

4.5.1 80% Speed

Rotor 9 80% speed was characterized by a mixed progressive/abrupt stall. The magnitude versus time plot (Figure 4.62) showed gradual increases from $t = -1500$ and then a sharp increase at stall. The phase plot (Figure 4.63) showed the negative slope mentioned above with the trend beginning as early as $t = -2000$ revs. The damping factor increased to near zero at approximately $t = -900$ revs (Figure 4.64) while the frequency tried to track the many frequency changes as seen on the SFC phase plot (Figure 4.63). The numerous frequencies present in this system can best be viewed

in the windowed pressure and SFCs data (Figure 4.66 and 4.67).

Specifically, the frequencies seen in the system identification plot were a weighted average of the frequencies displayed in Figure 4.67. For a stall precursor determination, the damping factor increase at $t = -900$ was used and corresponded to a stall warning time of 3270 msec.

4.5.2 90% Speed

Rotor 9 90% was characterized by an abrupt stall (Figure 4.65). The phase was again found to have a significant period of negative slope (Figure 4.66). The negative slope began at approximately $t = -780$ revs and continued until stall. The system identification output (Figure 4.67) indicated this same value, with movements of frequency and damping factor at approximately the same point in time. The windowed PSD of pressure indicated this with the amplitude growth at 156 Hz. This frequency first appeared at $t = -771$ revs and grew up to the point of stall.

It was also noted that a low frequency (35 Hz) occurred at stall. This was not function of the surge-like phenomenon since the planar waves were subtracted out for this analysis. More discussion of this low frequency will be done in the 100% speed case.

For this particular case, the precursor signal was identified at $t = -780$ revs. This value corresponded to a stall warning time of 2504 msec.

4.5.3 100% Speed

This case like all other 100% speed cases was characterized by an abrupt stall (Figure 4.70). The phase for this case had a positive growth until just prior to stall where it became flat or possibly negative (Figure 4.71). The system identification output showed changes in damping factor and frequency at $t = -49$ revs. The windowed PSD of the pressure and SFCs appeared to show indications of the rotating stall frequency at $t = -236$ revs. It was also noted that the low frequency wave seen at 35 Hz was recognizable at approximately $t = -660$ revs and grew as stall was approached. Further examination of this wave showed that this frequency was not the surge frequency (Figure 4.76 and 4.77). However, whether this frequency was due to a modal wave or an interaction between the rotor and test facility was not determined during this study. The fact that this low frequency was not eliminated during the channel subtraction indicated that it was rotating or out of phase from other channels.

Since the origin of the 35 Hz wave was unknown, the value of stall precursor from the system identification output was used. This value ($t = -49$) equated to 140 msec of stall warning.

4.6 Summary of results

Table 4.3 was compiled to give a comparison of the four rotors and the results at the various speeds tested.

Table 4.3 Rotor Comparison Table

Rotor	Speed	RPM	Rotor Freq Hz	Stall Freq Hz	Stall Type	Modal Waves	Prec Time msec
4	70	14475	241.2	123	Abr	Yes	551
	80	16638	277.3	139	Abr	Yes	173
	90	18804	313.4	155	Abr	Yes	86
	100	21030	350.5	182	Abr	Unkn	---
6	70	14568	242.8	121	Prog	Yes	1853
	80	16692	278.2	150	Abrupt	Yes	288
	90	18900	315	158	Prg/Abr	Yes	3810
	100	21099	351.6	197	Abr	Unkn	---
8	80	16335	272.1	177	Prog	Yes	1426
	90	18672	311.2	162	Prog	Yes	1149
	100	20880	348	188	Abrupt	Unkn	---
9	80	16512	275.2	143.1	Prg/Abr	Yes	3270
	90	18690	311.5	156	Abr	Yes	2504
	100	21006	350	245	Abr	Yes	140

The rotating stall frequency for each of the rotors and speeds was approximately 0.5/rev. The stall type seen at each speed varied with the exception of the 100% speed. This speed resulted in an abrupt for all rotors tested. This speed also resulted in no precursor time for rotors 4, 6 and 8, and only 140 msec. for rotor 9. For rotors 4, 6 and 8 at 100%, the presence of each modal waves was listed as unknown since each analysis method did not find indications of their presence.

Each of the swept rotors 6, 8, and 9 had notably more precursor time than seen for the baseline, rotor 4 which was un-swept. Rotor 9 in

particular, had a significant increase in the amount of stall warning time when compared to rotor 4. This increase occurred at both the low speed where the stall was somewhat progressive in nature, but also at the higher speeds where the stall was abrupt.

The precursor time for Rotor 6 and 8 had significant increases when the stalls were progressive, but the results were not as significant when the stall was abrupt.

5.0 CONCLUSIONS AND RECOMMENDATIONS

5.1 Discussion

5.1.1 Analysis methods

Several new innovative methods were used in this study. The first was windowing the frequency spectrum during the Power Spectrum Density analysis. This method aided the signal analysis of the frequency domain by not allowing frequencies to be influenced by past data. In this way, the modal frequencies could be detected at times when their amplitude would have been significantly lower than the other frequencies present, if the whole time history was analyzed simultaneously.

The second new method was the channel subtraction method. This technique provided an excellent way of eliminating the influence of the planar frequencies from the surge cycles while maintaining the integrity of the rotating content of the signal. It also provided a means for eliminating and isolating particular modes of the rotating wave for further study.

Several different methods were used to analyze SFC coefficients to identify the rotating waves for stall warning. The results of the present study did not identify any single superior method. The system identification method showed the most promise, however one of its limitations was identifying an averaged frequency for the entire data set.

This prevented the system identification method from converging to the correct frequency until the onset of stall.

5.1.2 Rotor characterization

The stall type recorded in Table 4.3 for each rotor was determined using the SFC magnitude plot as described in section 1.2. Comparing the stall type found using this method with the compressor maps for each of the four rotors (Figures 5.1 - 5.4) studied showed that this was a valid characterization. As an example, Figure 5.2 showed the 80% speed line for rotor 6 to have little or no positive slope to its characteristic (Abrupt stall Figure 1.2). This was also the determination found using the SFC magnitude. In contrast, the rotor 6 90% speed line had a fairly large period of positive slope (Progressive stall Figure 1.2). The SFC in this case demonstrated a mixed progressive/abrupt stall. This comparison can be made for each of the other rotors and speed lines with similar results.

Precursor time also appeared to be related to the speed line characteristic for each rotor. As found by Boyer et al. [14], speed lines with less negatively sloped regions had more stall warning time. The findings of Day [10], indicated that modal waves were not present in his analysis until the rotor had reached peak performance. This indicated that rotors with speed line characteristics that appear flat or having regions of positive slope would provide much longer periods of modal waves before stalling. This was confirmed in this study.

The compressor map for Rotor 9 is shown in Figure 5.4. (Note the flat appearance of the 80% and 90% speed lines) These two speed lines were found to possess some of the largest values of stall warning indicating the presence of modal frequencies earlier than the other rotors. In Figure 5.2, the 90% speed line for rotor 6 is shown to have a significant portion with positive slope, this sample too possessed a considerably high value of stall precursor.

In contrast, the 100% speed cases for rotor 4, 6 and 8 yielded no precursor and their speed line characteristics had much higher negative slope and little or no positive slope. The exception to this was the 100% speed line of rotor 9 (Figure 5.4) which also had a highly negative slope but a fairly flat response once it reached its peak performance value.

It was not determined if the negative slopes seen in the SFC phase plots and the negative frequency seen in the system identification plots for rotor 9 possessed any physical meaning. Further analysis of this rotor is required to better understand these results.

5.2 Conclusions

First, the results of this study appear to reinforce the conclusion found by Day [10]. He found that the appearance of modal waves was dependent upon the operating point location on the compressor map. In fact, the waves did not appear until the compressor was near its peak pressure rise. This study found that for compressor rotors which continued

to operate beyond the peak pressure rise (e.g. Rotor 6 90% and Rotor 9 90%), there was an increased value of stall warning.

Secondly, the analysis found modal waves for all cases except the 100% speeds of rotor 4, 6, and 8. For these three cases, the analysis methods used in this study could not identify the waves or frequencies prior to stall. However, for the all other cases the modal waves preceded the stall event. This indicated that even if these waves are not coupled to the stall event, the waves can still be used as a precursor to the stall event. This uncoupling of the stall and modal waves would not allow for the extended operating region found by Paudano [13], but would allow for the decrease of the stall margin and the ability to operate closer to stall than previously allowed.

Third, the use of the channel subtraction method provided an excellent analysis tool. Its ability to eliminate planar effects while amplifying the rotating frequencies was invaluable to this study. It could also be used to isolate the modes of interest. The technique used with the addition of channels did allow for the elimination of the rotor frequency, but amplified planar effects and eliminated the odd modes. Its further use is yet to be determined.

Of the rotors characterized in the study, rotor 9 demonstrated the most interesting results. It consistently possessed a higher value of precursor to stall while operating over much wider regions of flow rate. The

negative slope of the SFC Phase plot requires more study to determine the physical indications of this slope. With the blades swept forward, it is difficult to ascertain the meaning of these negative slopes.

For the backward swept rotors (6 and 8), the results were mixed for various speed lines. However, the relationship between the speed line shape and the stall precursor was evident when comparing these two rotors. In particular, the swept rotors allowed for more stall warning than the unswept rotor. This indicated that there is some interaction between the stall and the shock waves that these transonic rotors experience.

5.3 Recommendations

This study found that the forward swept rotor provided more stall warning than the straight or backward swept rotors. This could be due to where the stall first occurred (tip or hub), or the stall cell-shock wave interaction. Also the physical relationship between the negative slope of the SFC Phase plot and the rotational flow deserves more attention than received by this study. The change in slope was found to correspond to the emergence of the 0.5/rev frequency during the PSD analysis but why the slope had a negative value has not been determined. In addition, the use of the negative slope as a indicator for stall precursor could be a valuable tool.

An investigation into the hysteresis of these compressors is necessary to determine the value of tracking these modal waves for use as stall precursor. If the emergence of the modal wave occurs at the peak pressure

rise, then identifying these waves may not allow the stall process to be reversed. Therefore, an analysis of stall precursor data along with simultaneously recorded flow rate data would enable an evaluation of this type to be made.

More analysis of the channel subtracting method is needed to evaluate the possibility of using it during the data collection process. This would eliminate one of the digital calculations performed during the analysis process.

The correlation between the stall and the shock structure of the rotors requires more investigation. This would identify any interaction between the modal waves seen in this study and the shock waves associated with these speeds.

Further analysis using modified techniques to those used in this study could provide additional information. Specifically, additional examination of the even modes (0 and 2), the use of smaller time windows in for the frequency analysis, and the use of higher order models for the system identification.

Additional recommendations include reexamining the data at higher frequencies, specifically above the 1 KHz, and performing the signal analysis with other signal processing techniques to isolate harmonics. These additional methods could included Gaussian-based transforms or wavelet transforms.

Finally, an examination of why a particular rotor was noted to have progressive stall at one speed and an abrupt stall at a lower rotational speed needs to be accomplished. Since progressive stall was only seen on the swept rotors, there was obviously a relationship between the stall and shock waves. This relationship also requires further study.

6.0 REFERENCES

1. Coppenhaver, W. W., "Stage Effects on Stalling and Recovery of a High Speed 10-Stage Axial-flow Compressor," WRDC-TR-90-2054, June 1990.
2. Stenning, A. H., "Rotating Surge and Stall," *Transactions of the ASME Journal of Fluids Engineering*, Vol 102, March 1980, pp. 14-20.
3. Day, I.J., and Freeman, C., "The Unstable Behavior of Low and High Speed Compressors", ASME 93-GT-26, May 1993.
4. Emmons, H.W., Pearson, C.E., and Grant, H.P., "Compressor Surge and Stall Propagation," *Transaction of the ASME*, Vol. 77, May 1955, pp. 455-469.
5. Boyer, K.M., King, P. I., and Coppenhaver, W. W, "Stall Inception in Single Stage, High Speed Compressors with Straight and Swept Leading Edges," AIAA 93-2386, 29th Joint Propulsion Conference and Exhibit, Jun 1993.
6. Garnier, V H., "Experimental Investigation of Rotating Waves as a Rotating Stall Inception Indication in Compressors," GTL Report #198, November 1989.
7. Pampreen, R C. *Compressor Surge and Stall*. Norwich Vermont: Concepts ETI Inc, 1993.
8. Greitzer, E.M., "Surge and Rotating Stall in Axial Flow Compressors, Part I Theoretical Compression System Model," *Transactions of the ASME Journal of Engineering for Power*, Vol 98, April 1976, pp. 190-198.
9. Greitzer, E.M., "Surge and Rotating Stall in Axial Flow Compressors, Part II Experimental Results and Comparison with Theory," *Transactions of the ASME Journal of Engineering for Power*, Vol 98, April 1976, pp. 199-217.
10. Day, I.J., " Stall Inception in Axial Compressors." 91-Gt-86, June 1986.

11. Moore, F.K. and Greitzer, E.M., "A Theory of Post-Stall Transients in Multistage Axial Compression Systems," NASA Contractor Report 3878, March 1985.
12. McDougall, N. M., Cumpsty, N.A., and Hynes T.P., "Stall Inception in Axial Compressors," *Transactions of the ASME, Journal of Turbomachinery*, Vol 112, January 1990, pp 116-125.
13. Paduano, J. D., "Active Control of Rotating Stall in Axial Compressors, PhD Thesis, MIT Dept of Aeronautics and Astronautics, February 1992.
14. Boyer, K. M., "Characterization of Stall Inception in High-Speed Single Stage Compressors," Master's thesis, AFIT/GAE/ENY/92D-21, Air Force Institute of Technology, Dec, 1992.
15. *MATLAB*, South Natick, MA: The MathWorks Inc., 1993.
16. Little, J., and Shure, L., *Signal Analysis Toolbox for Use with MATLAB™*, South Natick, MA: The MathWorks Inc., August 29, 1988.
17. Hoying, D A., "Stall Inception in a Multistage High Speed Axial Compressor," AIAA 93-2386, 29th Joint Propulsion Conference and Exhibit, Jun 1993.
18. Ljung, L., and Söderström, T., *Theory and Practice of Recursive Identification*. Cambridge, MA., MIT Press: 1983.
19. Marple, S. L., Jr., *Digital Spectral Analysis with Applications*. Englewood Cliffs, NJ., Prentice-Hall: 1987.

7.0 FIGURES

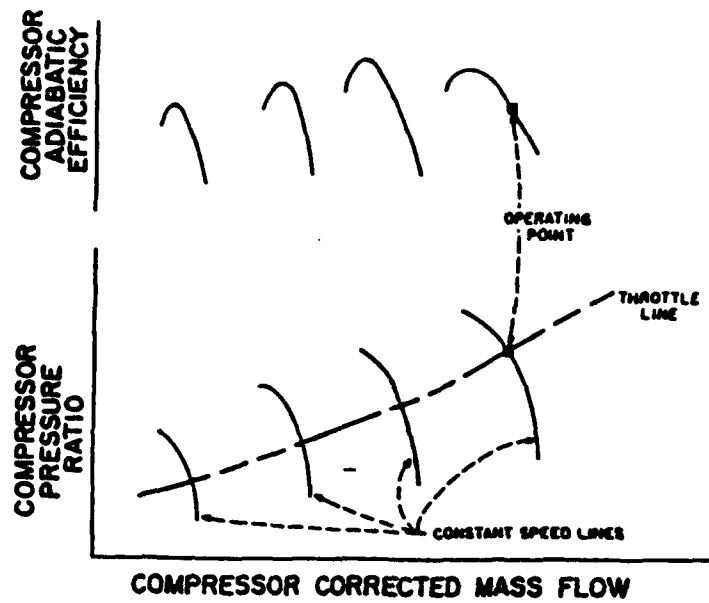


Figure 1.1 Compressor Map with Pressure Rise and Efficiency
Copenhaver [1]

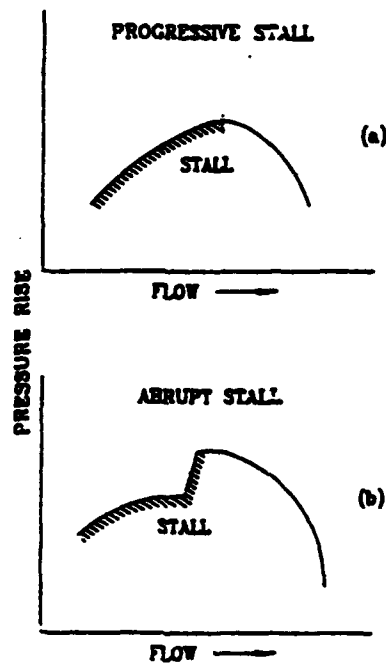


Figure 1.2 Abrupt/Progressive Stall
Pampreen [7]

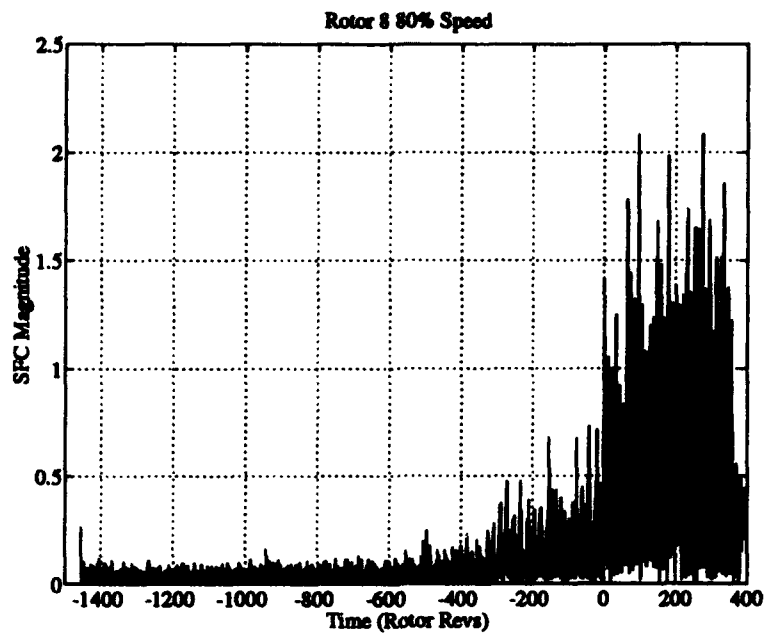


Figure 1.3 Example of Progressive Stall

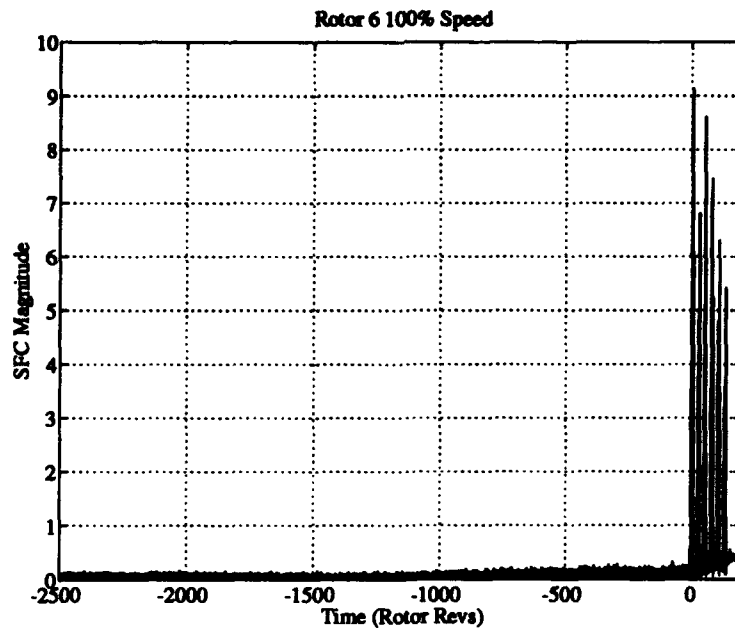


Figure 1.4 Example of Abrupt Stall

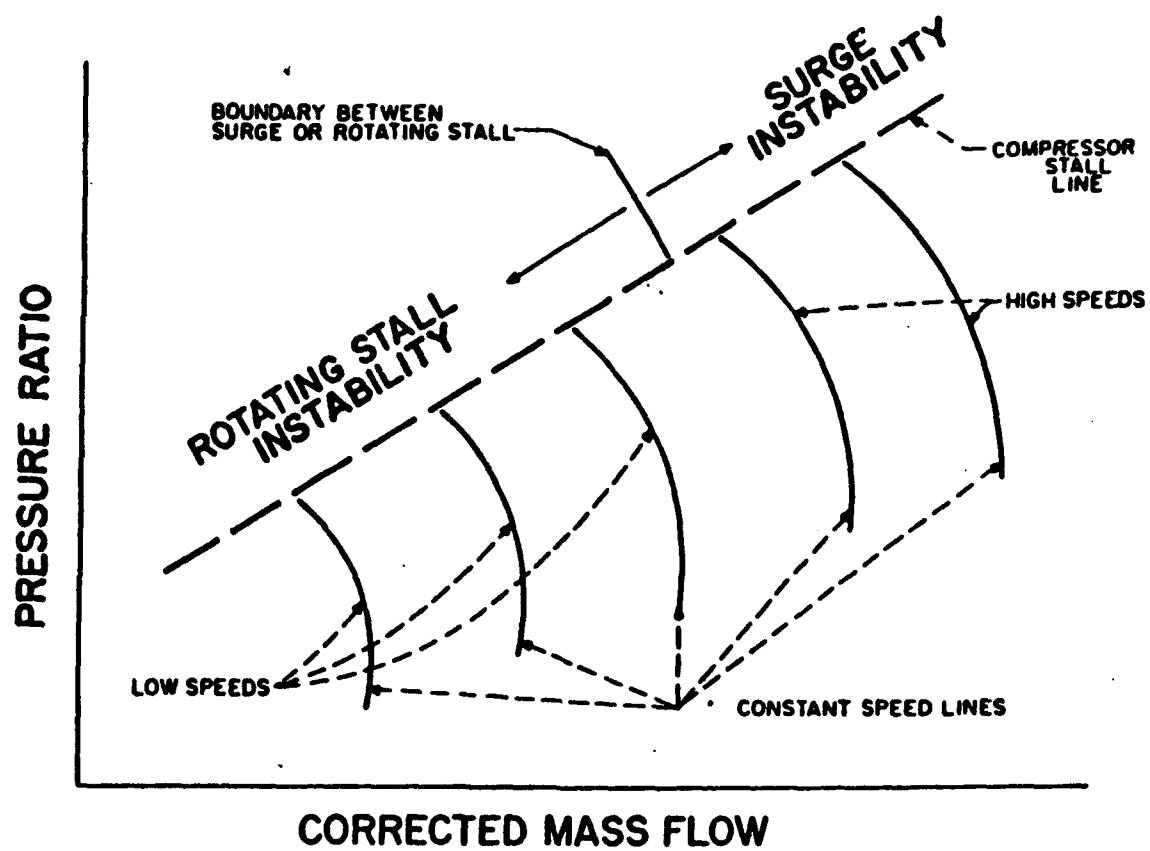


Figure 1.5 Compressor Surge/Rotating Stall Boundary
Copenhaver [1]

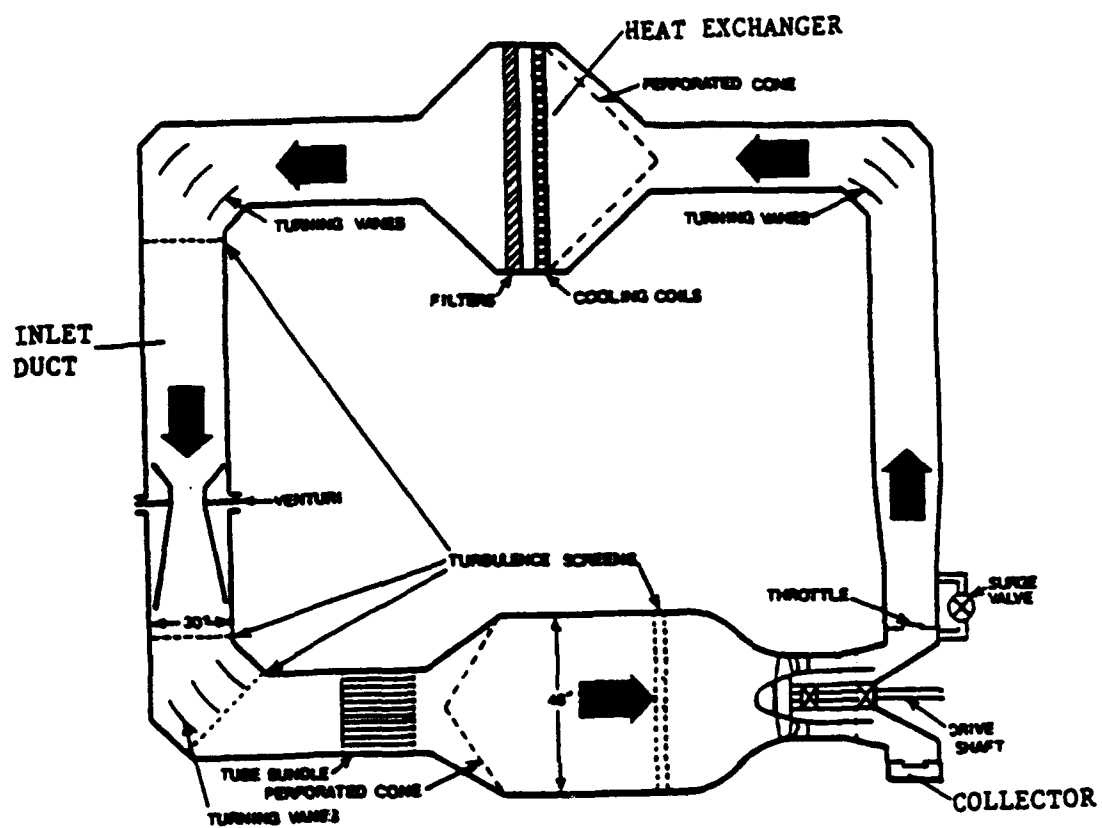


Figure 2.1 Schematic of CARL Facility

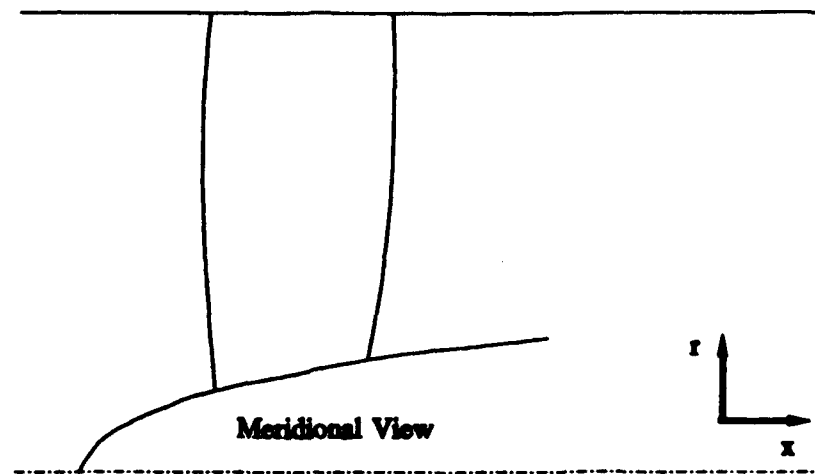


Figure 2.2 Sketch of Rotor 4

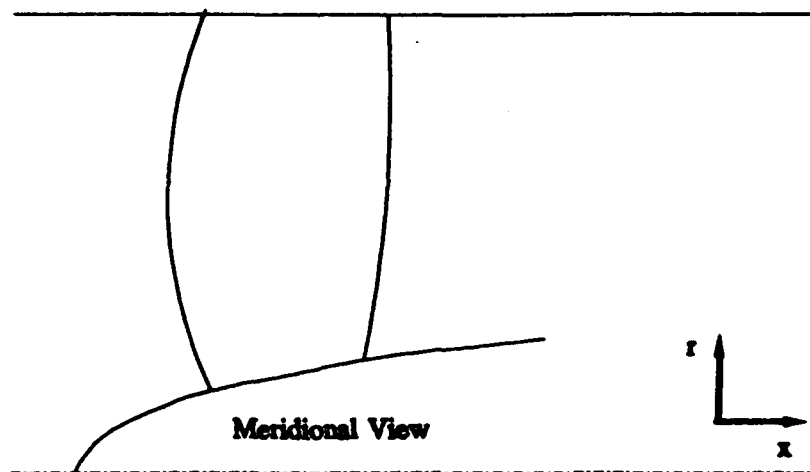


Figure 2.2 Sketch of Rotor 6

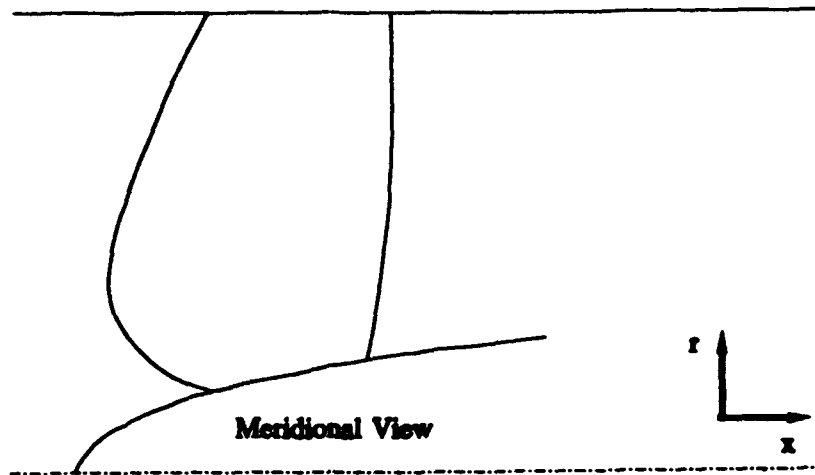


Figure 2.4 Sketch of Rotor 8

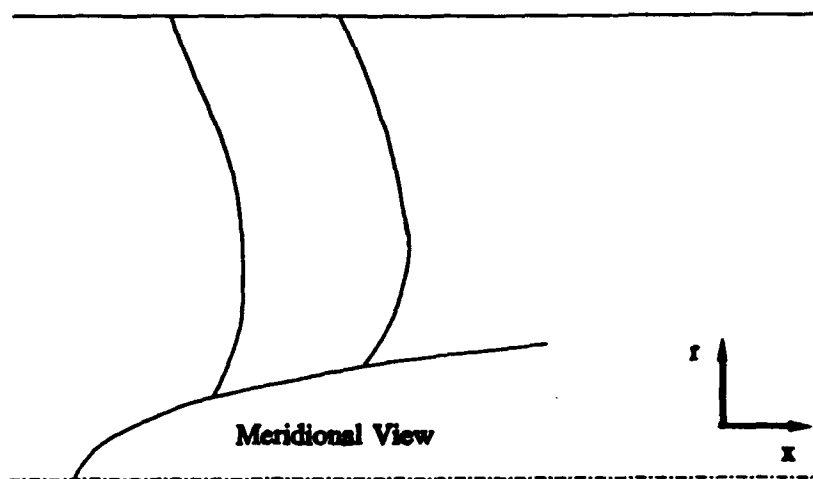


Figure 2.5 Sketch of Rotor 9

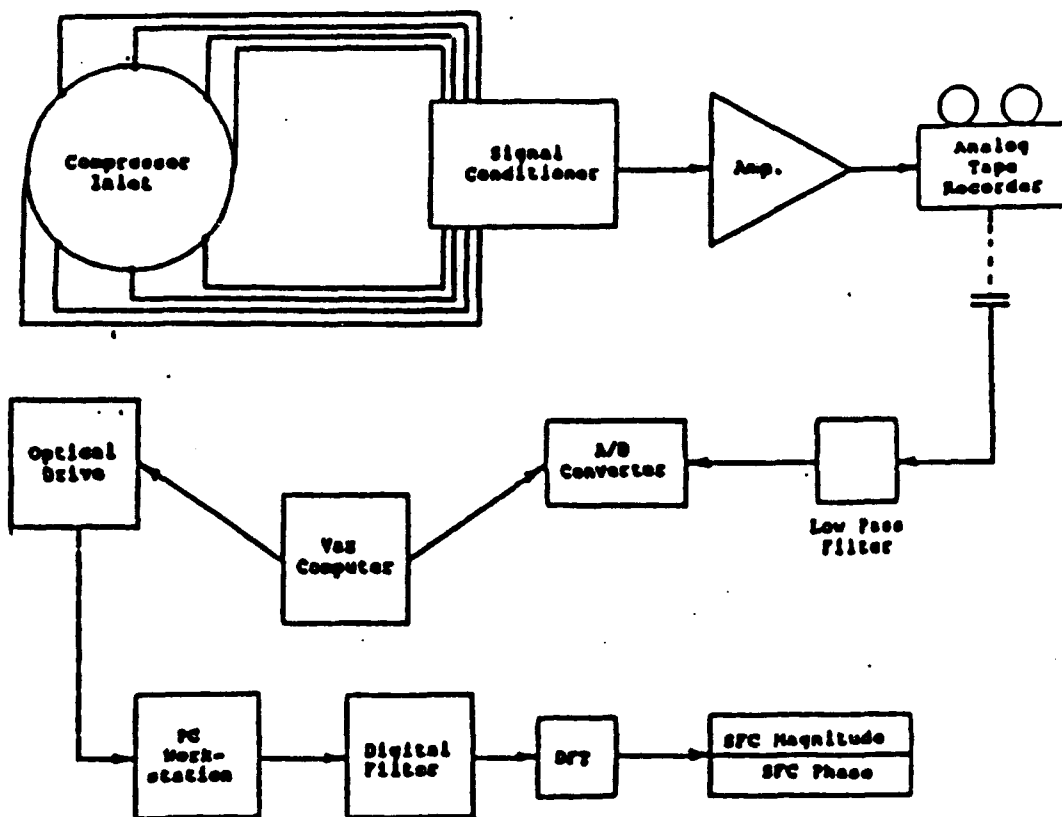


Figure 2.6 Pressure Signal Processing
Boyer et al. [14]

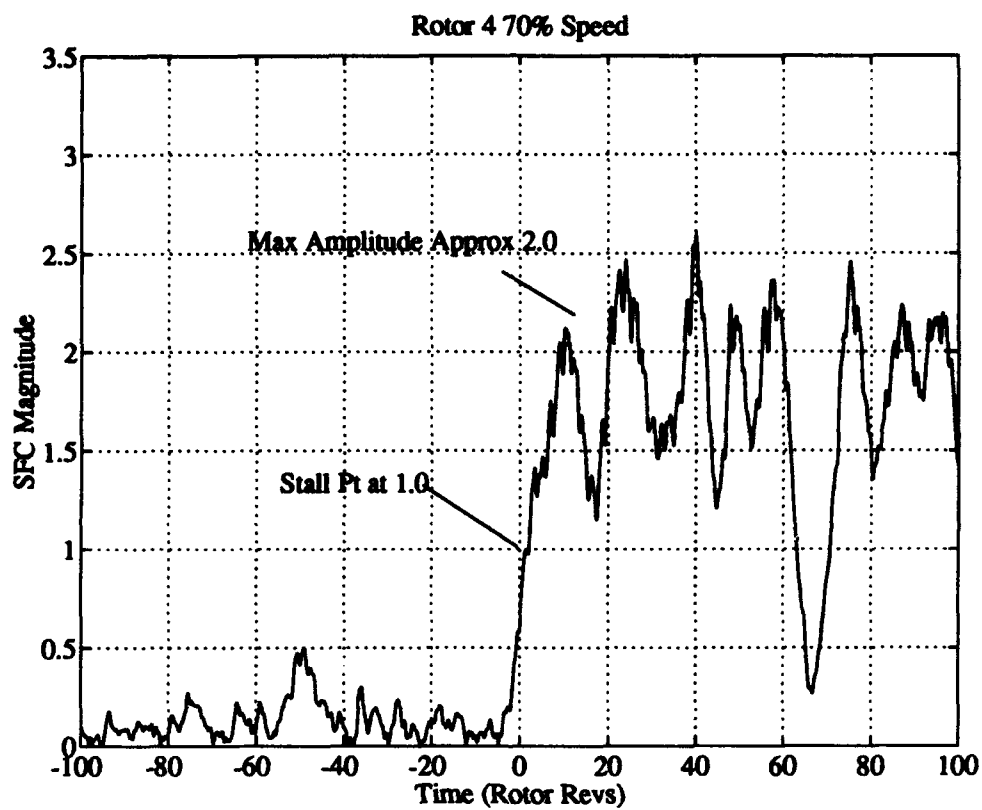


Figure 3.1 Example of Stall Point Location

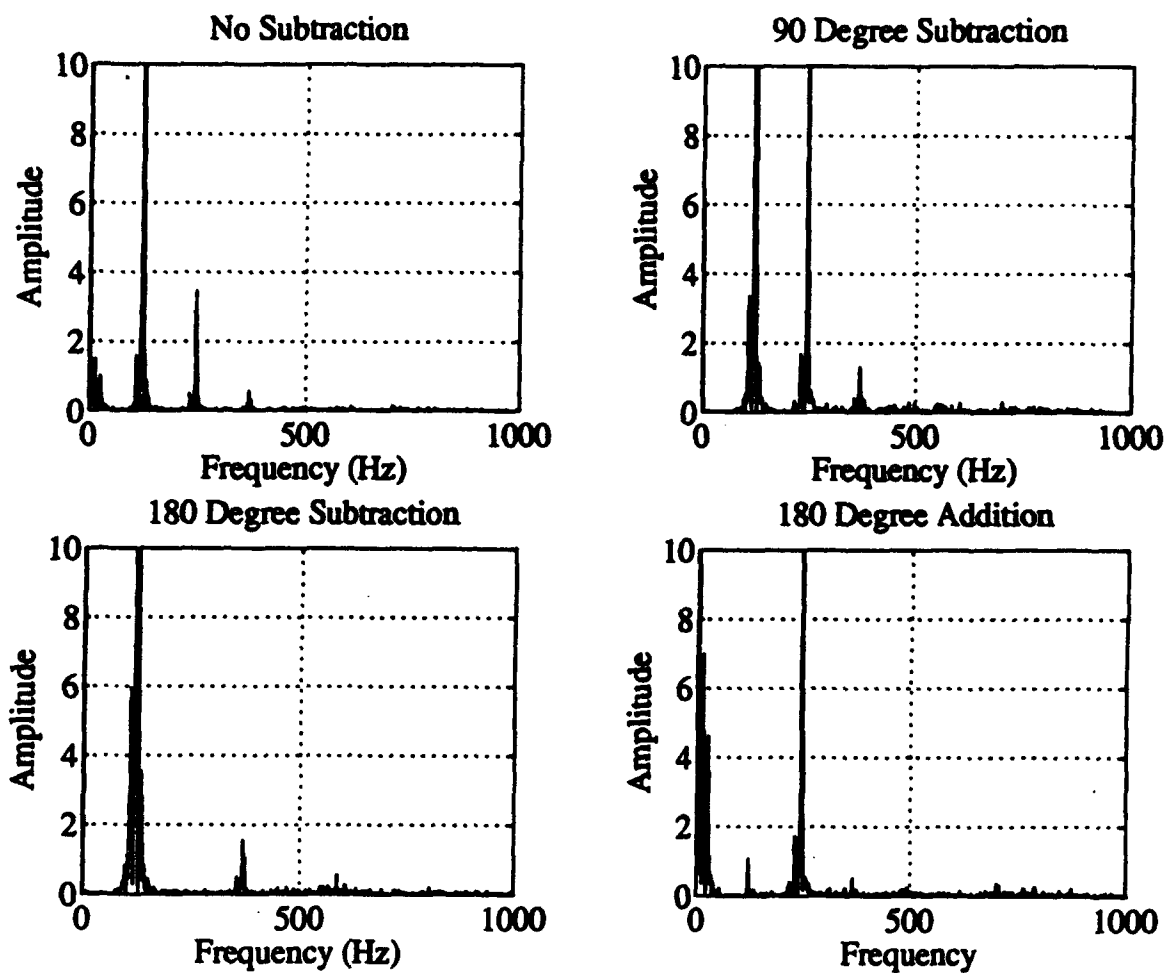


Figure 4.1 Channel Subtraction/Addition Results

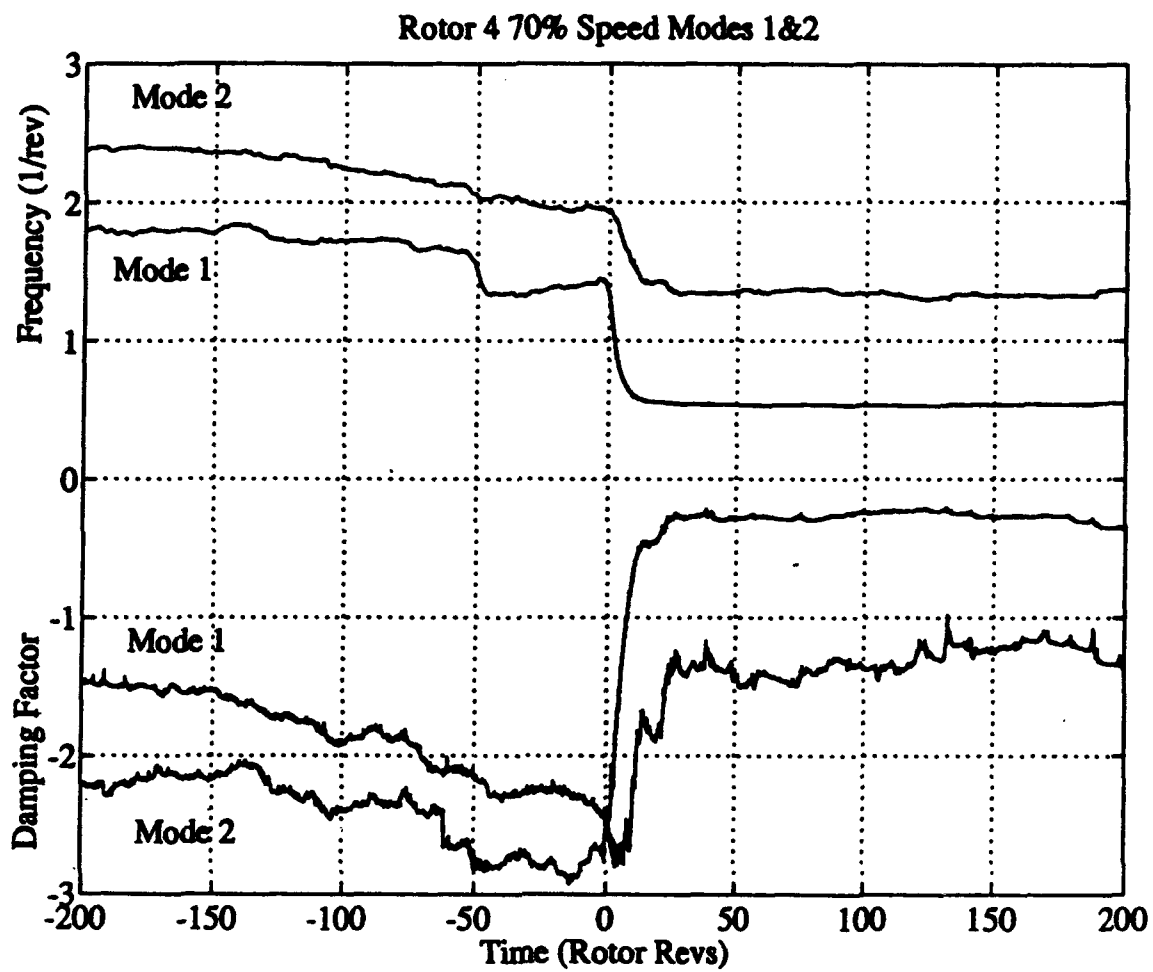


Figure 4.2 Frequency and Damping Factor - 1st And 2nd Mode -Rotor 4 70% Speed without lowpass Filtering

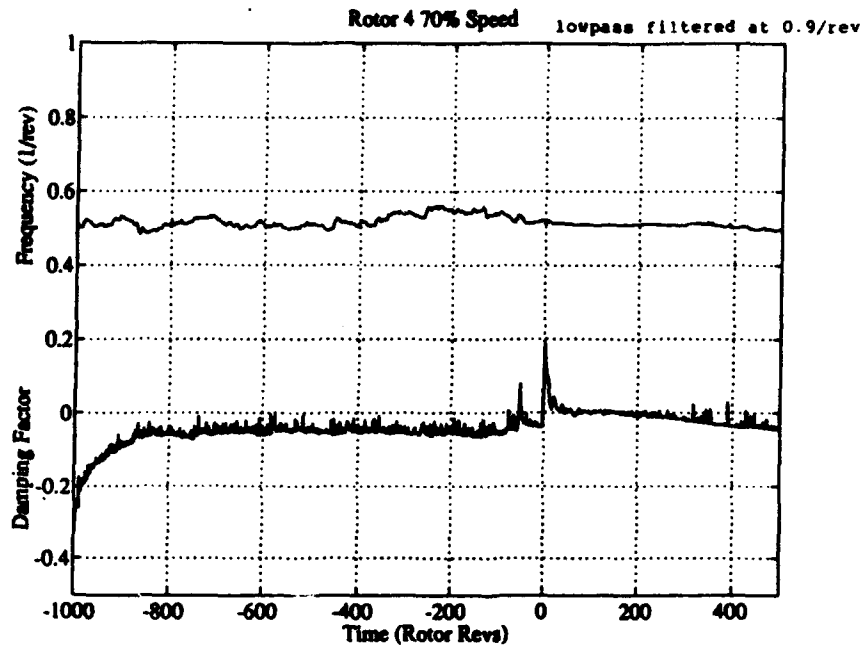


Figure 4.3 Frequency and Damping Factor - Mode 1
Rotor 4 70% Speed - Lowpass filtered at 0.9/rev

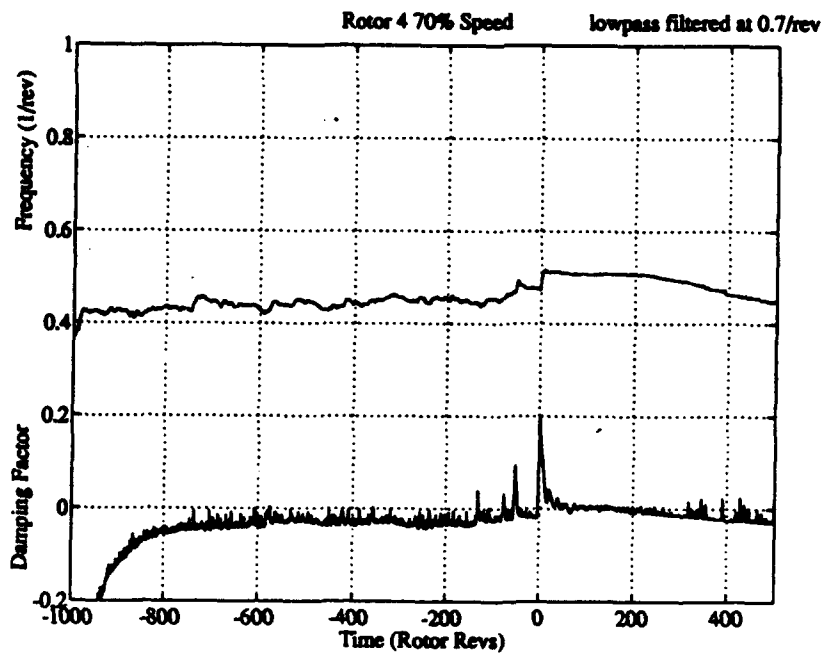


Figure 4.4 Frequency and Damping Factor - Mode 1
Rotor 4 70% Speed - Lowpass filtered at 0.7/rev

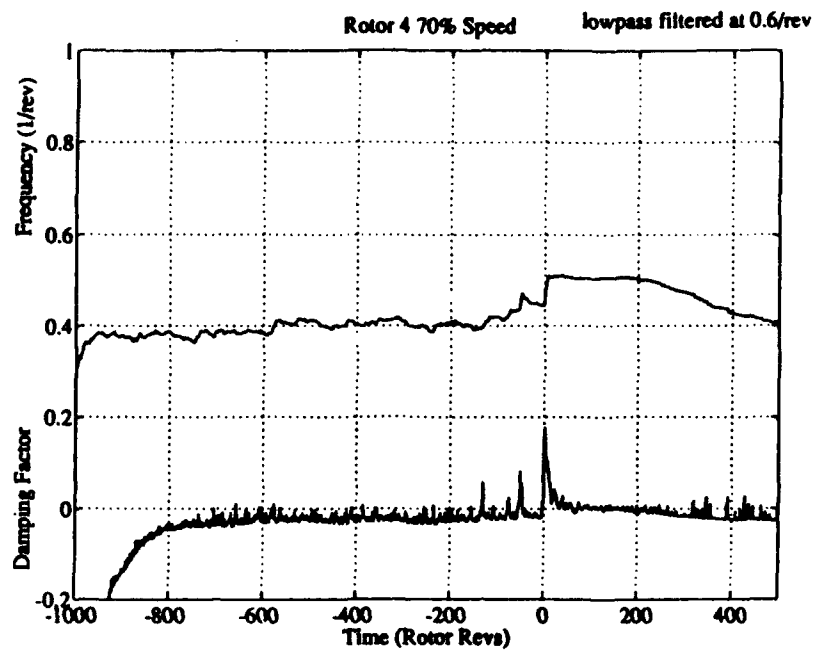


Figure 4.5 Frequency and Damping Factor - Mode 1
Rotor 4 70% Speed - Lowpass filtered at 0.6/rev

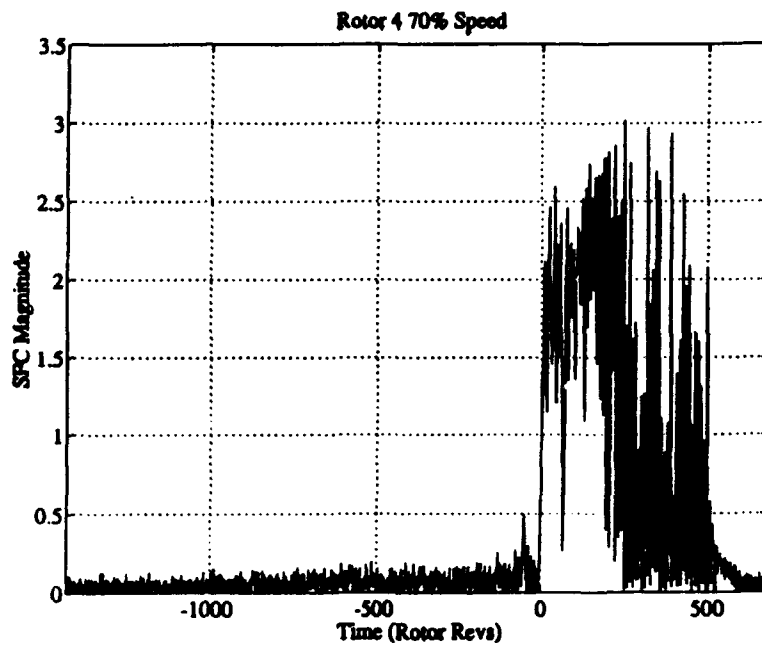


Figure 4.6 Spatial Fourier Magnitude versus Time plot
Rotor 4 70% Speed

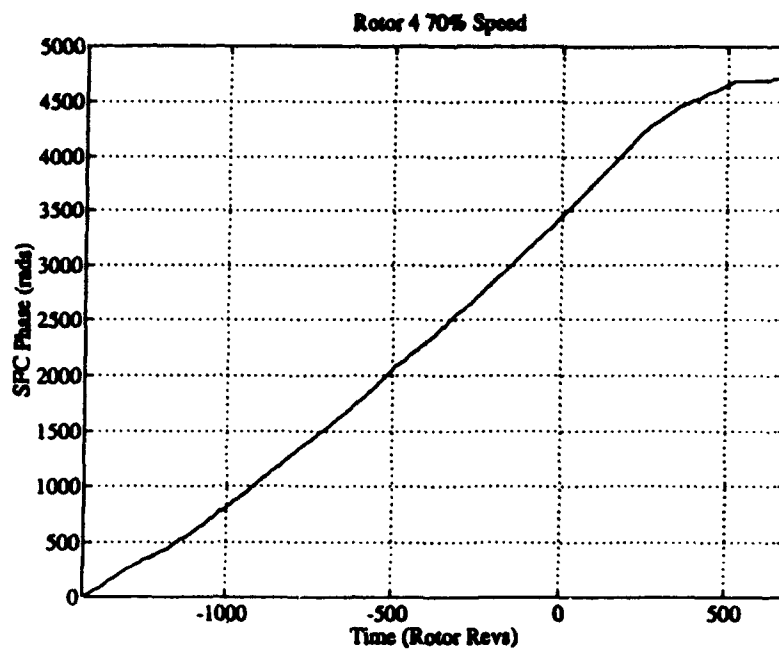


Figure 4.7 Spatial Fourier Phase versus Time plot
Rotor 4 70% Speed

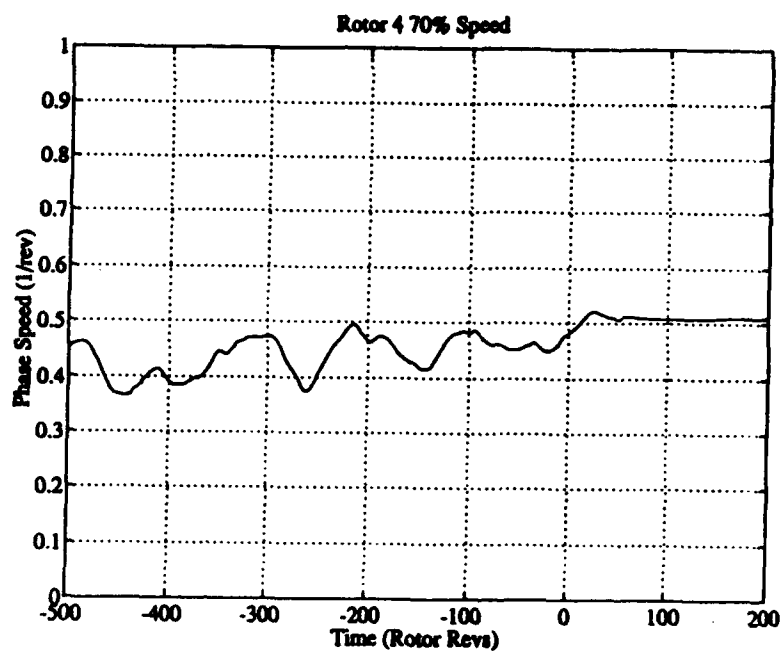


Figure 4.8 Phase Tracking Output - Rotor 4 70% Speed

Rotor 4 70% Speed

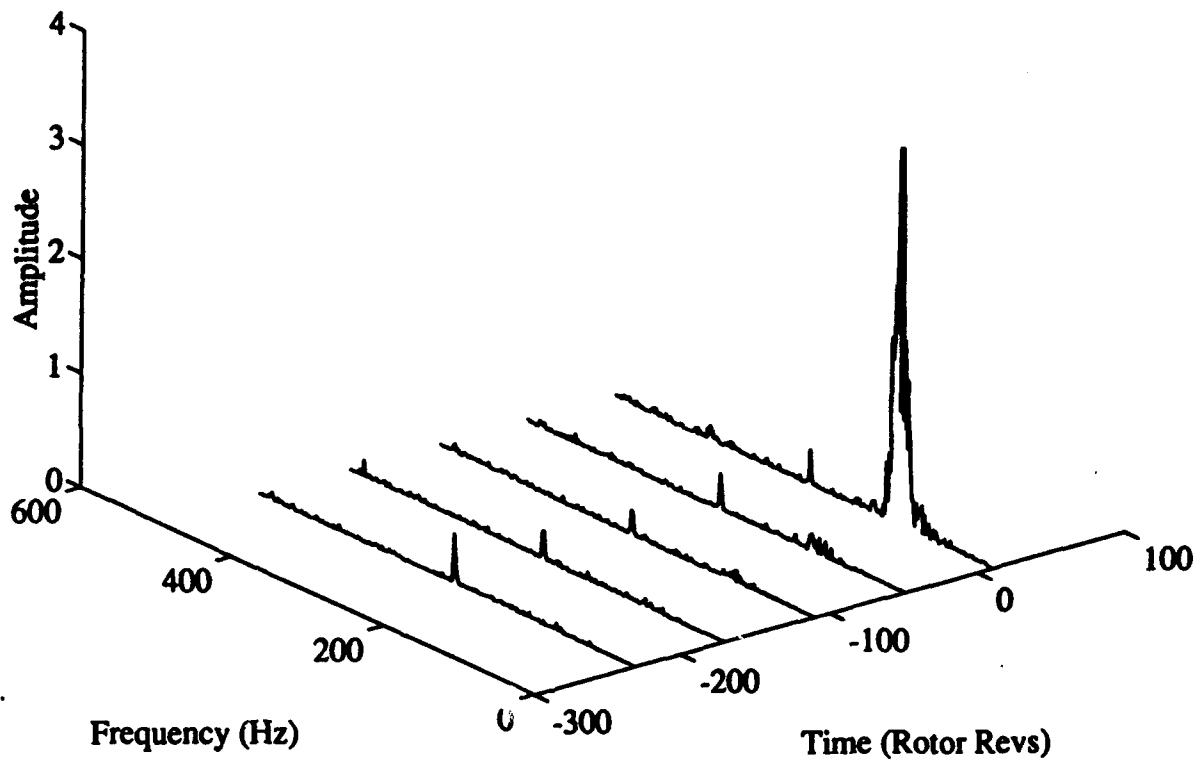
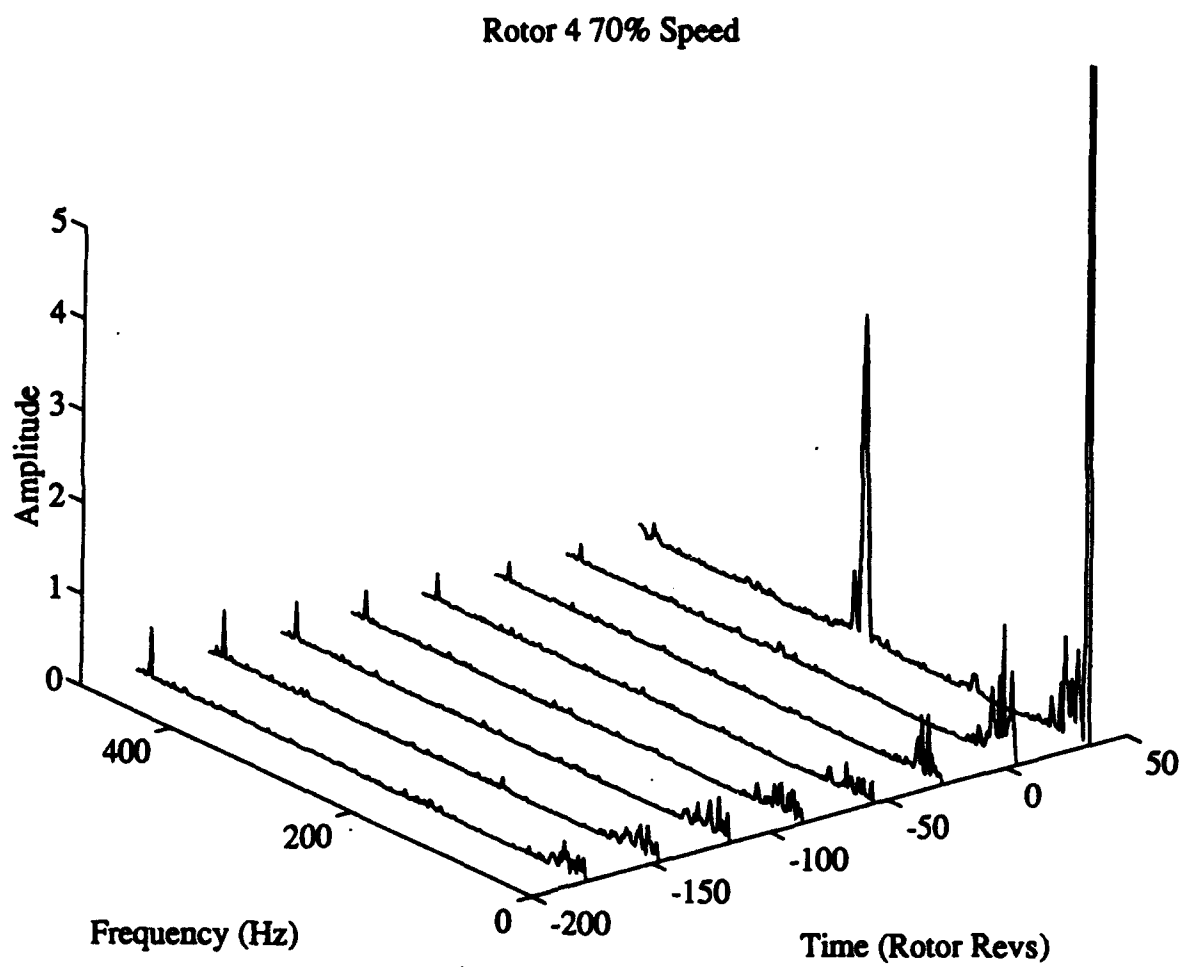
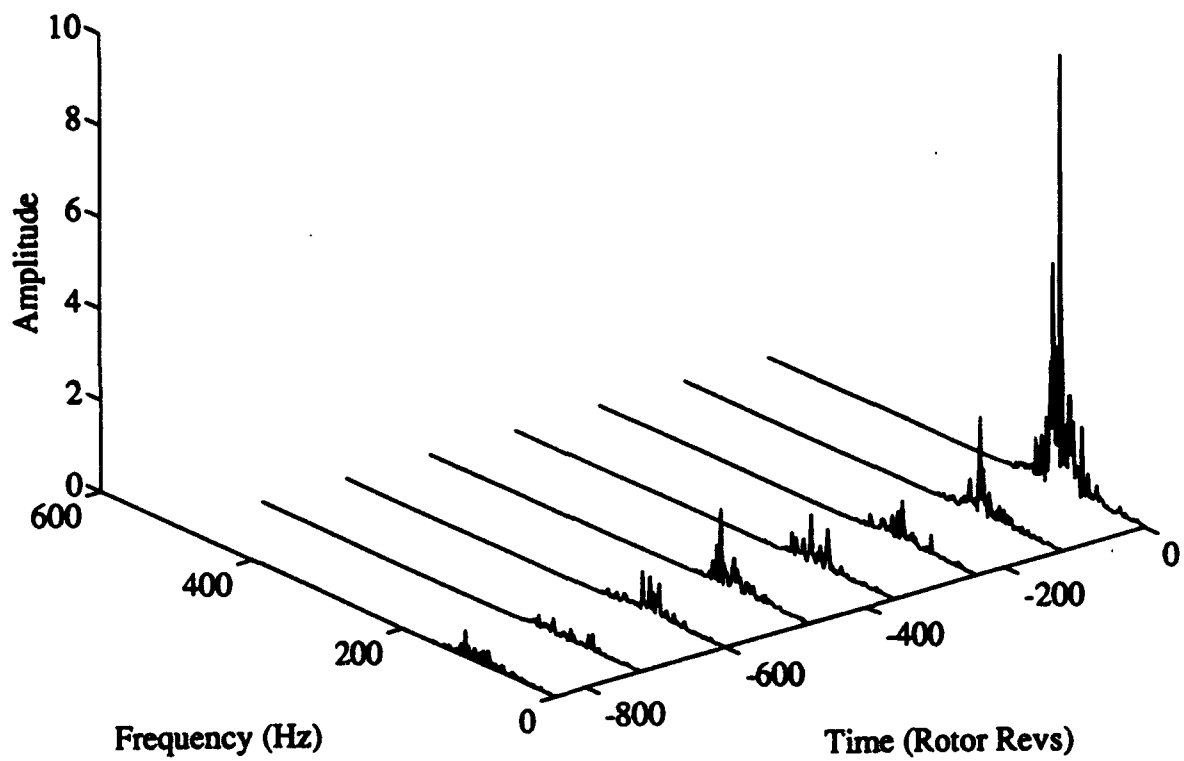


Figure 4.9 Windowed Frequency Pressure Signal Data
(180 Degree Subtracted) - Rotor 4 70% Speed



**Figure 4.10 Windowed Frequency Pressure Signal
(180 Degree Addition) - Rotor 4 70% Speed**

Rotor 4 70% Speed



**Figure 4.11 Windowed Frequency Spectrum from SFCs
Rotor 4 70% Speed**

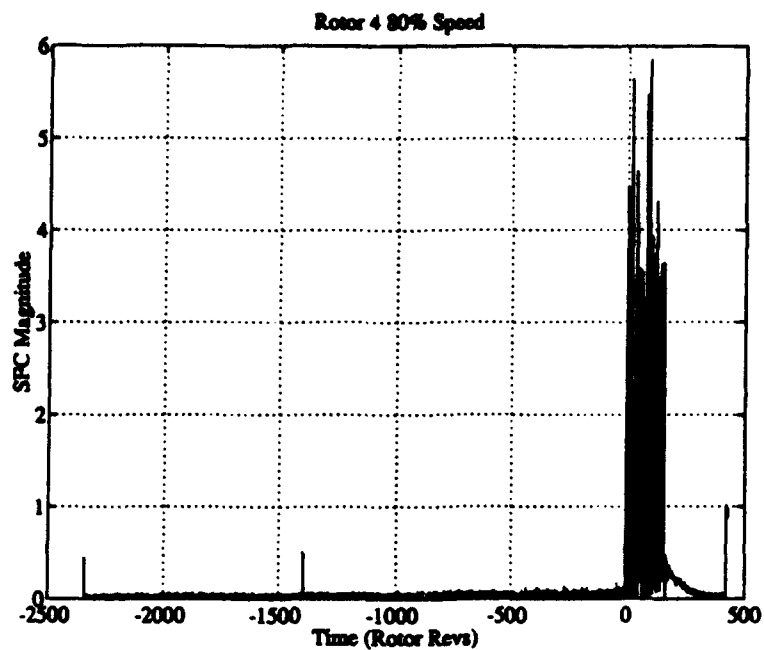


Figure 4.12 Spatial Fourier Magnitude versus Time plot
Rotor 4 80% Speed

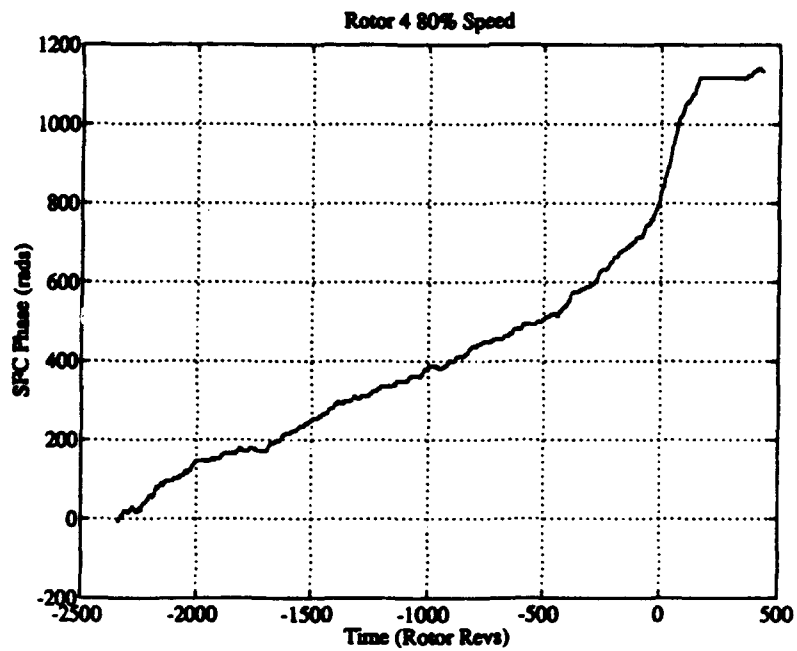
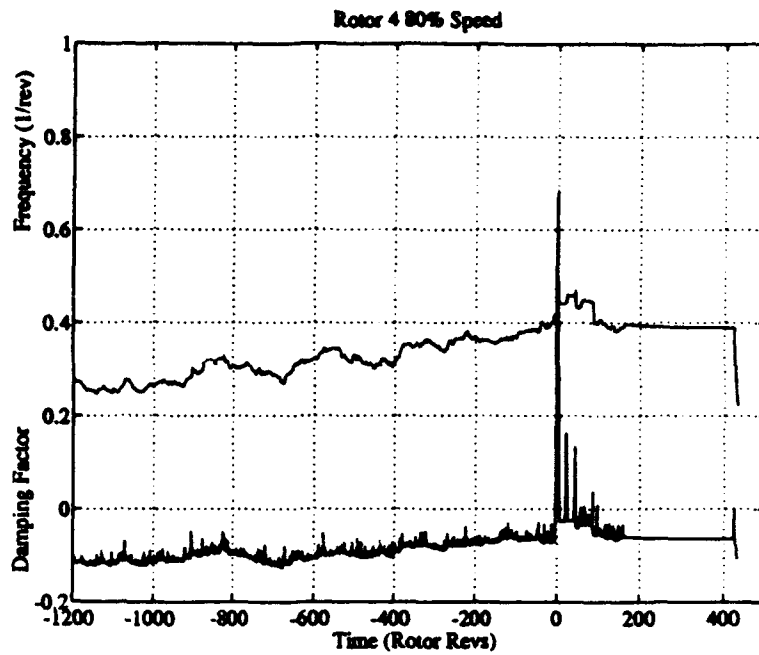
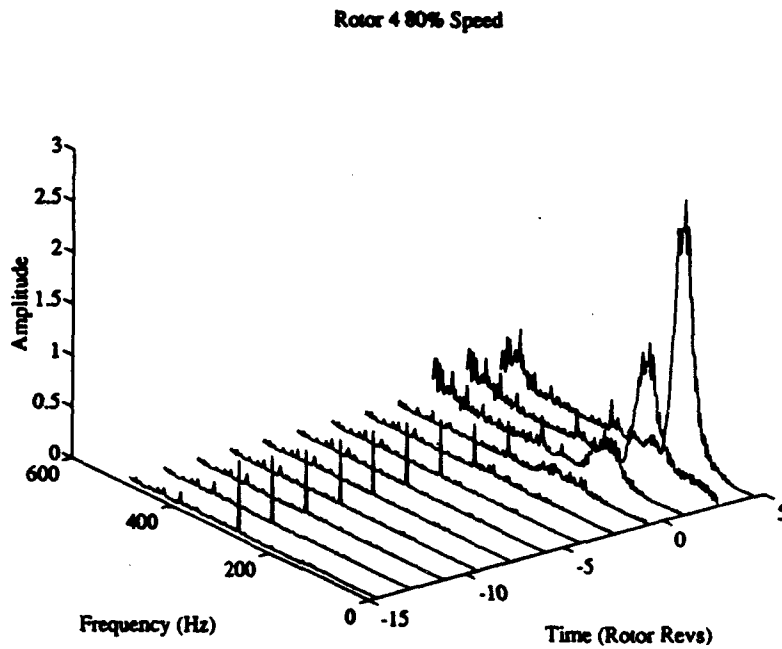


Figure 4.13 Spatial Fourier Phase versus Time plot
Rotor 4 80% Speed



**Figure 4.14 Frequency and Damping Factor
Rotor 4 80% Speed**



**Figure 4.15 Windowed Frequency Pressure Signal Data
Rotor 4 80% Speed**

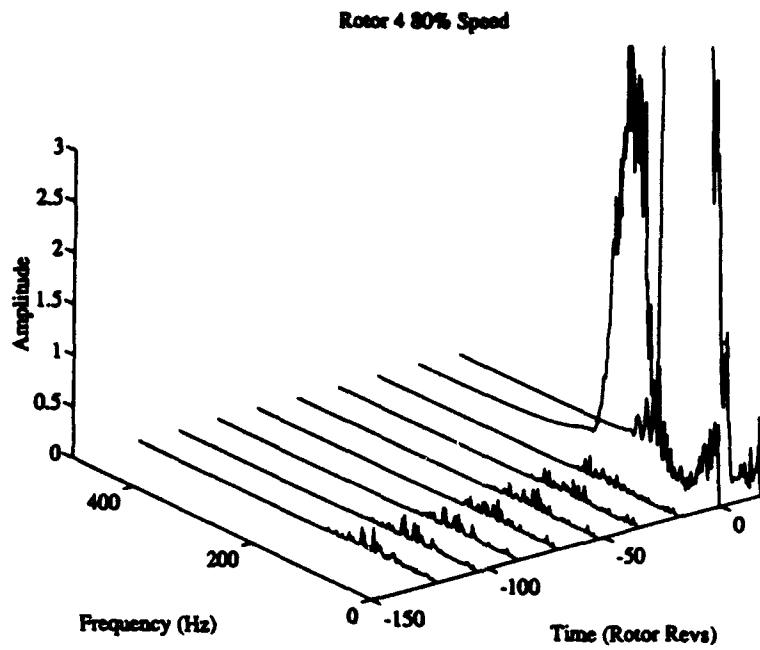


**Figure 4.16 Windowed Frequency Spectrum from SFCs
Rotor 4 80% Speed**

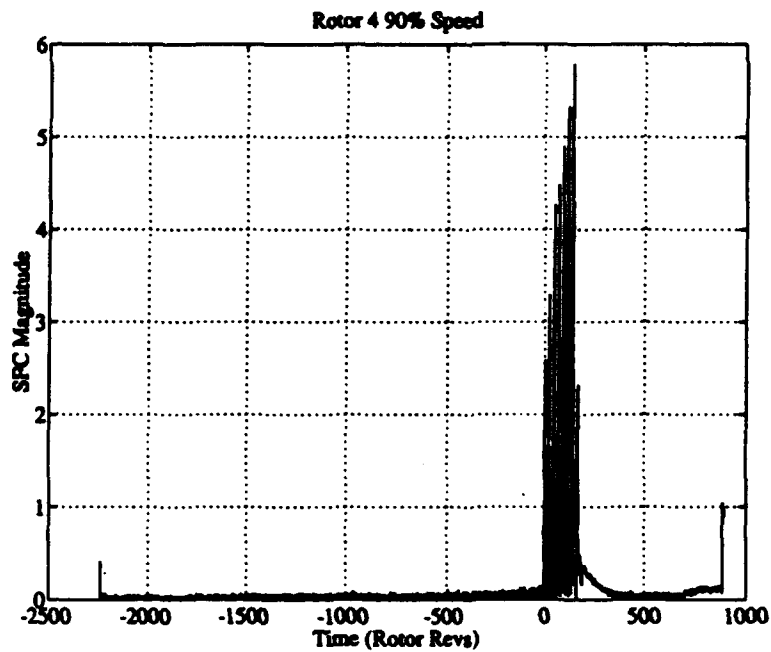


**Figure 4.17 Spatial Fourier Magnitude versus Time plot
Rotor 4 90% Speed**

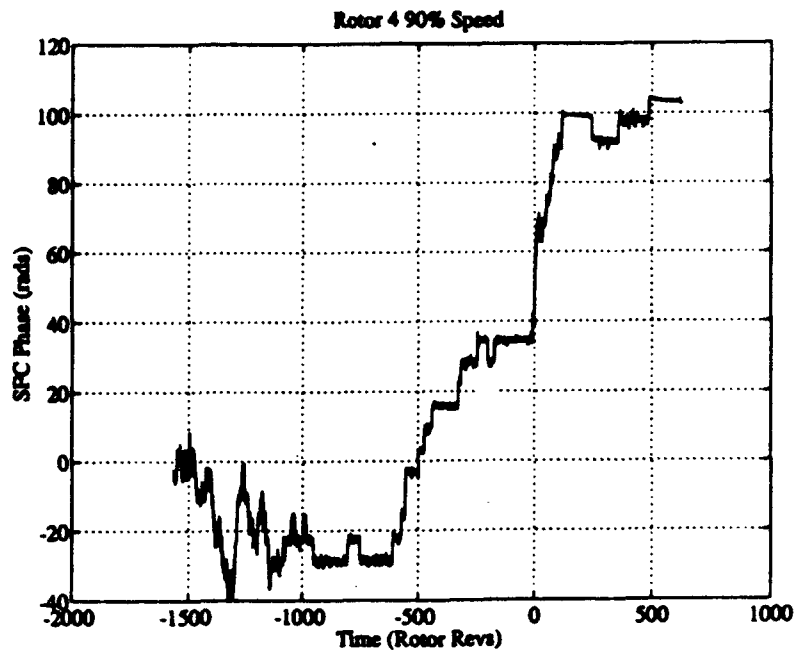


**Figure 4.18 Spatial Fourier Phase versus Time plot
Rotor 4 90% Speed**

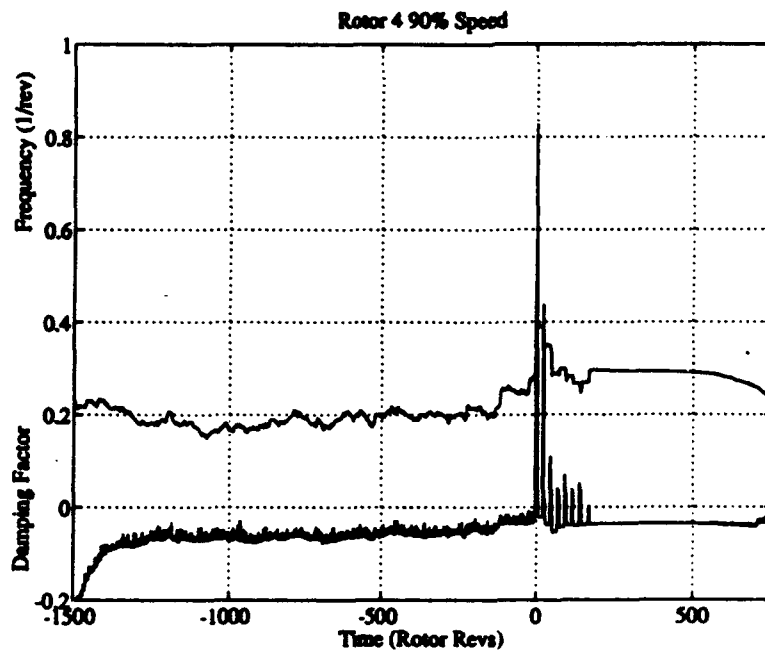


**Figure 4.19 Frequency and Damping Factor
Rotor 4 90% Speed**

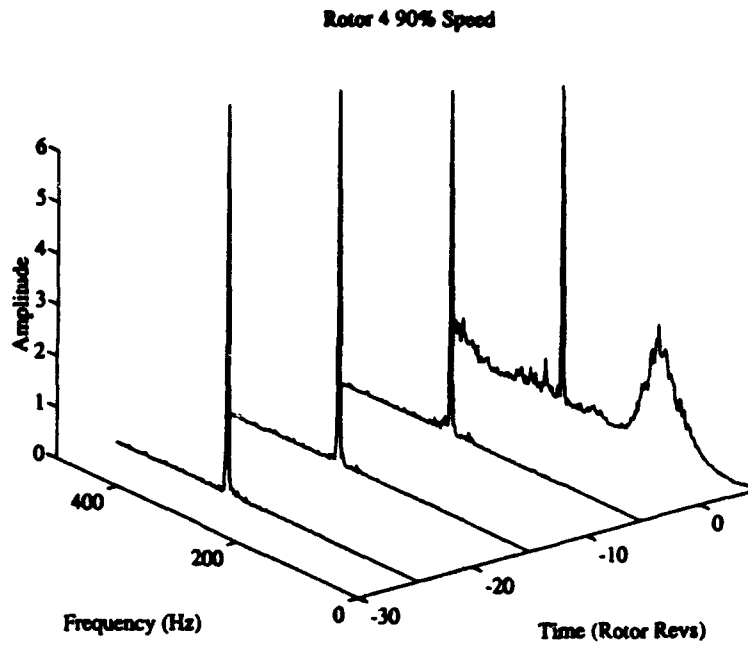


**Figure 4.20 Windowed Frequency Pressure Signal
Rotor 4 90% Speed**

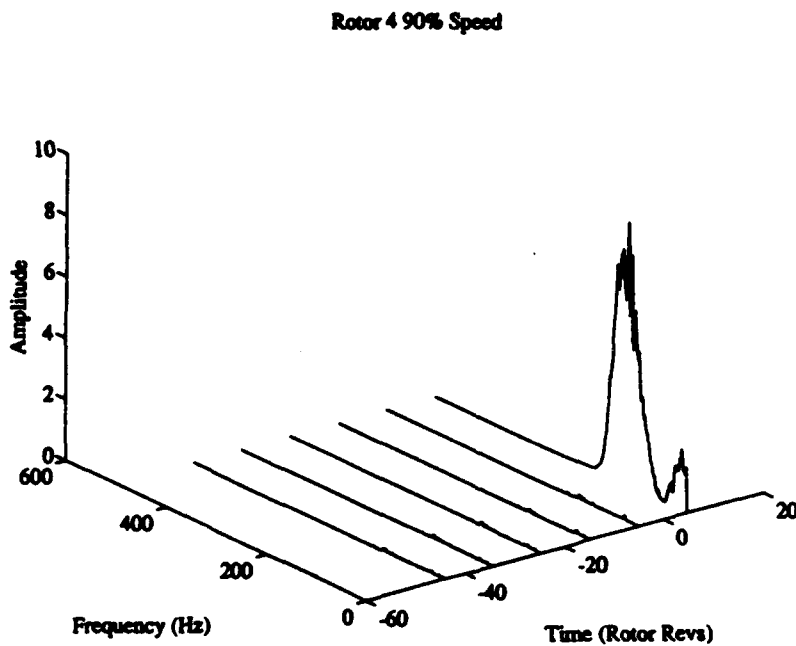


**Figure 4.21 Windowed Frequency Spectrum from SFCs
Rotor 4 90% Speed**

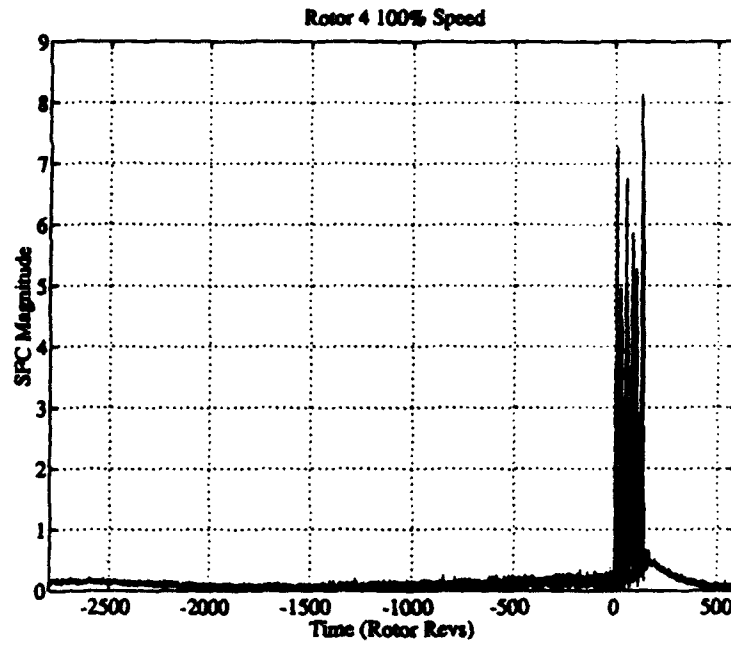


Figure 4.22 Spatial Fourier Magnitude versus Time plot
Rotor 4 100% Speed

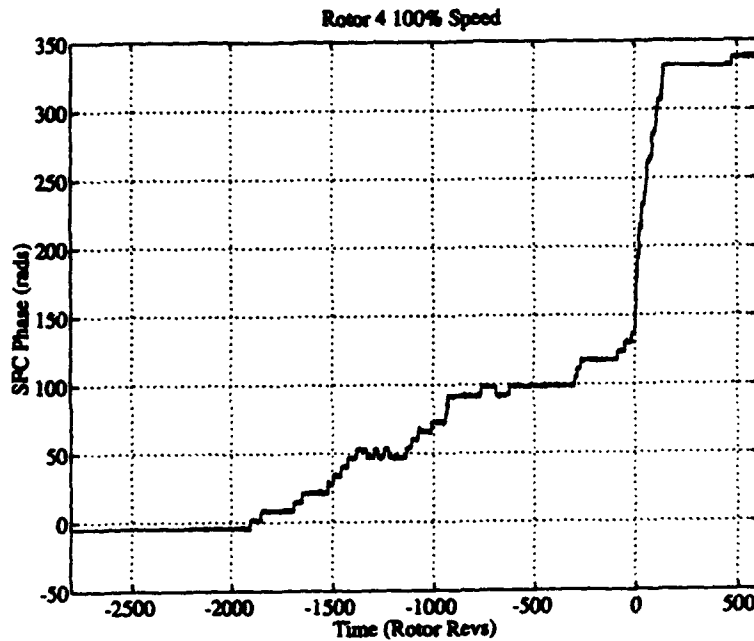
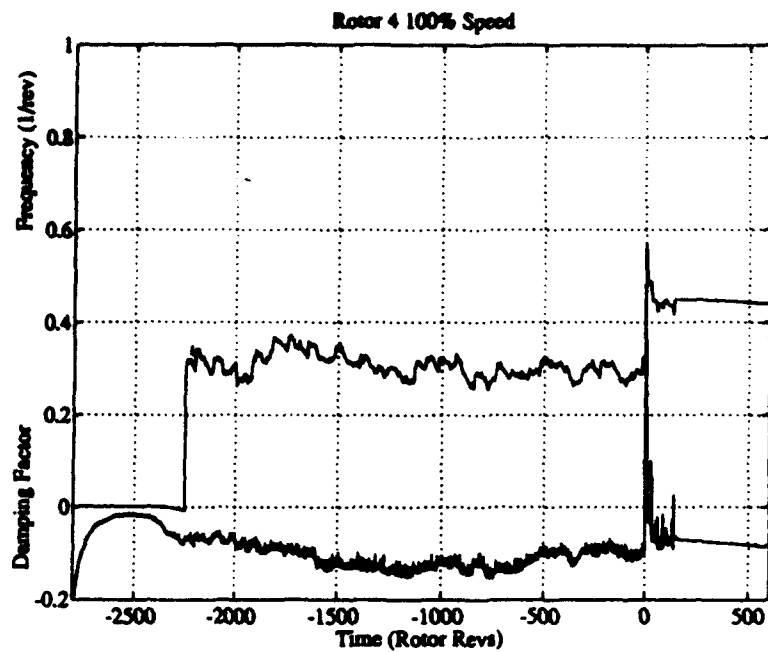
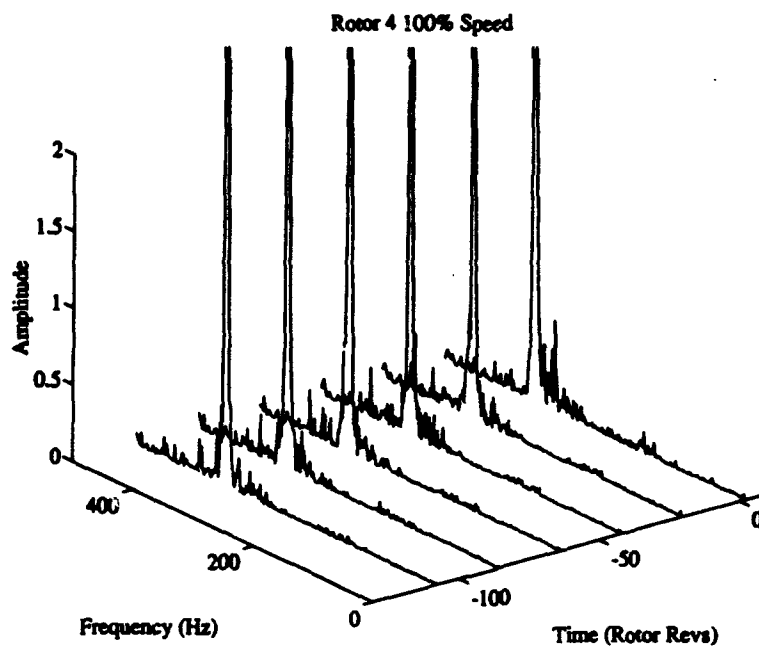


Figure 4.23 Spatial Fourier Phase versus Time plot
Rotor 4 100% Speed



**Figure 4.24 Frequency and Damping Factor
Rotor 4 100% Speed**



**Figure 4.25 Windowed Frequency Pressure Signal Data
Rotor 4 100% Speed**

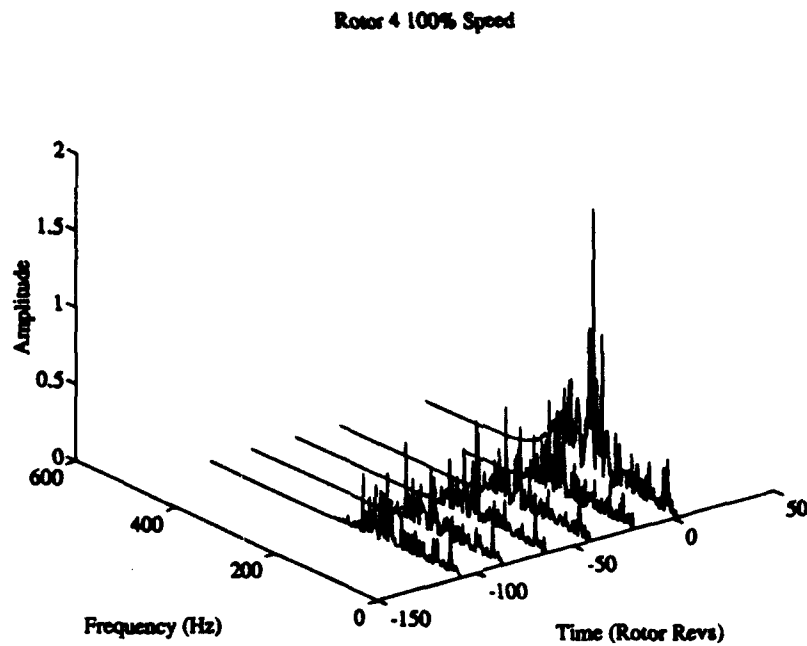


**Figure 4.26 Windowed Frequency Spectrum from SFCs
Rotor 4 100% Speed**

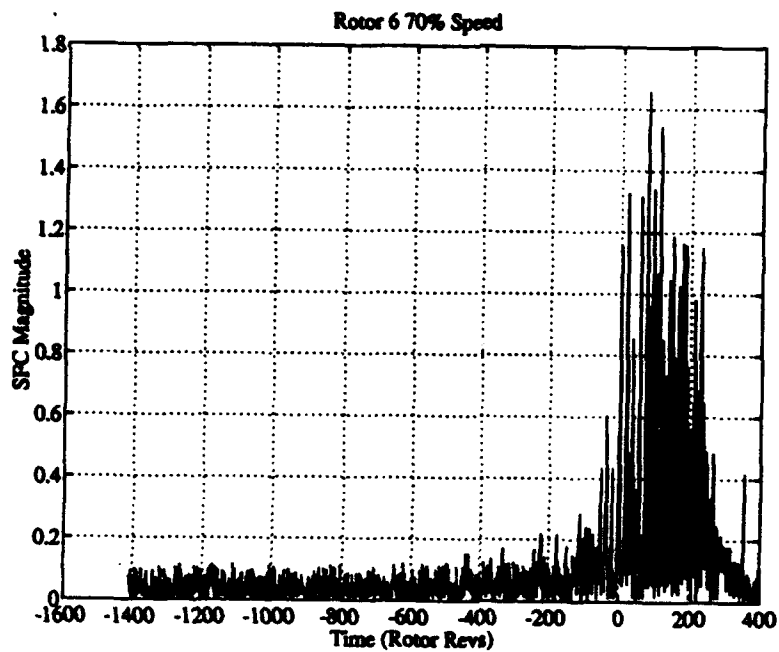


**Figure 4.27 Spatial Fourier Magnitude versus Time plot
Rotor 6 70% Speed**

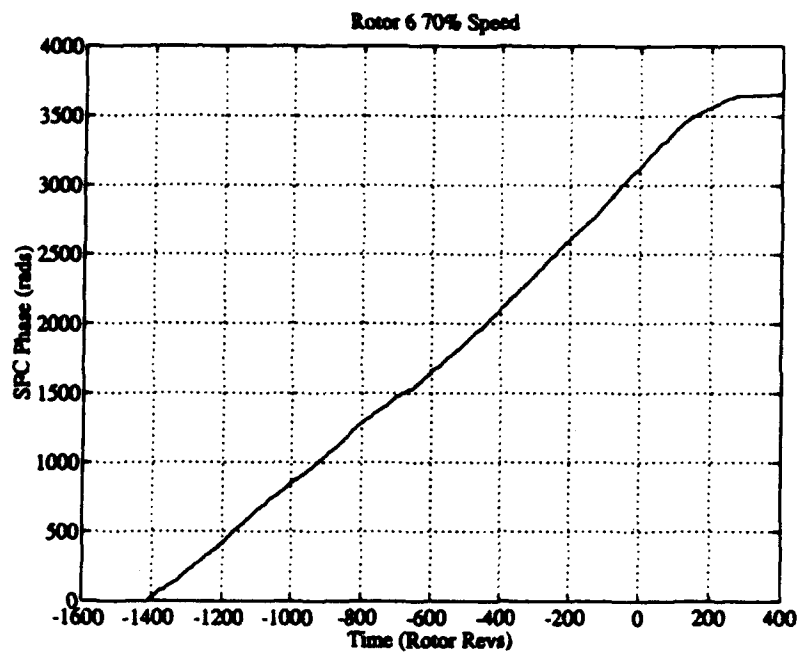


Figure 4.28 Spatial Fourier Phase versus Time plot
Rotor 6 70% Speed

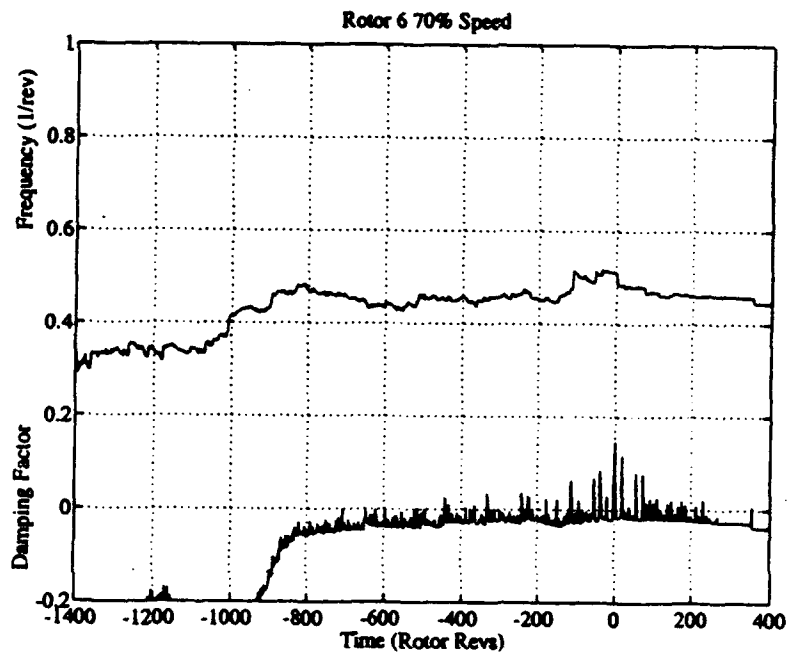
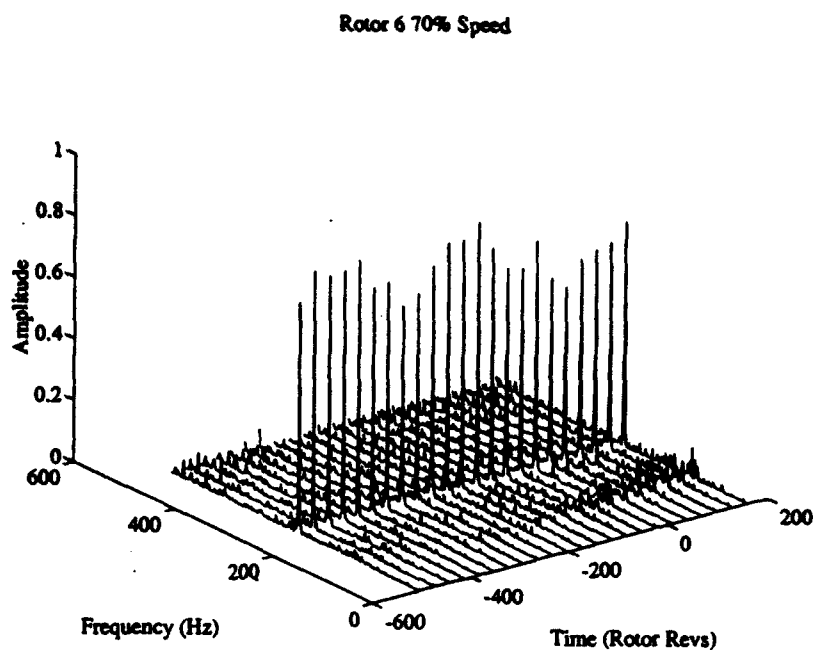
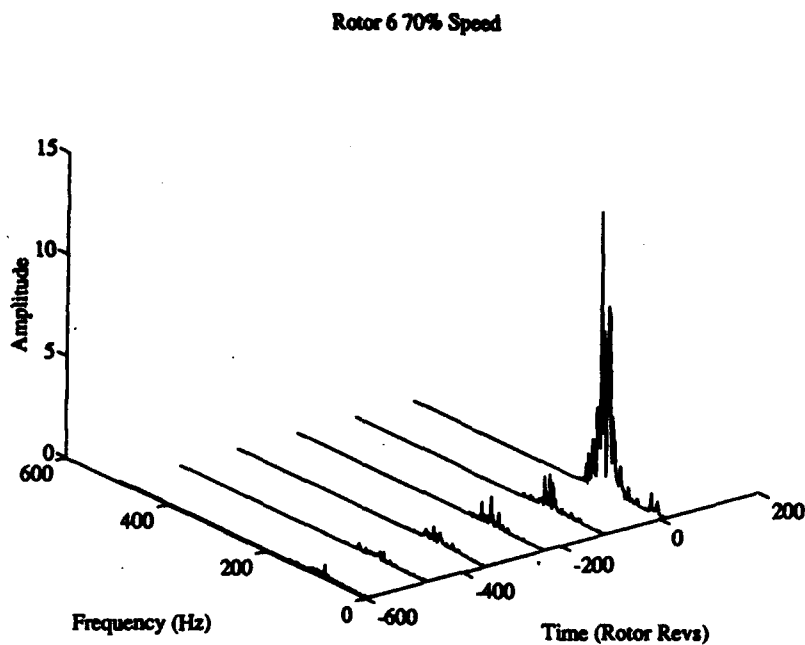


Figure 4.29 Frequency and Damping Factor
Rotor 6 70% Speed



**Figure 4.30 Windowed Frequency Pressure Signal Data
Rotor 6 70% Speed**



**Figure 4.31 Windowed Frequency Spectrum from SFCs
Rotor 6 70% Speed**

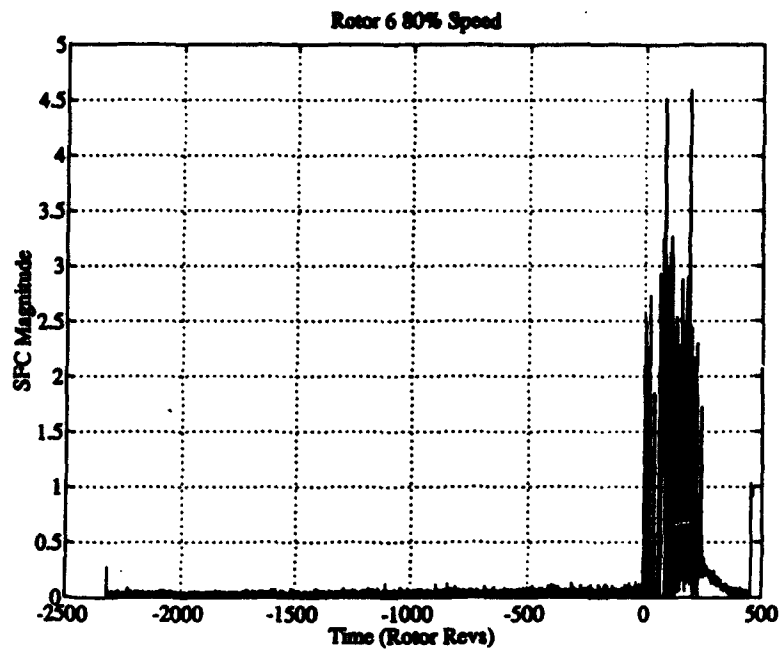


**Figure 4.32 Spatial Fourier Magnitude versus Time plot
Rotor 6 80% Speed**

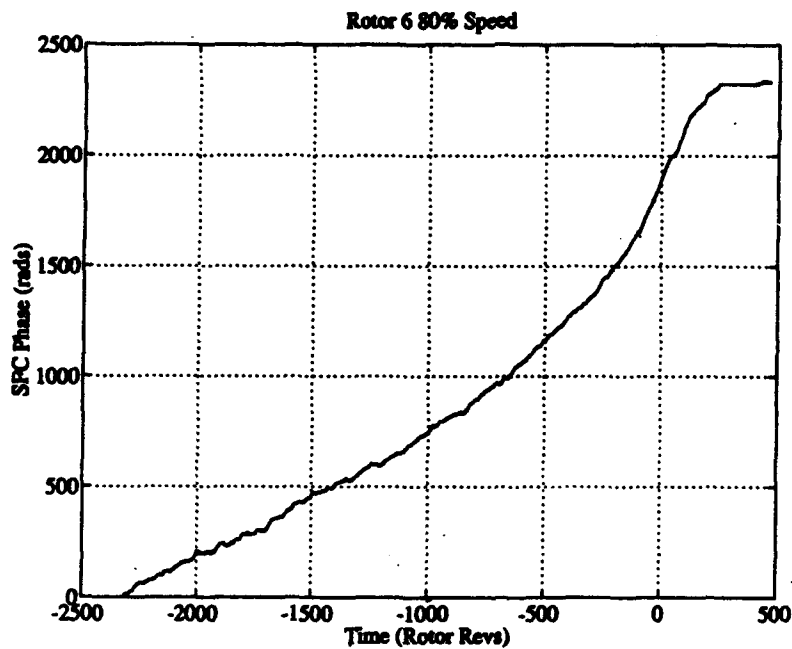


**Figure 4.33 Spatial Fourier Phase versus Time plot
Rotor 6 80% Speed**

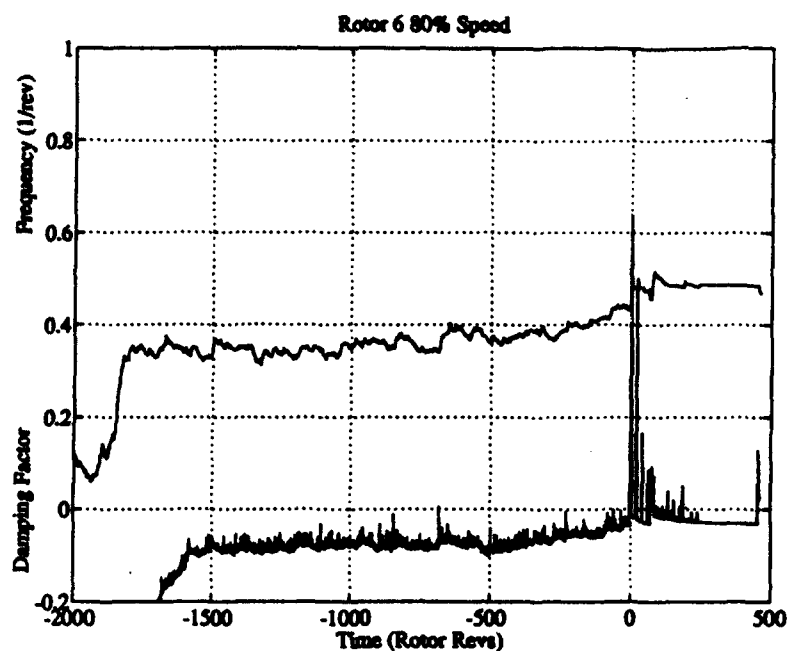


Figure 4.34 Frequency and Damping Factor
Rotor 6 80% Speed

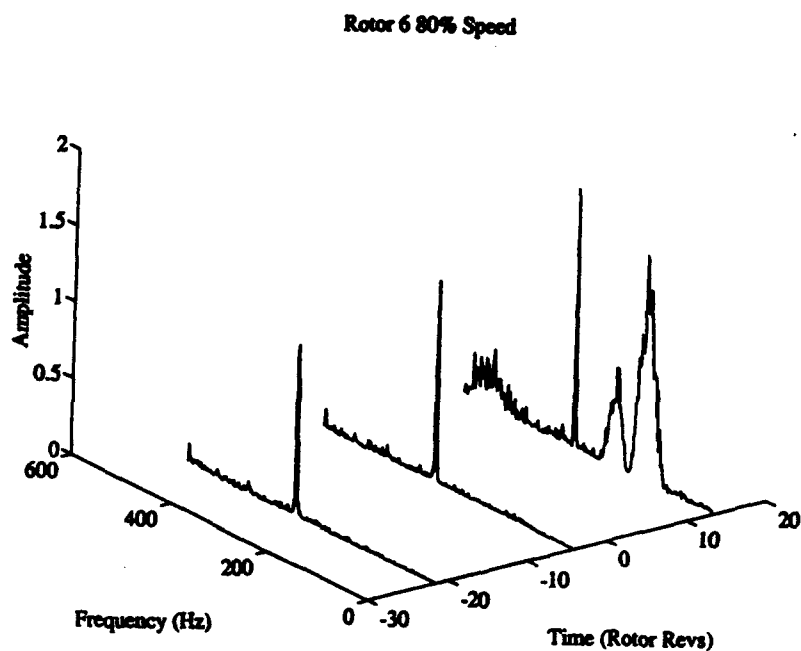
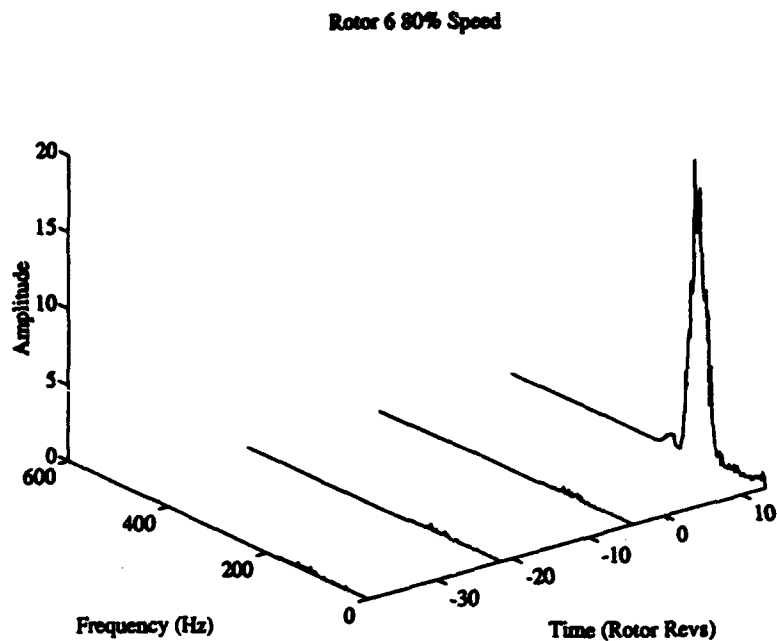
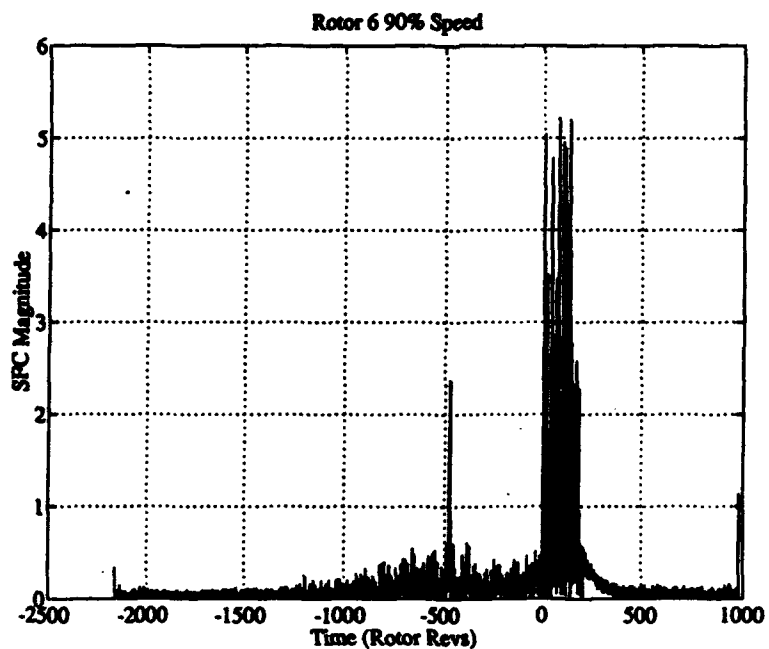


Figure 4.35 Windowed Frequency Pressure Signal Data
Rotor 6 80% Speed



**Figure 4.36 Windowed Frequency Spectrum from SFCs
Rotor 6 80% Speed**



**Figure 4.37 Spatial Fourier Magnitude versus Time plot
Rotor 6 90% Speed**

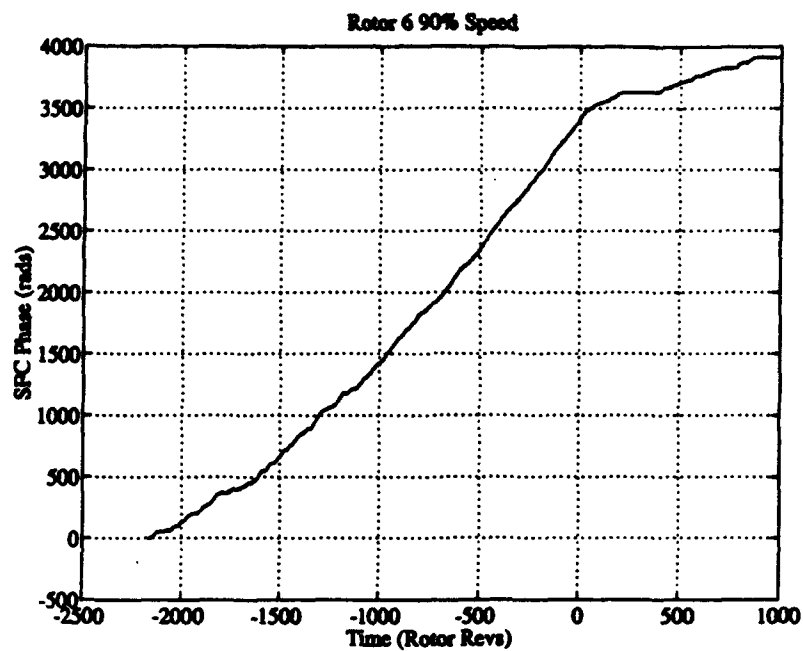


Figure 4.38 Spatial Fourier Phase versus Time plot
Rotor 6 90% Speed

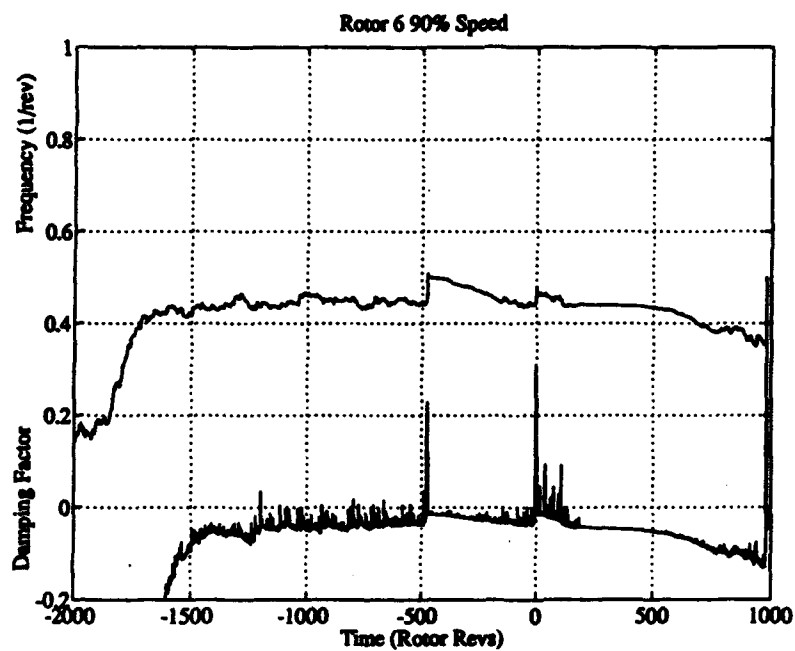
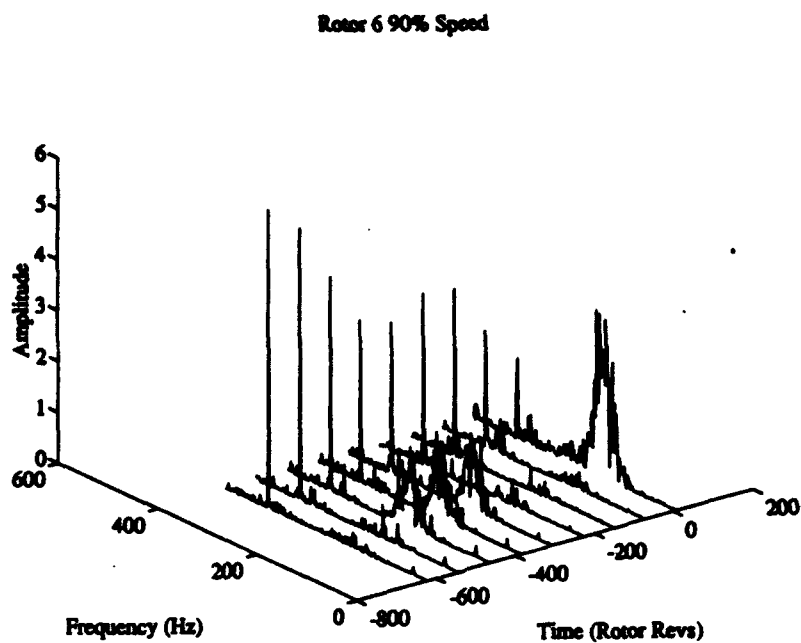
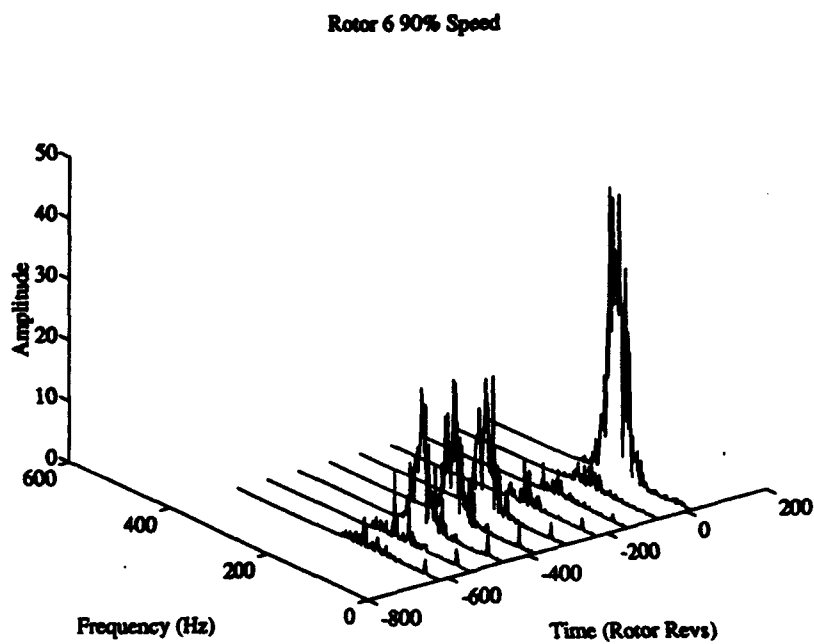


Figure 4.39 Frequency and Damping Factor
Rotor 6 90% Speed



**Figure 4.40 Windowed Frequency Pressure Signal Data
Rotor 6 90% Speed**



**Figure 4.41 Windowed Frequency Spectrum from SFCs
Rotor 6 90% Speed**

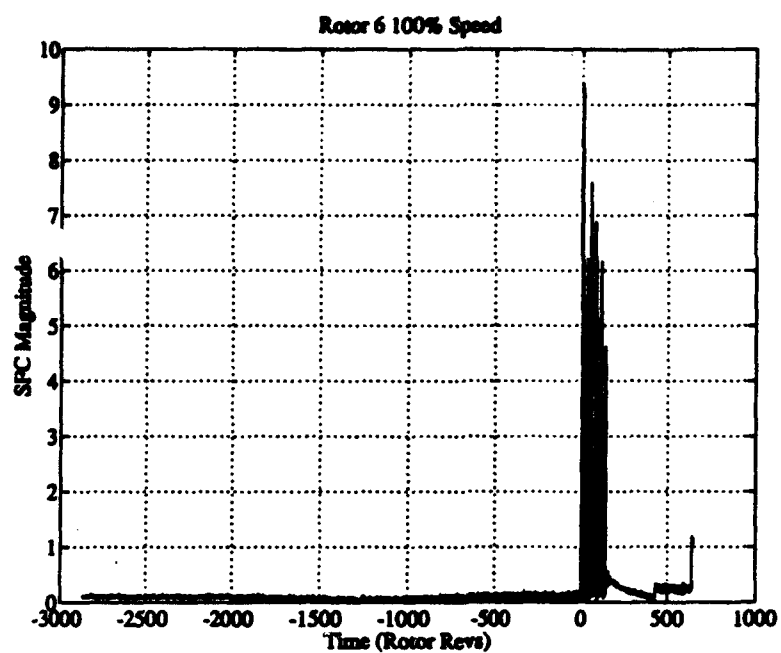


Figure 4.42 Spatial Fourier Magnitude versus Time plot
Rotor 6 100% Speed

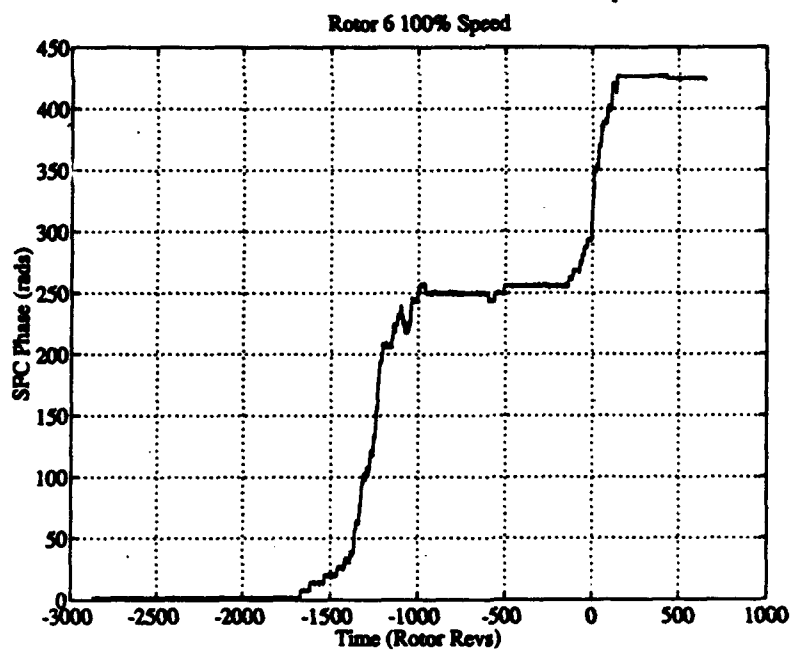
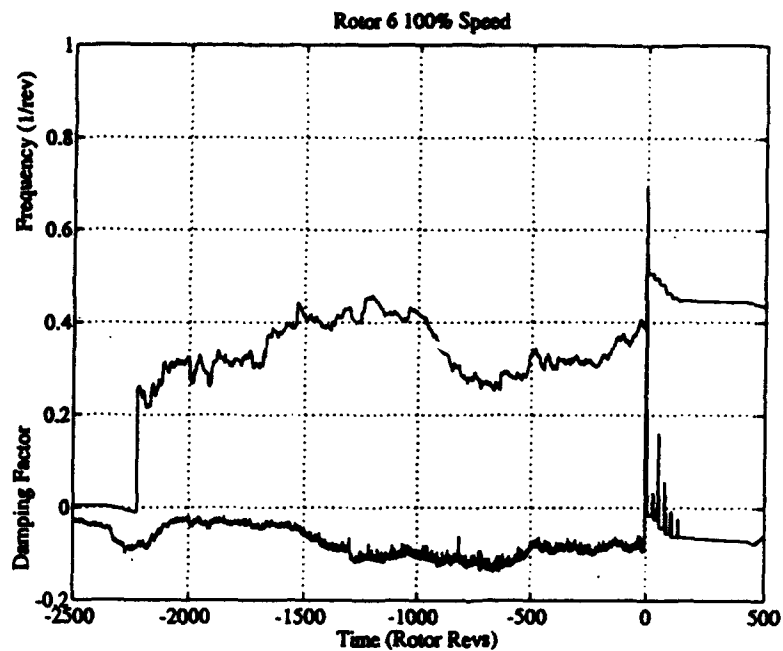
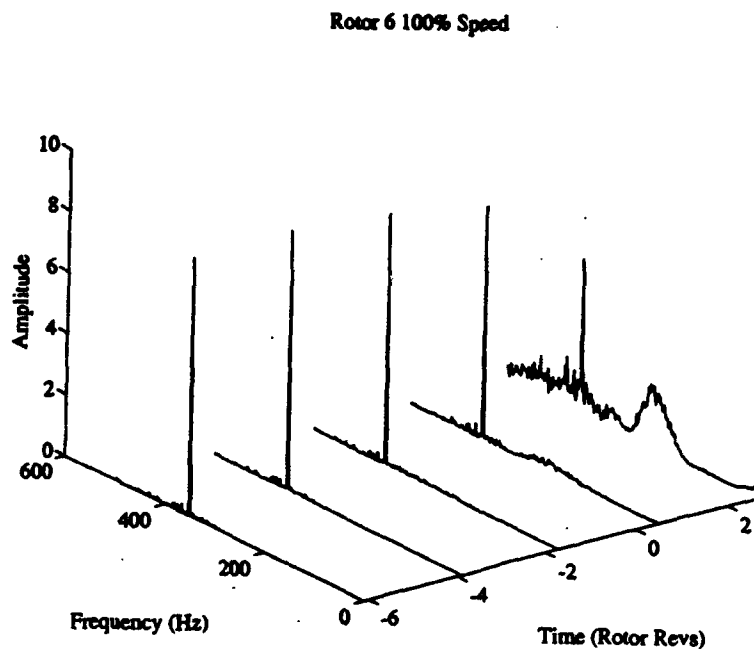


Figure 4.43 Spatial Fourier Phase versus Time plot
Rotor 6 100% Speed



**Figure 4.44 Frequency versus Damping Factor
Rotor 6 100% Speed**



**Figure 4.45 Windowed Frequency Pressure Signal Data
Rotor 6 100% Speed**

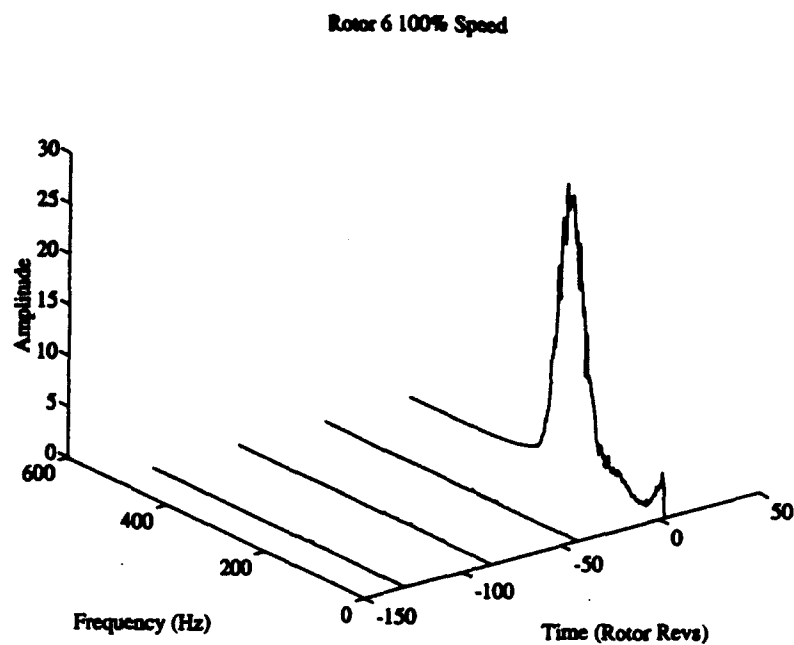


**Figure 4.46 Windowed Frequency Spectrum from SFCs
Rotor 6 100% Speed**

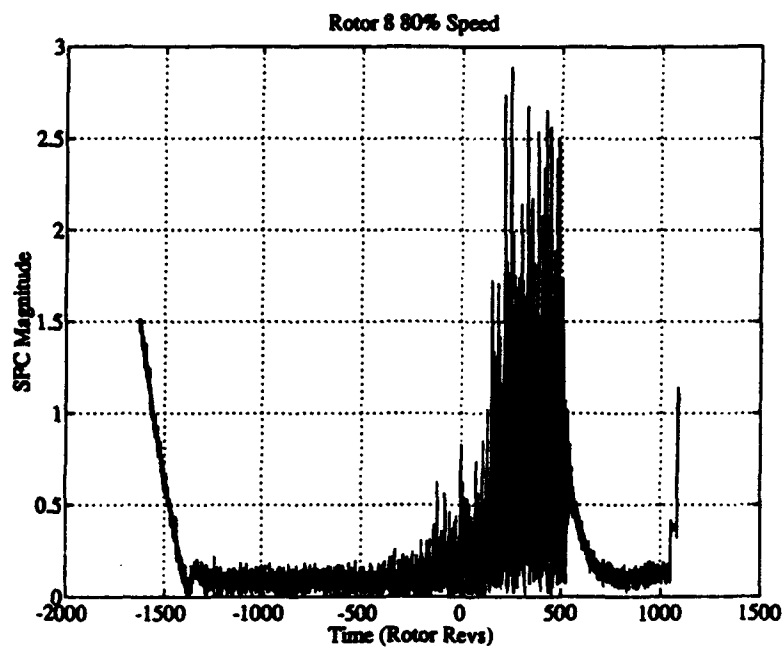


**Figure 4.47 Spatial Fourier Magnitude versus Time plot
Rotor 8 80% Speed**

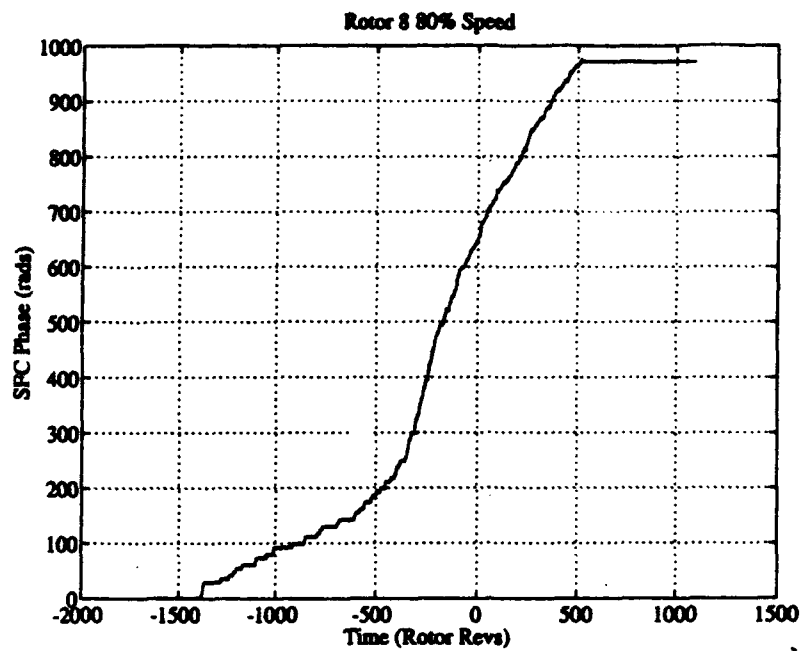


Figure 4.48 Spatial Fourier Phase versus Time plot
Rotor 8 80% Speed

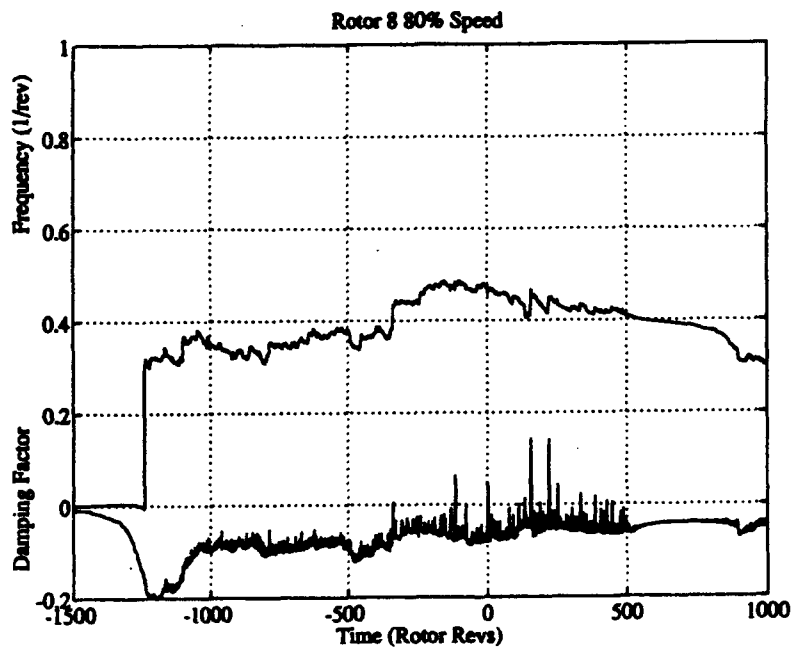
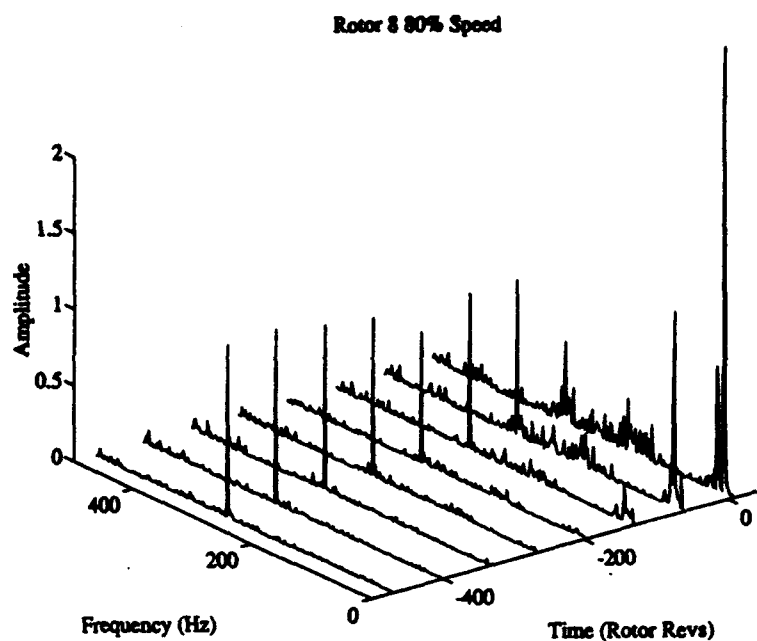
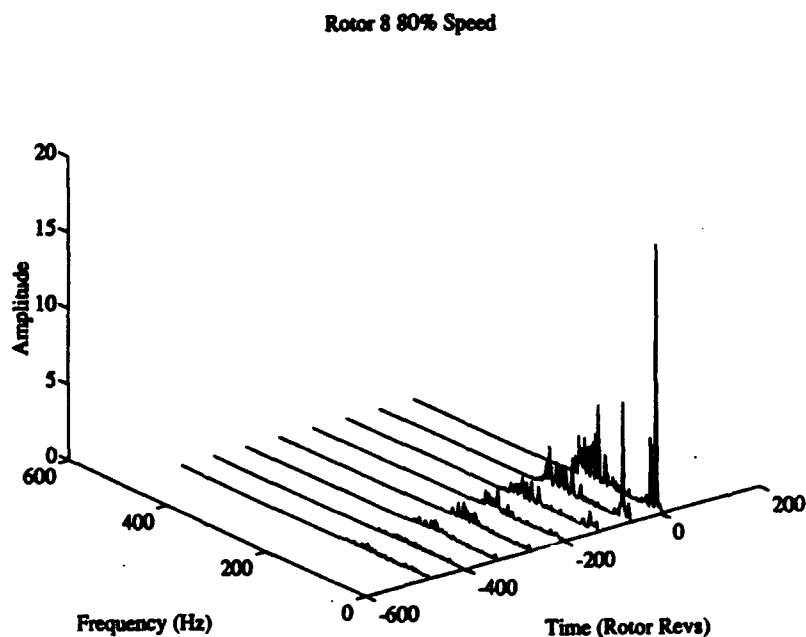


Figure 4.49 Frequency and Damping Factor
Rotor 8 80% Speed



**Figure 4.50 Windowed Frequency Pressure Signal Data
Rotor 8 80% Speed**



**Figure 4.51 Windowed Frequency Spectrum from SFCs
Rotor 8 80% Speed**

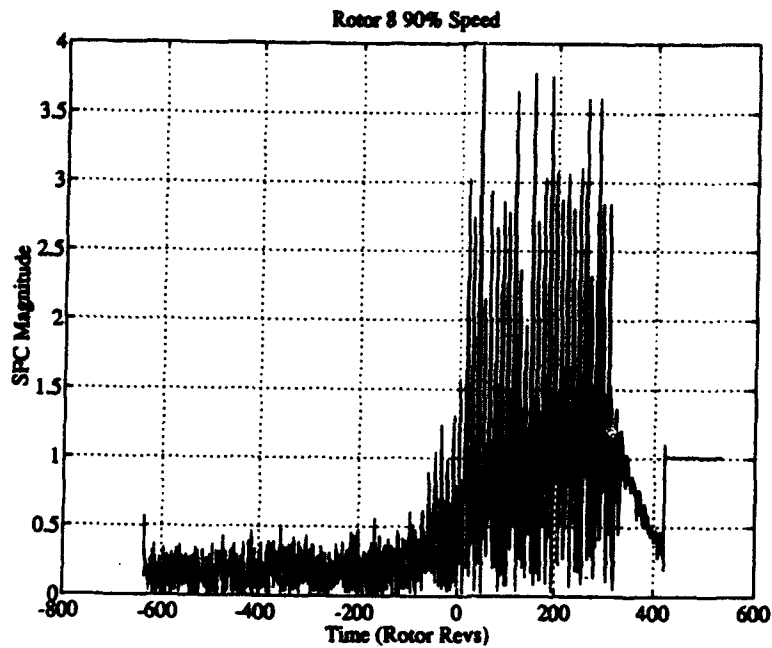


Figure 4.52 Spatial Fourier Magnitude versus Time plot
Rotor 8 90% Speed

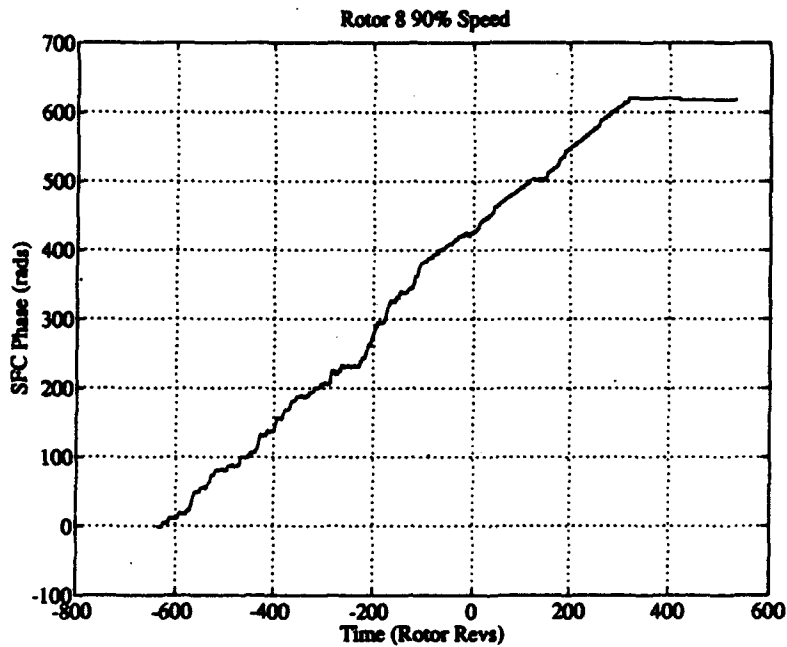
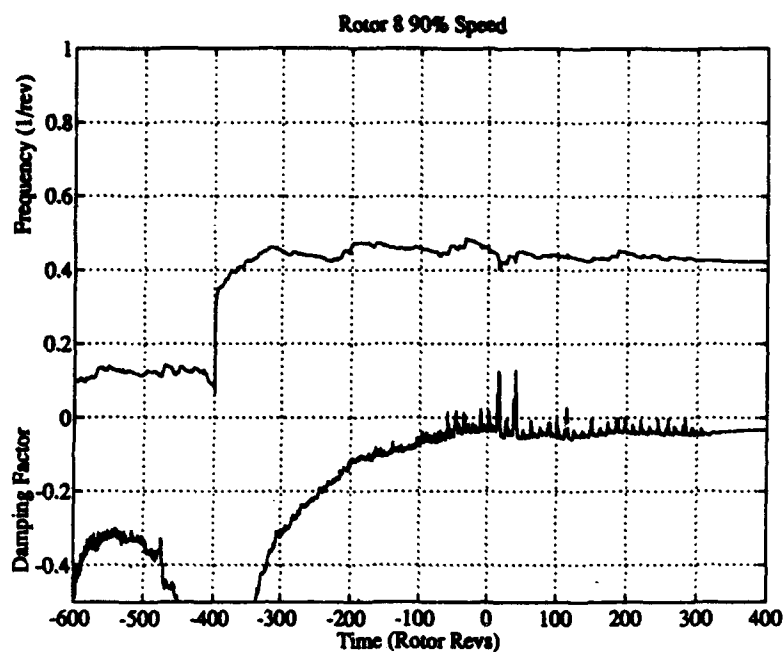
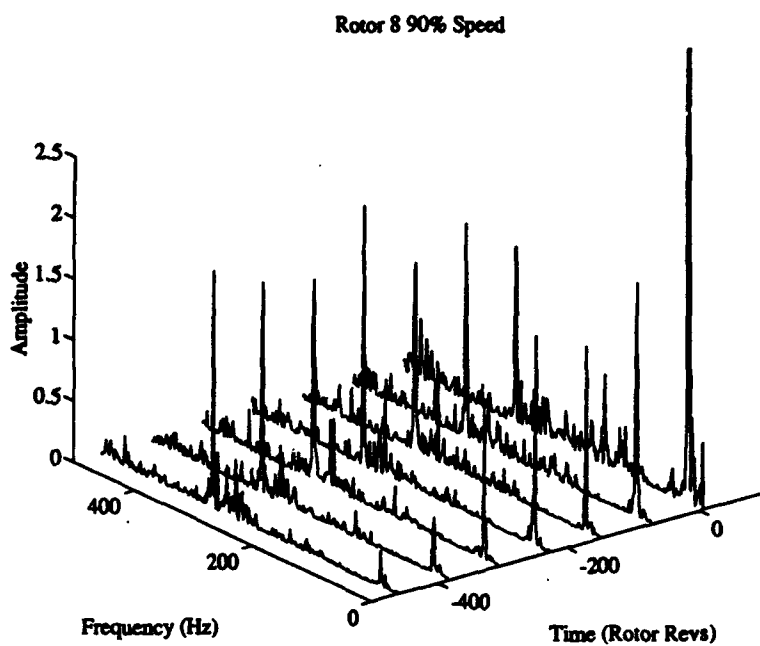


Figure 4.53 Spatial Fourier Phase versus Time plot
Rotor 8 90% Speed



**Figure 4.54 Frequency and Damping Factor
Rotor 8 90% Speed**



**Figure 4.55 Windowed Frequency Pressure Signal Data
Rotor 8 90% Speed**

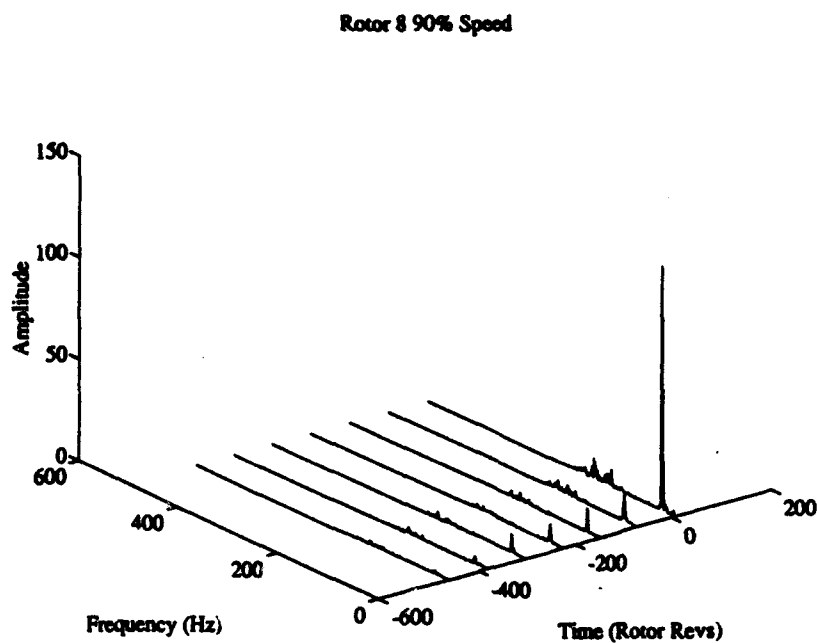


**Figure 4.56 Windowed Frequency Spectrum from SFCs
Rotor 8 90% Speed**

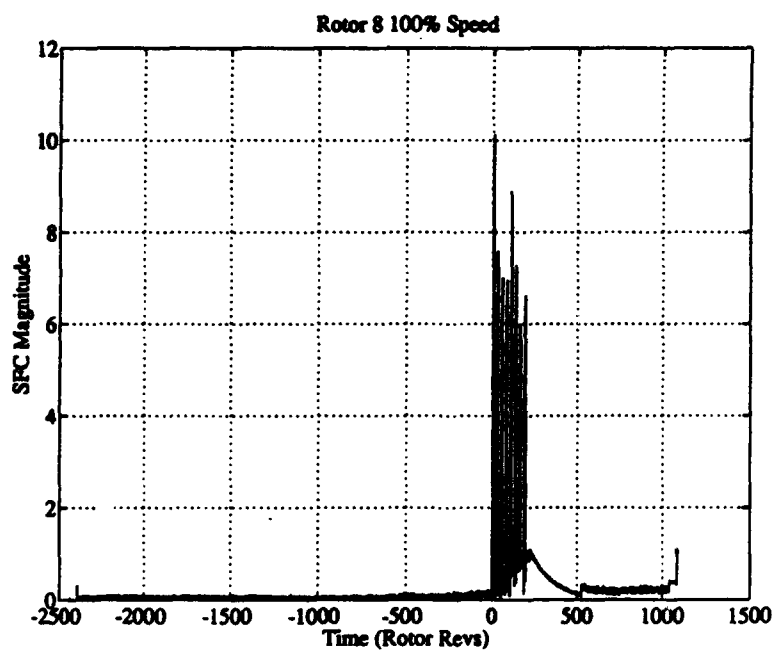


**Figure 4.57 Spatial Fourier Magnitude versus Time plot
Rotor 8 100% Speed**

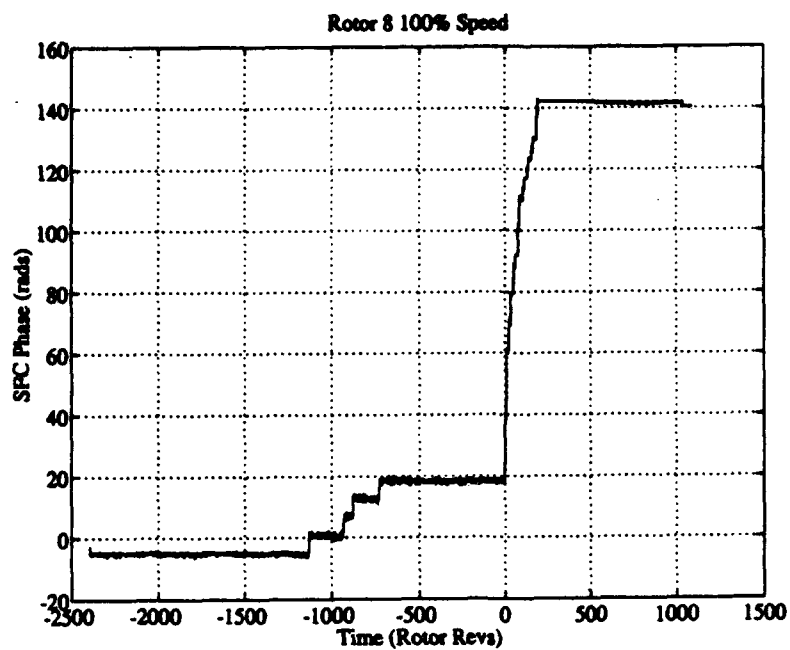


**Figure 4.58 Spatial Fourier Phase versus Time plot
Rotor 8 100% Speed**

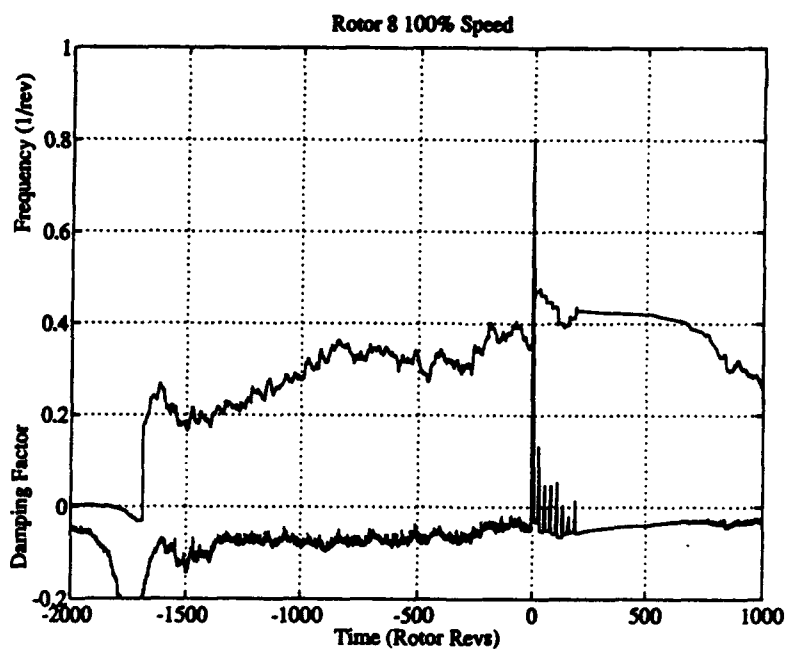


**Figure 4.59 Frequency and Damping Factor
Rotor 8 100% Speed**

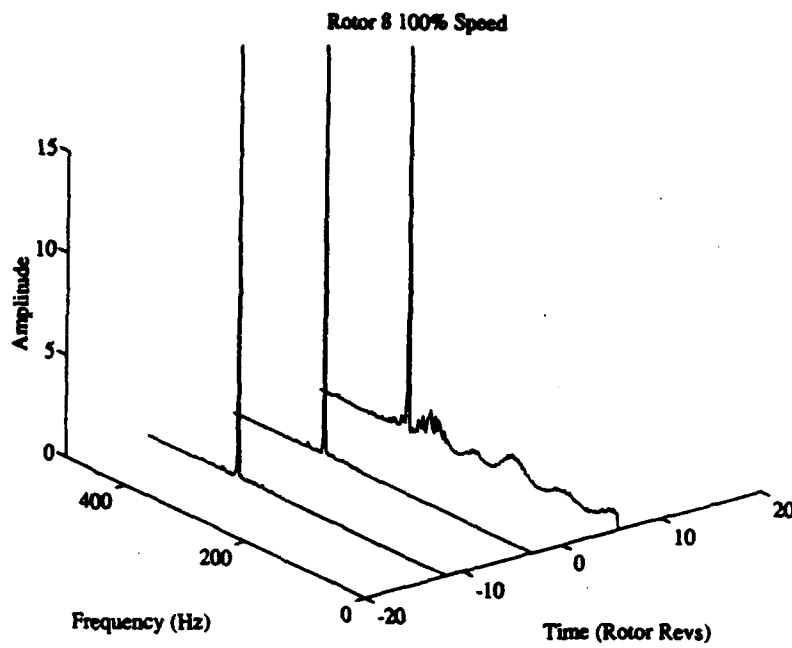


**Figure 4.60 Windowed Frequency Pressure Signal Data
Rotor 8 100% Speed**

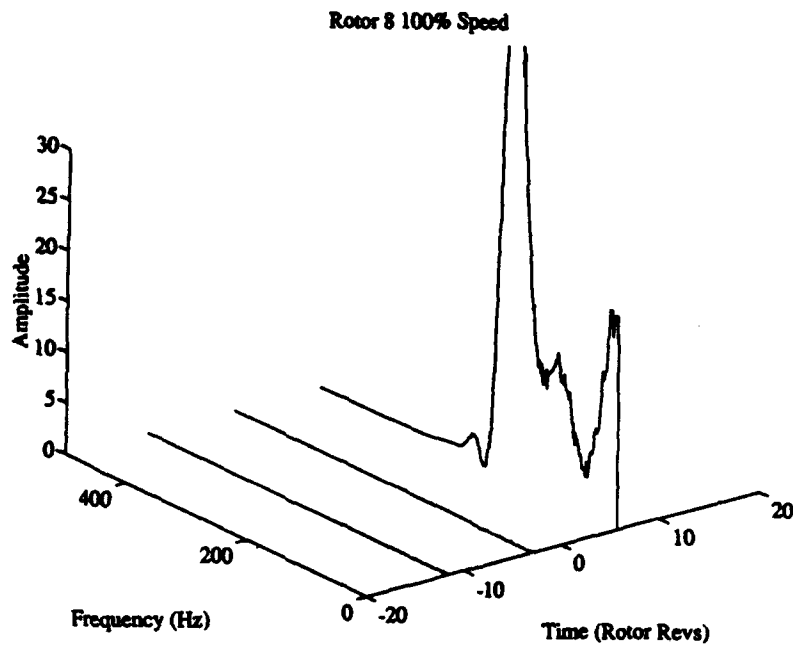


**Figure 4.61 Windowed Frequency Spectrum from SFCs
Rotor 8 100% Speed**

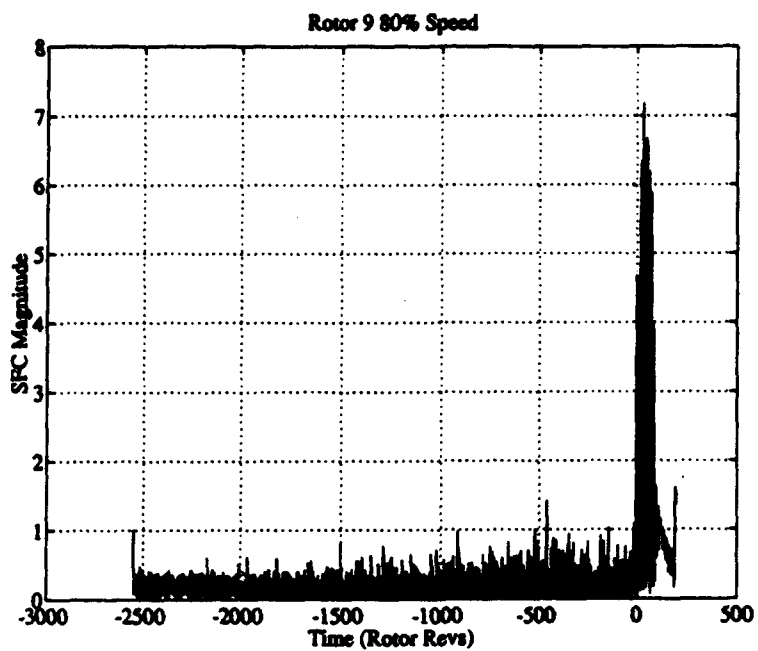


**Figure 4.62 Spatial Fourier Magnitude versus Time plot
Rotor 9 80% Speed**

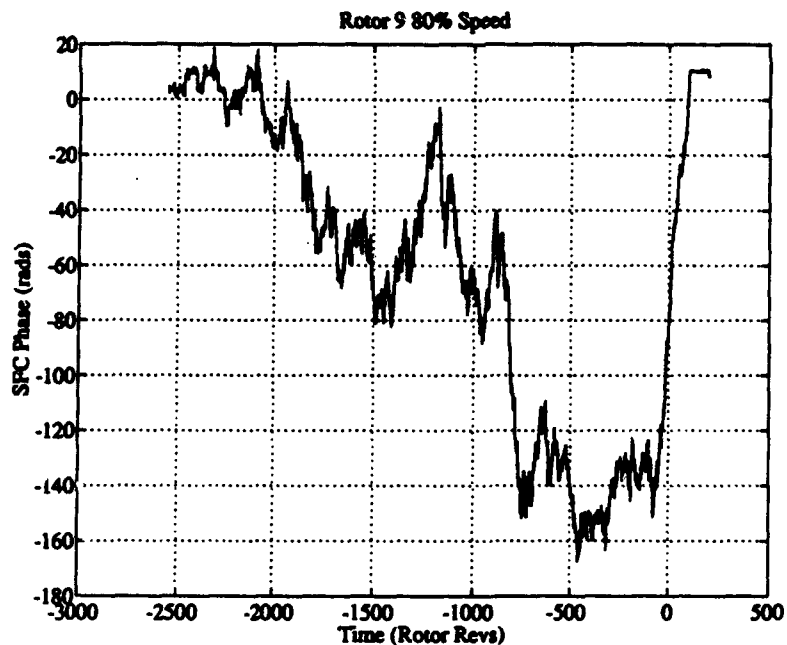


**Figure 4.63 Spatial Fourier Phase versus Time plot
Rotor 9 80% Speed**

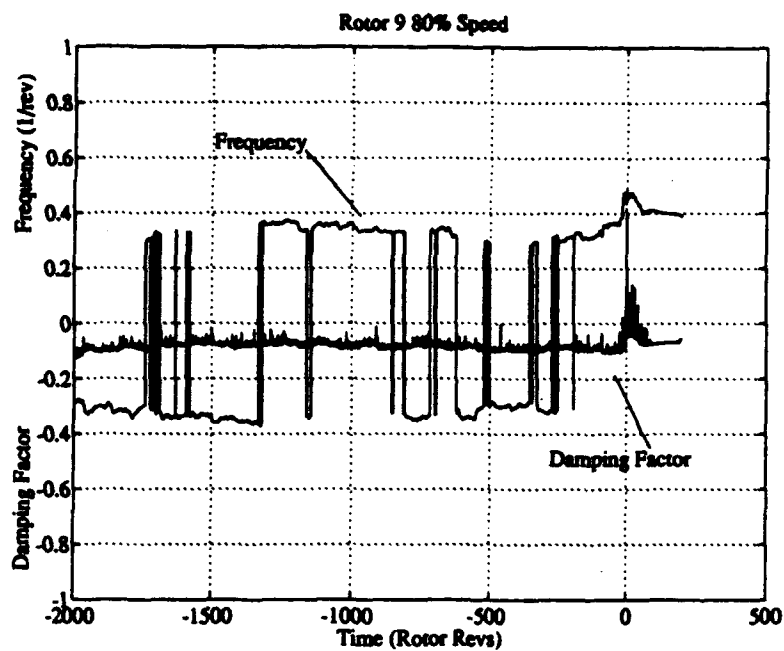


**Figure 4.64 Frequency and Damping Factor
Rotor 9 80% Speed**

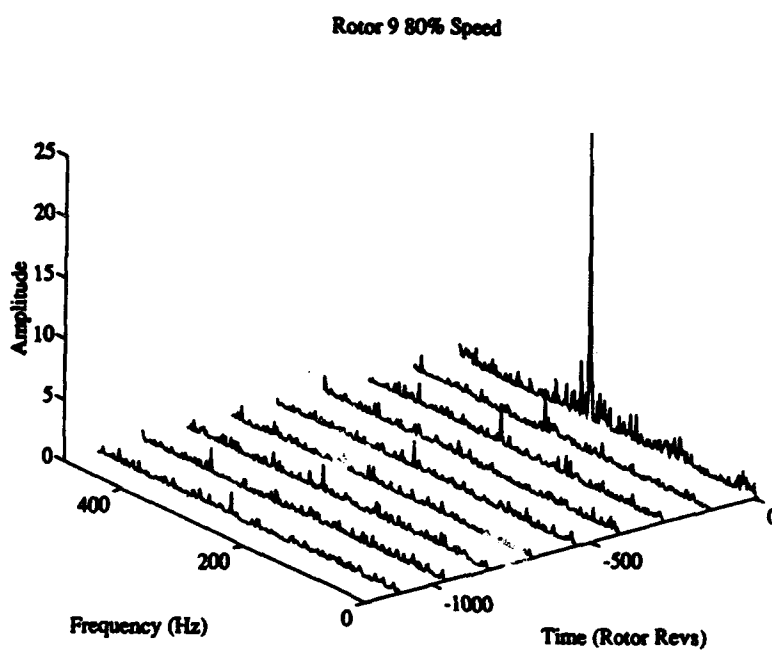


**Figure 4.65 Windowed Frequency Pressure Signal Data
Rotor 9 80% Speed**

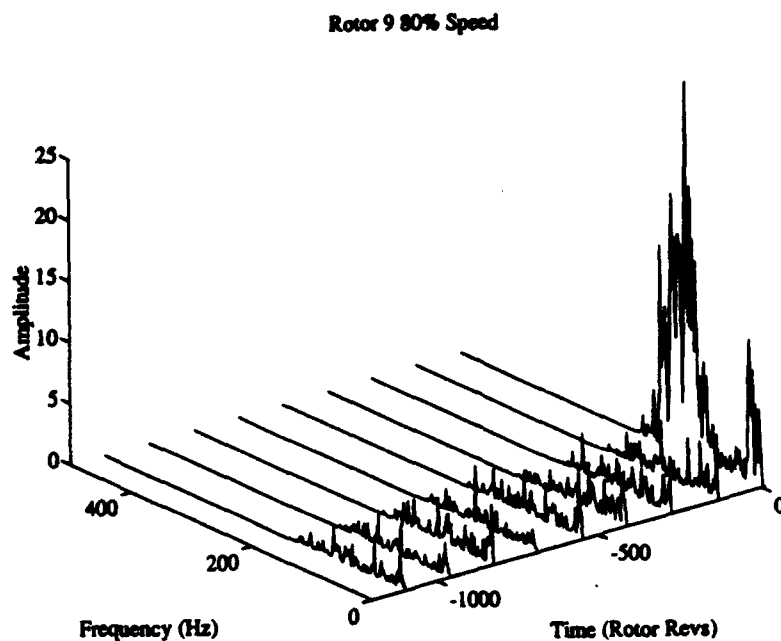


**Figure 4.64 Windowed Frequency Spectrum from SFCs
Rotor 9 80% Speed**

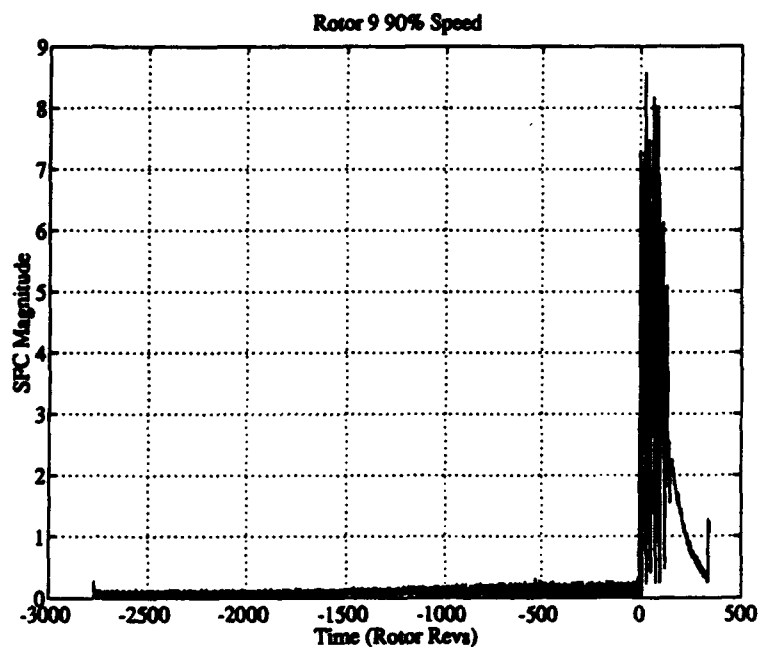


**Figure 4.65 Spatial Fourier Magnitude versus Time plot
Rotor 9 90% Speed**

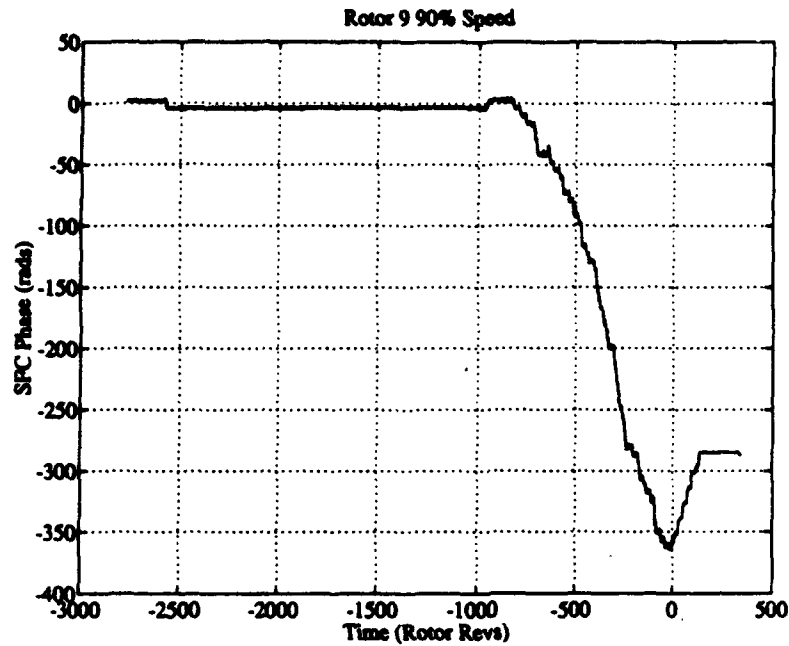


**Figure 4.66 Spatial Fourier Phase versus Time plot
Rotor 9 90% Speed**

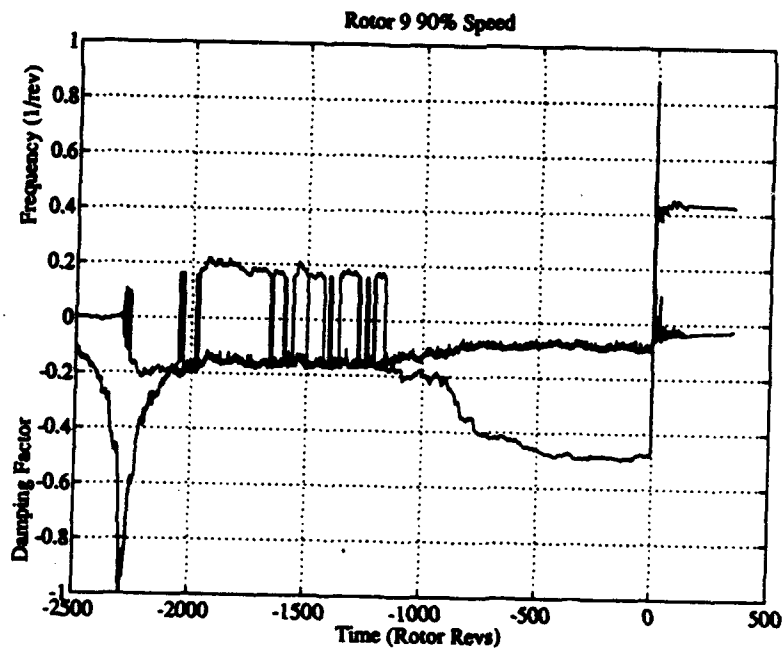


**Figure 4.67 Frequency and Damping Factor
Rotor 9 90% Speed**

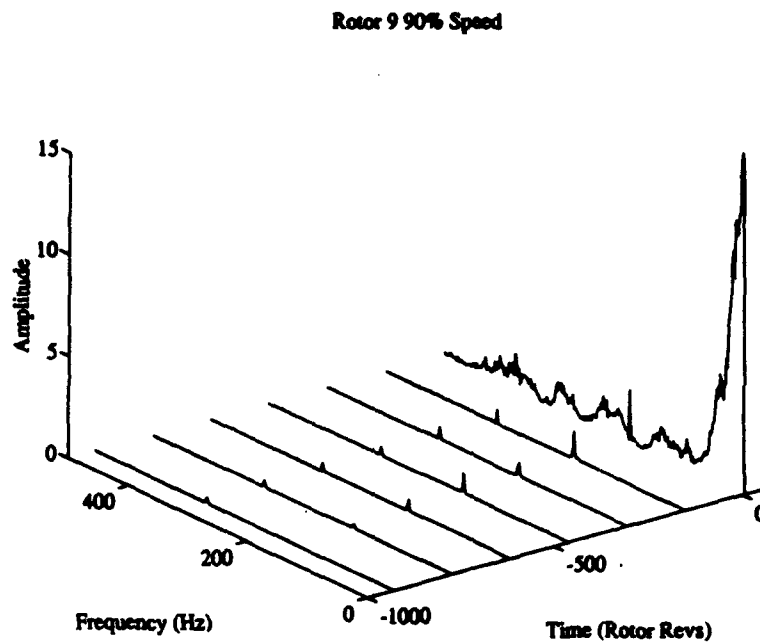


**Figure 4.68 Windowed Frequency Pressure Signal Data
Rotor 9 90% Speed**

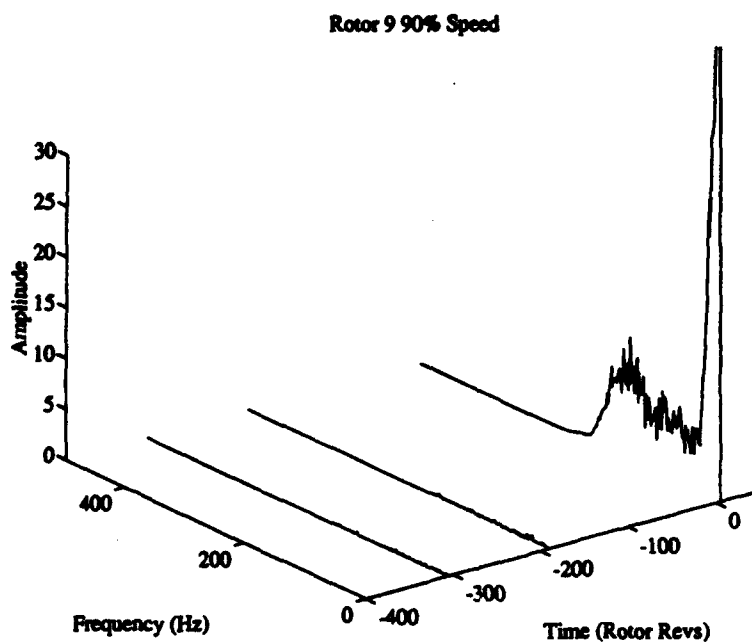


**Figure 4.69 Windowed Frequency Spectrum from SFCs
Rotor 9 90% Speed**

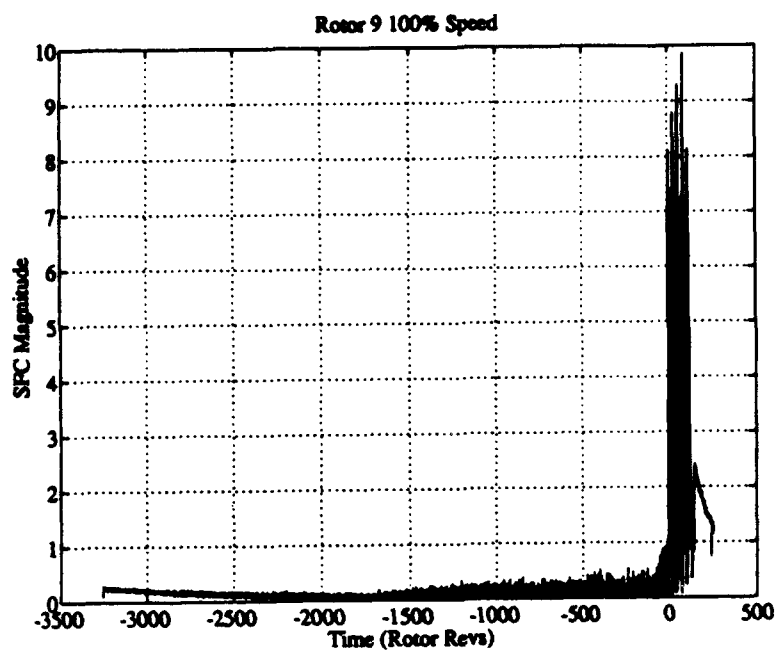


**Figure 4.70 Spatial Fourier Magnitude versus Time plot
Rotor 9 100% Speed**

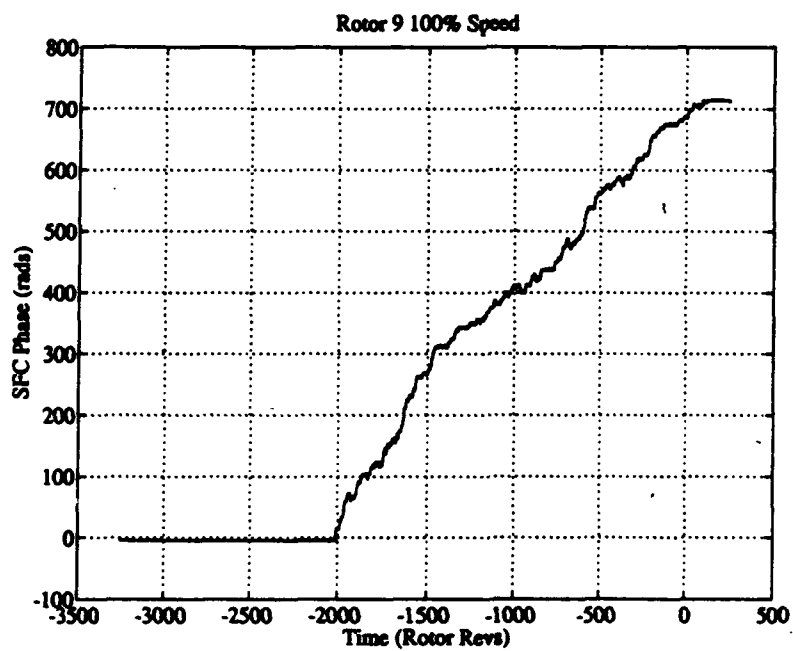


**Figure 4.71 Spatial Fourier Phase versus Time plot
Rotor 9 100% Speed**

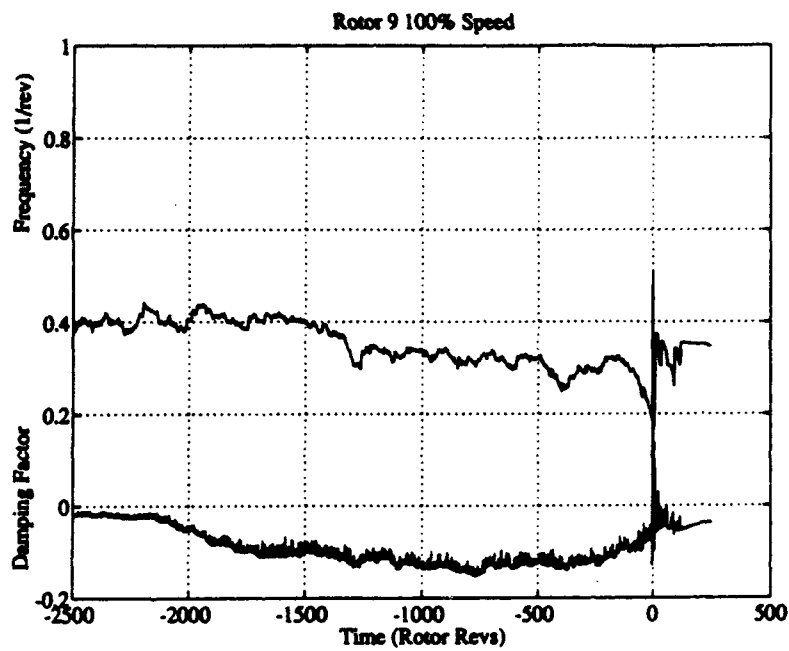


**Figure 4.72 Frequency and Damping Factor
Rotor 9 100% Speed**

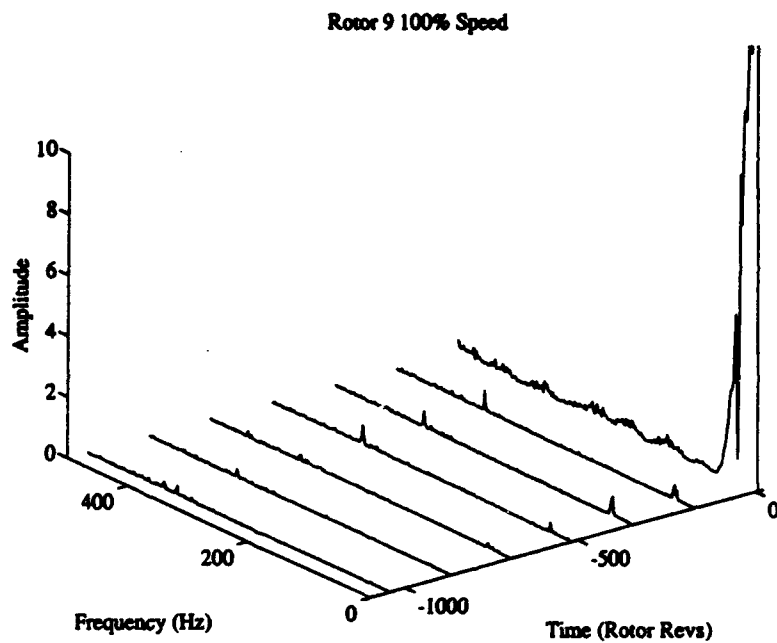


**Figure 4.73 Windowed Frequency Pressure Signal Data
Rotor 9 100% Speed**

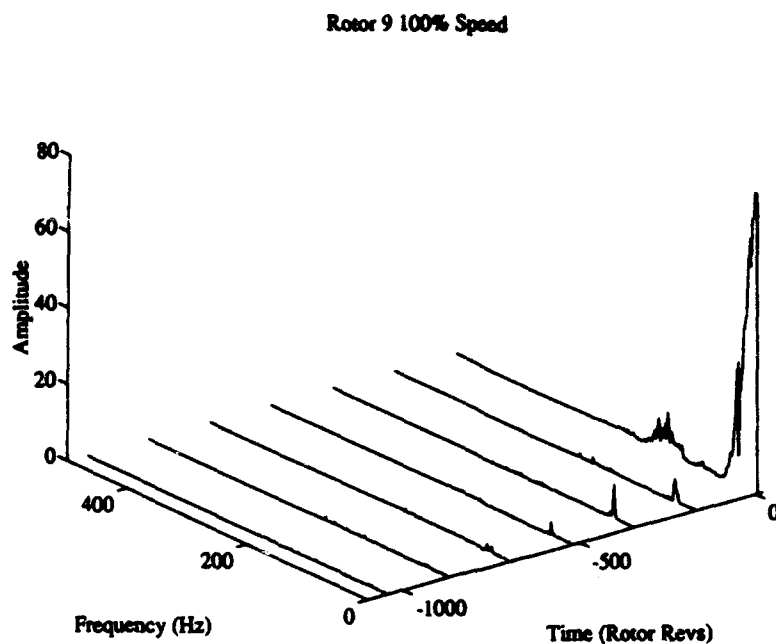


**Figure 4.74 Windowed Frequency Spectrum from SFCs
Rotor 9 100% Speed**

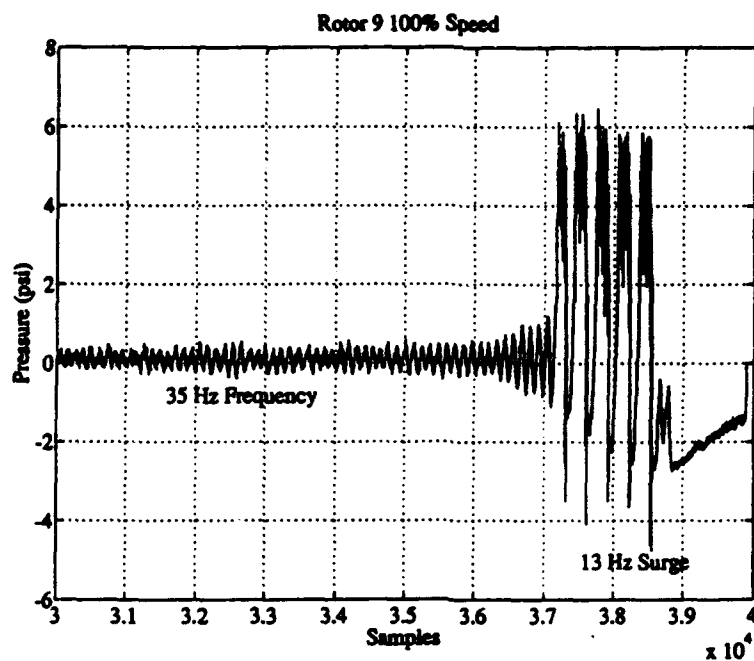


**Figure 4.76 Pressure versus Samples for one Kulite Trace
Rotor 9 100% Speed (Sample rate = 4000 samples/sec)**

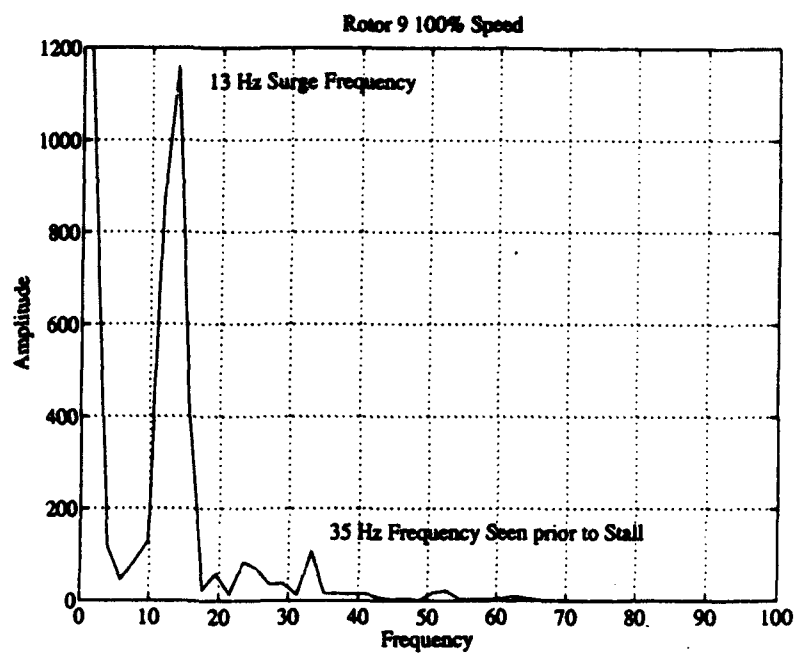


Figure 4.77 FFT of Rotor 9 100% After Stall

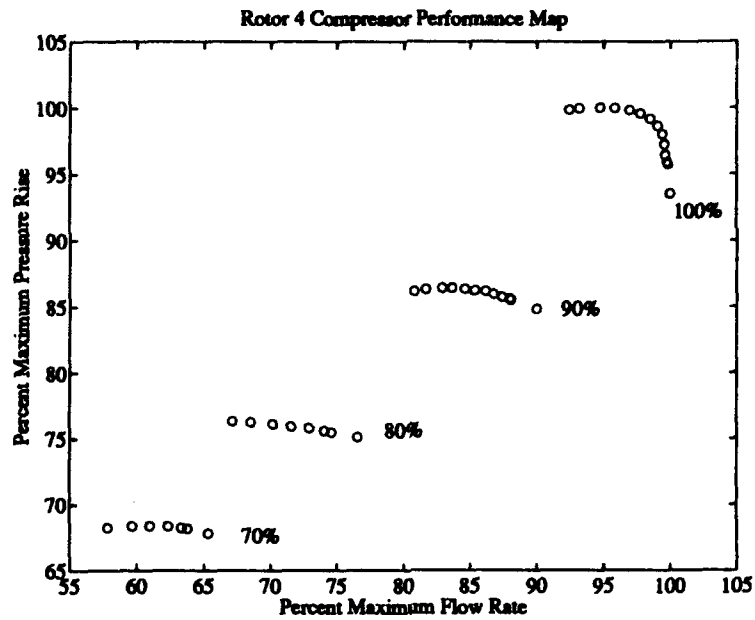


Figure 5.1 Compressor Map for Rotor 4

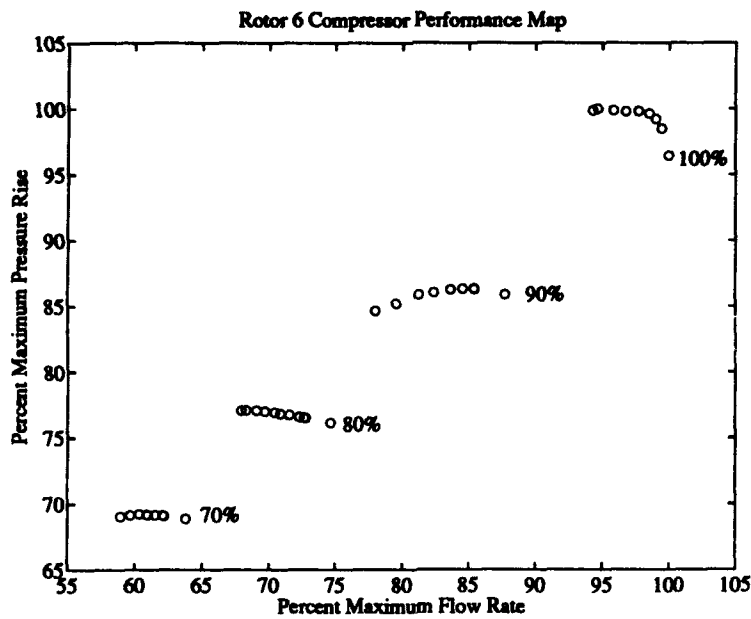


Figure 5.2 Compressor Map for Rotor 6

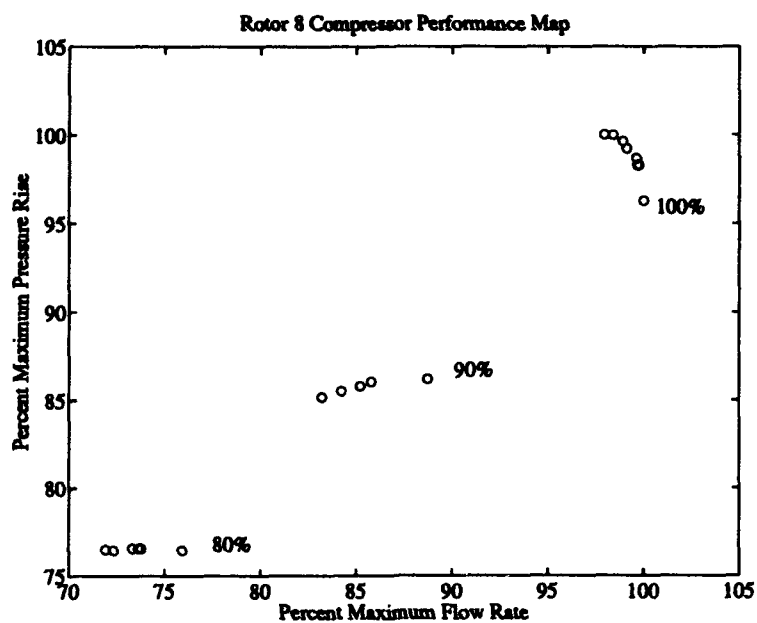


Figure 5.3 Compressor Map for Rotor 8

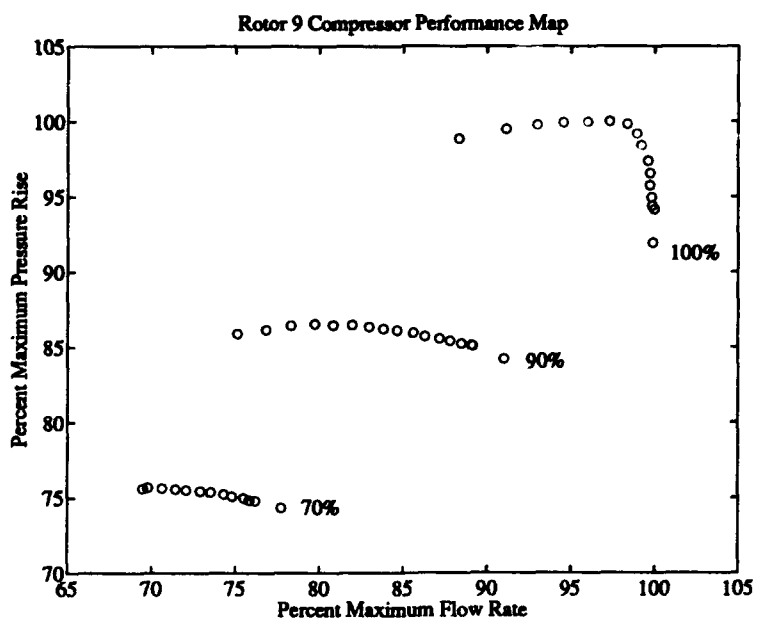


Figure 5.4 Compressor Map for Rotor 9

VITA

Capt. Bernard J. Frank was born in Beaver Falls, PA. on the 26th day of July 1960. He graduated from Rochester Area High School as a member of the National Honor Society in 1978. After 3 years at Gannon University, He entered military service via Basic Military Training in 1981.

His enlisted career spanned 8 years, the first 5 of which were spent in the Electronic Security Command. During this time frame, he received numerous awards including being chosen as one of the 12 Outstanding Airman of the Air Force in 1984. The last 3 years of his enlisted service were spent as a selectee of the Airman Education and Commissioning Program. He attended the University of Missouri-Rolla, where he graduated Cum Laude with a Bachelors Degree in Aerospace Engineering in 1989.

Capt. Frank attended the Air Force Officer Training School in the summer of 1989. He received his commission on September 28, 1989. His first assignment was to the Oklahoma City Air Logistic Center, Tinker AFB. His assignment to the Propulsion Directorate involved varied aspects of engine management and maintenance. Capt. Frank was the lead engineer for the prototype maintenance verification team for the F118-GE-100, B-2 bomber engine. He was also involved in the acquisition of a heat treating facility upgrade for the OKC-ALC.

In May of 1992, Capt Frank began his graduate studies at the Air Force Institute of Technology. His field of study was Aeronautical Engineering. Upon completion of his Masters Degree, he will be assigned to the Compressor Research Facility at Wright-Patterson AFB, where he will continue his research and study of compressor surge and stall.

**Permanent Address: 845 Deer Lane
Rochester, PA
15074**

REPORT DOCUMENTATION PAGEForm Approved
OMB No. 0704-0188

Public reporting burden for this collection of information is estimated to average 1 hour per response, including the time for reviewing instructions, searching existing data sources, gathering and maintaining the data needed, and completing and reviewing the collection of information. Send comments regarding this burden estimate or any other aspect of this collection of information, including suggestions for reducing this burden, to Washington Headquarters Services, Directorate for Information Operations and Reports, 1215 Jefferson Davis Highway, Suite 1204, Arlington, VA 22202-4302, and to the Office of Management and Budget, Paperwork Reduction Project (0704-0188), Washington, DC 20503

1. AGENCY USE ONLY (Leave blank)		2. REPORT DATE December 1993	3. REPORT TYPE AND DATES COVERED Master's Thesis
4. TITLE AND SUBTITLE ANALYSIS AND CHARACTERIZATION OF COMPRESSOR STALL PRECURSOR SIGNALS IN FORWARD AND AFT SWEEP HIGH SPEED COMPRESSORS			5. FUNDING NUMBERS
6. AUTHOR(S) Bernard J. Frank, Captain, USAF			
7. PERFORMING ORGANIZATION NAME(S) AND ADDRESS(ES) Air Force Institute of Technology WPAFB, OH 45433-7765			8. PERFORMING ORGANIZATION REPORT NUMBER AFIT/GAE/ENY/93D-14
9. SPONSORING/MONITORING AGENCY NAME(S) AND ADDRESS(ES) William W. Copenhaver WL/POTX WPAFB, OH 45433-6523			10. SPONSORING/MONITORING AGENCY REPORT NUMBER
11. SUPPLEMENTARY NOTES			
12a. DISTRIBUTION/AVAILABILITY STATEMENT Approved for public release, Distribution Unlimited			12b. DISTRIBUTION CODE
13. ABSTRACT (Maximum 200 words) The stall characteristic of four single-stage transonic compressor rotors were investigated as they were throttled to stall. Forward-swept, backward-swept, and straight leading edge rotors were examined. Three methods of analysis (1) windowed power spectrum densities of pressure and spatial Fourier coefficients, (2) phase tracking analysis, and (3) system identification were used to identify the first appearance of modal waves and their accompanying frequencies in order to identify a stall warning time. A direct correlation between the amount of stall warning time and the shape of the compressor characteristic was found. Specifically, if the compressor characteristic had a significant period of flat or positive slope, more stall warning was noted. It was also found that the forward-swept rotor consistently provided more stall warning time than the backward-swept and straight leading edge rotors.			
14. SUBJECT TERMS Compressors, axial compressor, compressor stall, stall inception, compressor stability, stall warning, transonic compressor, forward-swept compressor, aft-swept compressor			15. NUMBER OF PAGES 123
			16. PRICE CODE
17. SECURITY CLASSIFICATION OF REPORT Unclassified	18. SECURITY CLASSIFICATION OF THIS PAGE Unclassified	19. SECURITY CLASSIFICATION OF ABSTRACT Unclassified	20. LIMITATION OF ABSTRACT UL